Processing of $Pb(Mg_{1/3}Nb_{2/3})O_3$-$PbTiO_3$ by a Novel Coating Approach

A Thesis

Submitted to the Faculty

of

Drexel University

by

Huiming Gu

in partial fulfillment of the

requirements for the degree

of

Doctor of Philosophy

November 2003

DEDICATIONS

To family with love.

ACKNOWLEDGEMENTS

First of all, I would like to thank my advisors Dr. Wei-Heng Shih and Dr. Wan Y. Shih for their supports, guidance, and encouragements. Their creative ideas and encouragement for independent thinking were invaluable not only to the accomplishment of this work but also to the rest of my life. Also, I wish to extend my deep gratitude to my doctoral thesis committee members, Dr. Michel Barsoum, Dr. Raj Mutharasan, and Dr. Antonios Zavaliangos for their advices on my research.

I would also like to express my sincere thanks to my colleagues, Dr. Xiaoping Li, Mr. Qiang Zhao, Mr. Hongyu Luo, and Dr. Chia-Yi Yang for their tremendous help in my experiments and for the good discussions between us.

Also, I sincerely thank all other faculty members, staffs, and fellow graduate students in the Department of Materials Science and Engineering for the help, discussion and friendship. In particular, thanks to Mrs. Judith Trachtman for her kindly help and to Mr. David von Rohr for the technical supports through all my graduate study.

TABLE OF CONTENTS

LIST OF TABLES

LIST OF FIGURES

ABSTRACT

Processing of $Pb(Mg_{1/3}Nb_{2/3})O_3$-$PbTiO_3$ by a Novel Coating Approach

Huiming Gu

Wei-Heng Shih, Ph.D. and Wan Y. Shih, Ph.D.

$Pb(Mg_{1/3}Nb_{2/3})O_3$-$PbTiO_3$ (PMN-PT) is an important ferroelectric material that has outstanding room temperature dielectric constant and electro-mechanical coefficient. Unlike most other ferroelectric materials, PMN-PT is difficult to prepare because of the formation of unwanted pyrochlore phase. Many methods of PMN-PT preparation have been developed to overcome this problem over the past decades. The remaining major problems for these methods are the high sintering temperature of 1200°C and the complex processing steps. In this thesis, a new coating method is introduced for PMN-PT processing. This method involves coating $Mg(OH)_2$ on the surface of Nb_2O_5 particles to increase the mixing of chemical components and enhance the complete transformation from pyrochlore phase to perovskite phase. With this method, the processing is simplified to only one-step calcination for PMN-PT powder preparation and one-step sintering for PMN-PT dense part preparation. At the same time, the sintering temperature is decreased to 1000°C. To gain fundamental understanding on the colloidal coating process, a modified SAK simulation model was developed. In powder processing, it was shown that smaller particle size and better powder configurations were the reasons for eliminating pyrochlore phase. On the other hand, smaller particle size and reactive sintering are responsible for the lower temperature sintering. Finally, processing optimization study showed that 0-2 at.% PbO excess is the ideal composition for high quality PMN-PT preparation.

CHAPTER 1: INTRODUCTION

1.1 Background and Motivations

Ferroelectric ceramics are used in a broad range of electronic applications. These electronic applications account for more than 50% of the total high technology ceramics market.[1] Major applications of ferroelectric ceramics can be divided into five distinct areas:

1. Dielectric applications make use of the high dielectric permittivity, low dispersion, and wide frequency range of response for capacitors in multi-layer, thick and thin film form.[2, 3] Nonlinear hysteretic response is of interest for thin film non-volatile memory.[4]

2. Piezoelectric and electrostrictive responses in poled and un-poled ferroelectric and anti-ferroelectric compositions are of importance in transducers[5] for converting electrical to mechanical response and vice versa. Application makes use of the high piezoelectric constant d_{ijk} of the converse effect also permits efficient conversion of mechanical to electrical response. For actuation the strong electrostrictive coupling can be exploited for high precision position control.[6]

3. Pyroelectric systems rely upon the strong temperature sensitivity of electric polarization (dP_s/dT),[7] the pyroelectric effect in ferroelectrics, for the bolometric detection of long wavelength infrared (IR) radiation.[8] Simple point detectors are widely used in domestic and industrial application and there is now a strong focus upon imaging systems that may be used for night vision and for thermal-medical diagnostics.

4. P.T.C semiconductors are a specialized area of application in which the barrier to charge transport at the ceramic grain boundary in specially processed barium titanate based ceramics is controlled by the polarization state of the ferroelectrics, giving rise to an extremely strong positive temperature coefficient of resistivity (PTCR effect) controlled by the Curie point and the ferroelectric composition.[9]

5. In Electro-optic applications the properties of interest are the high quadratic and linear electro-optic coefficients which occur in ferroelectrics and the manner in which these can be controlled in modulators, switches,[10] guided structures and photo-refractive devices.

$Pb(Mg_{1/3}Nb_{2/3})O_3$ (PMN) or $Pb(Mg_{1/3}Nb_{2/3})O_3$-$PbTiO_3$ (PMN-PT) is one of the most widely studied ferroelectric ceramics because of its superior dielectric constant, electrostrictive, and piezoelectric coefficient.[11] For example, at the composition near 0.9PMN-0.1PT, its dielectric constant can be larger than 20,000, much higher than the commonly used capacitor materials $BaTiO_3$, which have a dielectric constant between 2,000 and 10,000. 0.9PMN-0.1PT also has a very high electrostrictive coefficient of 3.6×10^{-16} m^2/v^2. 0.65PMN-0.35PT, at the composition in the vicinity of the morphotropic phase boundary (MPB), could have very high piezoelectric coefficient of 560×10^{-12} C/N. This property is better than the commonly used PZT.[12, 13, 14, 15, 16, 17] Because of these superior properties, PMN or PMN-PT is very promising in the applications of transducer, electrostrictive device, and capacitor. But, compared with PZT and $BaTiO_3$, the synthesis of PMN or PMN-PT is not easy. This is one of the main reasons that PMN or PMN-PT was not widely utilized as PZT or $BaTiO_3$ in electronic ceramics industry.

Unlike most other ferroelectric ceramics, the desired perovskite phase of PMN or PMN-PT cannot be synthesized by simply calcining the component oxides mixture. It has been shown that the following equations are the reaction sequence during the calcination of the oxide mixture of PbO, MgO, and Nb_2O_5:[18, 19]

$$\mathrm{PbO} + \mathrm{Nb_2O_5} + \mathrm{MgO(Very\ small\ amount)} \xrightarrow{500-700°\mathrm{C}} \mathrm{Pyrochlore} \tag{1.1}$$

$$\mathrm{Pyrochlore} + \mathrm{MgO} + \mathrm{PbO} \xrightarrow{700-900°\mathrm{C}} \mathrm{Pb(Mg_{1/3}Nb_{2/3})O_3\,(Perovskite)} \tag{1.2}$$

In these two reactions, reaction (1.2) is not complete, indicating that the pyrochlore phase is not completely converted into perovskite phase. The final product is a mixture of both pyrochlore and perovskite phase. The presence of the pyrochlore phase degrades the dielectric and electromechanical property significantly.

Until now, the exact composition of the pyrochlore phase is still not clear. Many possible formulas have been proposed: $Pb_3Nb_4O_{13}$, $Pb_2Nb_2O_7$,[18] $Pb_5Nb_4O_5$, $Pb_3Nb_2O_8$,[19] $Pb_{1.83}Nb_{1.71}Mg_{0.29}O_{6.39}$,[20] $Pb_2Mg_{0.32}Nb_{1.87}O_7$,[21] $Pb_{1.86}Nb_{1.76}Mg_{0.24}O_6$,[22] $Pb_{2.25}Nb_{1.79}Mg_{0.27}O_7$,[23] $Pb_2Nb_{1.75}Mg_{0.25}O_{6.62}$,[24] $Pb_2Nb_{1.33}Mg_xO_{5.33+x}(0<x<0.66)$,[25] $Pb_3(Mg_{1-x}Nb_{2+x})O_{9+3x/2}(0<x<0.625)$,[26] $Pb_{(3+3x/2)/2}(Mg_xNb_{2-x})O_{0.65}(0<x<0.5)$,[27] $Pb_{1.83}Mg_{0.29+x}Nb_{1.71-x}O_{6.39-1.5x}(0.1<x<0.522)$,[28] and $Pb_{2-x}(Mg_{0.286}Nb_{1.714})O_{6.571-x}(0<x<0.286)$.[29] The common features of these formulas are that the pyrochlore phase is composed mainly of PbO and Nb_2O_5. It may contain a small amount of MgO in the lattice. The ratio of Pb:Nb in the pyrochlore phase is less than or equal to the ratio of Pb:Nb=1.5 in the perovskite phase. So, in essence, the transformation reaction from the pyrochlore to perovskite phase (equation 1.2) is a process of MgO and maybe some PbO diffusing into the lattice of the pyrochlore phase. Since the PbO melting temperature is low at 888°C,[30] the diffusion rate of PbO in the pyrochlore phase is quite high. Therefore, the critical factor in this reaction is controlled by the slower diffusion of MgO. For a multi-component system like PMN-PT, improving reactant homogeneity could significantly enhance the inter-diffusion and reaction between them. Based on this reasoning, it was found that improving the distribution and decreasing the particle size of MgO could significantly increase the percentage of perovskite phase formed in the final product.[31]

From the discussion above, the major challenge for pyrochlore-free PMN-PT powder processing is to improve the homogeneity of reactant components, especially MgO. So far, many methods have been found to be able to eliminate the formation of the pyrochlore phase under this principle. These methods can be divided into the following two categories:

1. Two-step calcination processing method

Swartz and Shrout[32] first succeeded in eliminating the pyrochlore phase by developing the columbite method that involved two calcination steps:

$$\mathrm{MgO} + \mathrm{Nb_2O_5} \xrightarrow{1000°\mathrm{C}} \mathrm{MgNb_2O_6}\ \text{(Columbite)} \tag{1.3}$$

$$\mathrm{MgNb_2O_6} + 3\mathrm{PbO} \xrightarrow{700\text{–}900°\mathrm{C}} 3\mathrm{Pb(Mg_{1/3}Nb_{2/3})O_3}\ \text{(Perovskite)} \tag{1.4}$$

In the first calcination step (equation 1.3), mixtures of Nb_2O_5 and MgO were heat-treated at around 1000°C to form the columbite phase, $MgNb_2O_6$. In the second calcination step (equation 1.4), $MgNb_2O_6$ was mixed and heat-treated with PbO. In this way, Nb_2O_5 and MgO are pre-reacted and mixed uniformly at atomic level. Since PbO are relative easy to diffuse, reaction (1.4) can be completed at a relative low temperature. Also the direct contact and reaction of Nb_2O_5 and PbO are eliminated, thus the formation of pyrochlore phase are prevented. This columbite method was adopted widely and is called the traditional method in the rest of this thesis.

2. One-step calcination processing method

Most methods found so far belong to this category. They include sol-gel methods,[33, 34, 35, 25] solution processes,[36, 37, 38] co-precipitation methods,[39] soft mechanochemical pulverization,[40] $Mg(NO_3)_2$ mixing,[41] and thermal spray.[42] These methods were based on the principle of improving the uniformity/reactivity of component reactants either by optimizing the powder characteristics including particle size, specific surface area, reactivity of raw materials such as $Mg(OH)_2$ or $Mg(NO_3)_2$, or by using a high-energy milling method. In this way, the reaction (1.2) can be more complete. Therefore, the pyrochlore phase is eliminated.

Using the two approaches mentioned above, the pyrochlore phase has been eliminated successfully in PMN or PMN-PT powder processing. But there are many steps involved in these processing methods. For example, for the traditional two-step calcination columbite method, two ball-milling and two calcination steps are required to obtain the perovskite phase PMN powder. For the one-step calcination processing methods, either special raw materials or special equipment were used. Some methods such as sol-gel methods, solution processes, co-precipitation methods, and thermal spray need even more processing steps than the traditional columbite method. Once the perovskite phase PMN powder was prepared, additional steps of ball-milling, pressing, and sintering are needed to obtain PMN dense part. For the mass production of PMN, a simplified production method using regular equipment and raw materials is needed.

Besides the pyrochlore phase and the multiple processing steps, another problem related to PMN or PMN-PT processing is its high sintering temperature. From regular perovskite PMN powder, a sintering temperature of 1200°C is needed to produce PMN dense part.[43] At this sintering temperature, PbO is very volatile.[44] The volatile nature of PbO could cause imprecise composition and deteriorates the properties of final product. Also, too much PbO evaporation is very harmful to the environments. Further more, at such a high sintering temperature, expensive electrode materials such as Pt or Pd have to be used in Multi-Layer-Capacitor (MLC) industry instead of the cheaper Ag and Cu electrode. In order to use Ag and Cu as electrodes, the sintering temperature cannot be higher than 1000°C.[43]

Targeting to decrease the sintering temperature and reduce the processing steps, several processing methods have been investigated. For example, it was found that an excess of 5-21 wt% of PbO could decrease the sintering temperature to 950°C.[45] 1-4 at% of SrO doping would result in the sintering temperature to be as low as 800-900°C.[46] Using the PMN powder made from $Mg(NO_3)_2$ mixing method, the sintering temperature could be decreased to 900°C.[41] By using thermal spray, pre heat-treatment, and reactive sintering, the sintering temperature could be decreased to 1050°C.[42] Liou et al[47] found that that directly pressing the columbite phase and PbO into green bodies and reactively sintering it could reduce the total processing steps of PMN dense part to 2 steps of ball-millings, 1 step of calcination, and 1 step of sintering. But the sintering temperature of this method was 1250°C. Later, with the same method, Kwon et al[48] succeeded in reducing the sintering temperature to 1000°C by using nanosize TiO_2, more reactive $(PbCO_3)_2Pb(OH)_2$ instead of PbO, and O_2 sintering atmosphere.

The methods mentioned above solved some of problems involved in PMN ceramic processing. But none of them can solve all these problems simultaneously. The method of S. Kwon et al is one of the best efforts that have been published so far. It prevented the pyrochlore phase from formation, decreased the sintering temperature, and reduced one ball-milling and one calcination step from the processing. But it uses nanosize reactant and needs O_2 sintering atmosphere. Also it still needs 2 steps of ball-milling, 1 step of calcination, and 1 step of sintering.

1.2 Objectives and Approaches

The major challenges for PMN-PT processing are: (1) the formation of pyrochlore phase needs to be eliminated; (2) the sintering temperature needs to be lowered; (3) the processing needs to be simplified. The major objective of this thesis is to find a method that can address these challenges simultaneously. Based on the publication results introduced in the previous section, it is clear that increasing the uniformity/reactivity and decreasing particle size could eliminate the formation of pyrochlore phase. Reactive sintering or one-step calcination powder processing could simplify the processing. Doping, nanosize raw material, and O_2 sintering atmosphere could decrease the sintering temperature. If we can find a method that takes advantage of these factors simultaneously, our objective can be achieved. Some of the factors like doping, O_2 sintering atmosphere, nanosize raw materials are what we try to avoid since they would lessen the properties or increase production cost. Therefore the major challenges are how to simultaneously take advantage of other factors, such as improving particle uniformity/reactivity, decreasing particle size, reactive sintering or one-step calcination.

These factors are not in conflict with each other. For example, improving component homogeneity/reactivity and decreasing particle size could prevent the pyrochlore phase. Therefore, one-step calcination or reactive sintering could be used to simplify processing. At the same time, improving components homogeneity and decreasing particle size could improve both the driving force and kinetics for the sintering, thus decrease the sintering temperature.

Based on the analysis above, the first step to achieve our objective is to find an effective method to improve the component distribution and decrease the component particle size.

Colloidal coating has been proven to be an effective method in improving component homogeneity. For example, it had been demonstrated that nearly fully dense ZnO and ZrO_2 composite ceramic could be obtained by coating ZnO on the surface of ZrO_2.[49] Specific to the system of PMN-PT, colloidal coating of $Mg(OH)_2$ on Nb_2O_5 may fulfill our requirements of improving component homogeneity and decreasing particle size due to the following reasons:

1. Wet-chemical processing could decrease the particle size. The $Mg(OH)_2$ coating could be realized by colloidally precipitating $Mg(OH)_2$ in Nb_2O_5 suspension. The $Mg(OH)_2$ precipitation obtained in this way is usually in amorphous state, which is very easy to decompose upon heat-treatment. During the decomposition, the amorphous $Mg(OH)_2$ coating could break down into nanosize MgO particle.

2. Colloidal coating of $Mg(OH)_2$ on Nb_2O_5 could improve the homogeneity of these two components. Comparatively, the diffusion rate of Mg^{2+} and Nb^{5+} are much lower than that of Pb^{2+} in both sintering and reaction. So their inter-diffusion is the bottleneck for both the reaction and sintering for PMN-PT processing. Colloidal coating of $Mg(OH)_2$ on Nb_2O_5 could bring them close together and make them more uniformly distributed with each other. Thus it could significantly improve their inter-diffusion.

As a result, our first step is to colloidally coat $Mg(OH)_2$ on the surface of Nb_2O_5 particle then mix with PbO powder.

Upon the realization of our first step, the second step is to find a simplified low temperature processing method for PMN-PT sintering.

The coating method has the potential of improving homogeneity and decreasing particle size. Therefore, it is a very promising method in eliminating the pyrochlore phase and decreasing the sintering temperature. As demonstrated by Liou et al[47] and Kwon et al,[48] reactive sintering $MgNb_2O_6$ and PbO could decrease the processing steps. Based on these facts, we plan to accomplish our second step by reactive sintering the colloidally coated powder. Since the coating method have the potential of eliminating pyrochlore phase, we plan to reactively sinter the coated powder from the very beginning instead of from the mid product of $MgNb_2O_6$ like in Liou and Kwon's methods. In this way the processing could be simplified further.

Once the objective of the low temperature reactive sintering of PMN-PT is realized, the second objective is to understand the mechanism and new phenomena involved in this method. The knowledge gained could be used to optimize the processing and the method could be expanded to other systems in the future. To accomplish this objective, materials analysis method such as DTA, X-ray diffraction, particle size analyzer, SEM, etc., will be used to analyze the phase, particle, structural evolution during reactive sintering. Simple models will be proposed to understand the process.

1.3 Thesis Outline

This thesis will be organized into 9 chapters. The research background, objective, and the approach we use to realize our objective will be introduced in the first chapter. Chapter 2 will explain the fundamental concept of ferroelectricity, piezoelectricity, electrostriction, and colloidal interaction. Because our studies are based on colloidal coating, the fundamental of colloidal coating will be studied in Chapter 3 via numerical simulation. Chapter 4 will illustrate that the perovskite phase PMN or PMN-PT powder can be produced by the coating method with the one-step calcination process. The reasons why the coating method can prevent the formation of pyrochlore phase will be analyzed in Chapter 5. Chapter 6 will illustrate that reactive sintering and the coating method can decrease the sintering temperature and reduce PMN or PMN-PT dense part processing steps. The low temperature sintering mechanism will be illustrated in Chapter 7. Partial processing optimization will be discussed in Chapter 8 by finding an optimized PbO composition. Finally this thesis will be concluded with conclusions and future work in Chapter 9.

CHAPTER 2: THE FUNDAMENTALS

2.1 Concepts of Ferroelectricity

2.1.1 Piezoelectricity, Ferroelectricity, and Electrostriction

In the dielectric materials, the constituent atoms are considered to be ionized to a certain degree and are either positively or negatively charged. In such ionic crystals, when an electric field is applied cations are attracted to the cathode and anions to the anode due to electrostatic interaction. The electron clouds also deform, causing electric dipoles. This phenomenon is known as the electric polarization of the dielectrics, and the polarization is expressed quantitatively as the sum of the electric dipoles per unit volume [C/m^2]. Figure 2.1 shows schematically the origin of the electric polarization. There are three kinds: electronics, ionic and dipole reorientation-related polarizations.

Compared with vacuum capacitors, dielectric capacitors can store more electric charge due to the electric polarization P. The physical quantity corresponding to the stored electric charge per unit area is called the electric displacement D and is related to the electric field by the following expression:

$$D = \varepsilon_o E + P = \varepsilon\varepsilon_o E \tag{2.1}$$

Here, ε_o is the vacuum permittivity ($=8.854\times10^{-12}$ F/m), ε is the material's relative permittivity (also simply called permittivity or dielectric constant).

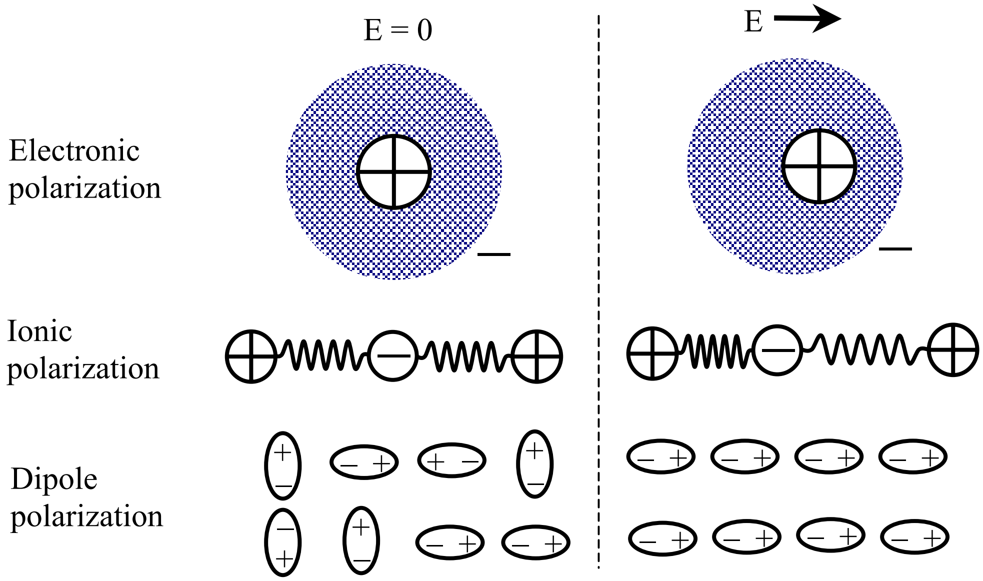

Figure 2.1: Microscopic origins of the electric polarization

Depending on the crystal structure, the centers of the positive and negative charges of some crystals do not coincide even without the application of external electric field. Such crystals are said to possess spontaneous polarization. When the spontaneous polarization of the dielectric can be altered by an electric field, it is called ferroelectric. Not every dielectric can be a ferroelectric. Crystals can be classified into 32 point groups according to their crystallographic symmetry, and these point groups can be divided largely into two classes, one with a center of symmetry and the other without. As showed in Figure 2.2, there are 21 point groups which do not have a center of symmetry. In crystals belonging to 20 of these point groups [except for the point group of cubic (432)], positive and negative charges appear on surfaces when stresses are applied. These surface charges are caused by stress induced polarization change. The materials are called as piezoelectrics. For piezoelectrics, the relationship between mechanical parameter and electrical parameter is usually expressed in the following equations:

$$D_i = \Sigma d_{ij} T_j \text{ (direct effect)} \qquad (2.2)$$

$$S_i = \Sigma d_{ij} E_j \text{ (converse effect)} \qquad (2.3)$$

Here, d is called piezoelectric coefficient. In addition to the d coefficients, open-circuit g coefficients are also used to evaluate piezoelectric ceramics for their ability to generate large amounts of voltage per unit of input stress. g have the following relationship with d:

$$g = d/\varepsilon\varepsilon_o \qquad (2.4)$$

Among the 20 piezoelectric point groups, 10 of them have temperature dependent spontaneous polarization, which means electric charges corresponding to temperature change appear on the surface of the crystal. This property is called pyroelectricity. Among the pyroelectric crystals, those whose spontaneous polarization can be reversed by an electric field are called ferroelectrics. There is some ambiguity in this definition. In order to establish ferroelectricity, it is necessary to apply an electric field on the pyrochlore material and experimentally ascertain the polarization reversal.

Electrostriction is electromechanical effect that unlike both in origin and behavior with piezoelectricity. In piezoelectricity, the deformation is linear with respect to the applied field and changes sign when the field is reversed. In electrostriction, the sign of the deformation that occurs with an electric field is independent of the polarity of the field and is proportional to even powders of the field. The corresponding equation is:

$$S = ME^2 \qquad (2.5)$$

Here M is the electrostrictive coefficients.

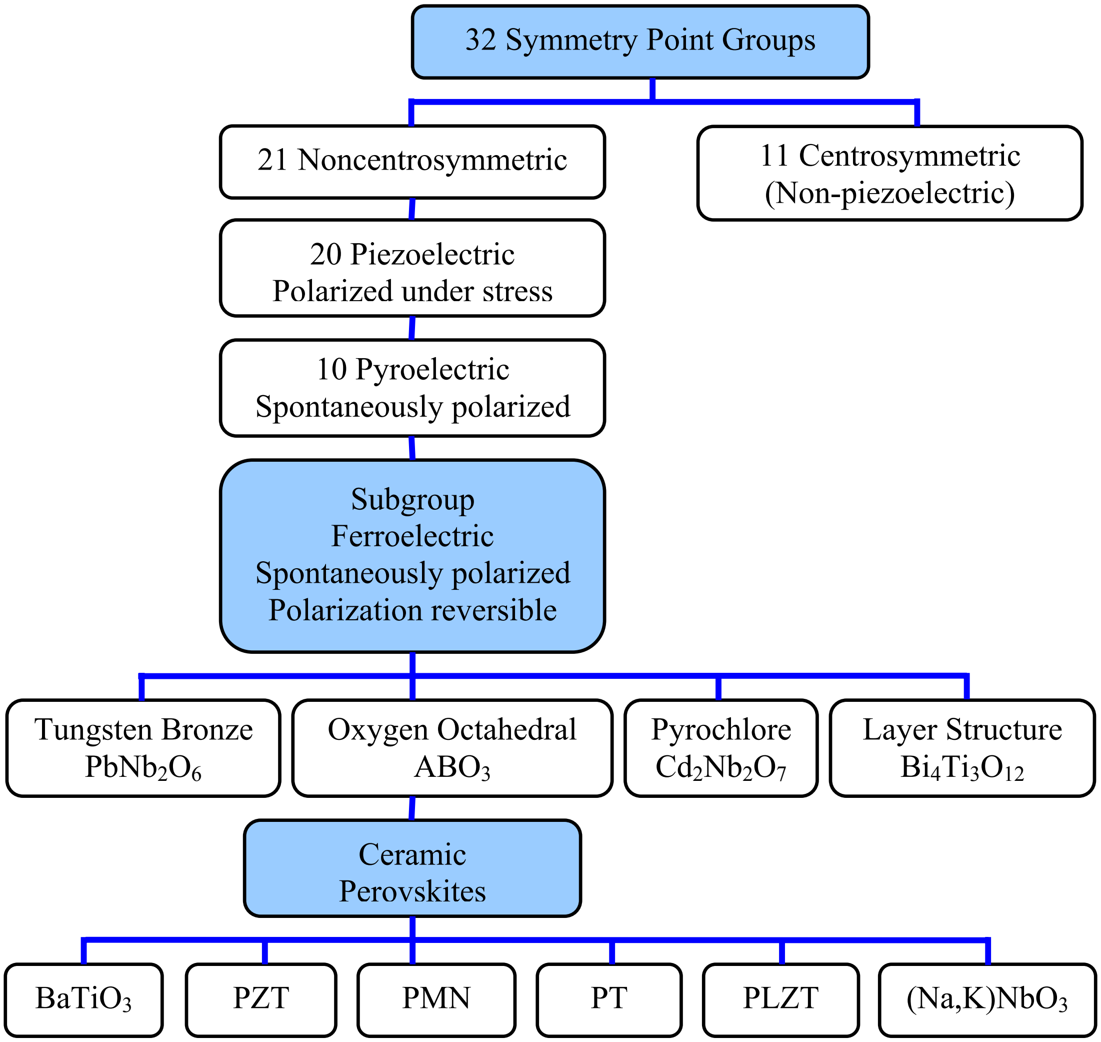

Figure 2.2: Interrelationship of piezoelectric and subgroups on the basis of symmetry

Figure 2.3 illustrated the difference between piezoelectric effect and electrostrictive effect in origination with a one-dimensional rigid-ion spring model. Under an applied electric field, the cations are drawn in the direction of the electric field and the anions in the opposite direction, leading to the relative change in the inter-ionic distance. For the case of piezostriction (Figure 2.3 (a)), the spring is un-symmetric, so strain (S) is in the relationship with first order of the electric field (E) applied. For the case of electrostriction (Figure 2.3 (b)), the spring is symmetric. In most cases, the springs posses anharmonicity, which means they are somewhat easy to extend but hard to contract. So, strain (S) is in an even order relationship with electric field (E) applied.

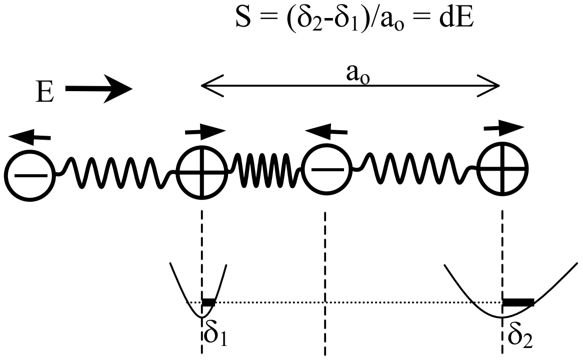

(a) Piezostriction

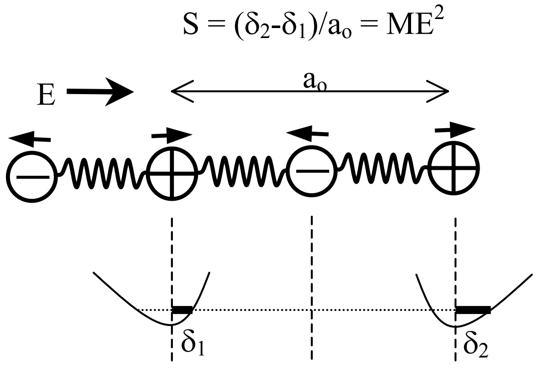

(b) Electrostriction

Figure 2.3: Microscopic explanations of the piezostriction and electrostriction

According the illustration in Figure 2.3, electrostriction is a general property of all dielectric materials, whether they are crystalline, amorphous, polar, or centrosymmetric. But the electrostriction can be particularly large in ferroelectric materials just above their curie temperature, where an electric field can enforce the energetically unstable ferroelectric phase. More commonly, this effect is utilized to good advantage in relaxor materials, such as PMN, PZN (lead zinc niobate), and PLZT, where the curie temperature is not sharp but rather is spread out over a moderate temperature range, thus allowing for a reasonable temperature range of operation for devices made from them. Some advantages for electrostrictors over conventional piezoelectrics are (1) hysteresis in the strain-field dependence is minimal or negligible in a selected temperature range, (2) realized deformation is more stable and comparable to the best piezoelectric ceramics, and (3) no poling is required.

2.1.2 Relaxor

Relaxor is a subgroup of ferroelectrics. It is unique in the onset of proper ferroelectric behavior. In Figure 2.4(a) is illustrated first the behavior in rather perfect single crystal which goes through an abrupt second order phase transition into the ferroelectric phase. Above T_c, the permittivity follows a Curie Weiss law $\varepsilon=C(T-T_c)^{-1}$, at T_c there is an abrupt but continuous onset of spontaneous polarization which evolves into the domain structure of the ferroelectric form. In some crystals the transition at T_c is first order, there is a finite maximum of ε at T_c and the Curie Weiss temperature θ in the relation $\varepsilon=C(T-\theta)^{-1}$ occurs some degrees below T_c e.g. 11ºC in $BaTiO_3$. Again there is an abrupt loss of polarization at T_c now in a discontinuous step but ε_{max} and $P_s \rightarrow 0$ occur at the same temperature T_c.

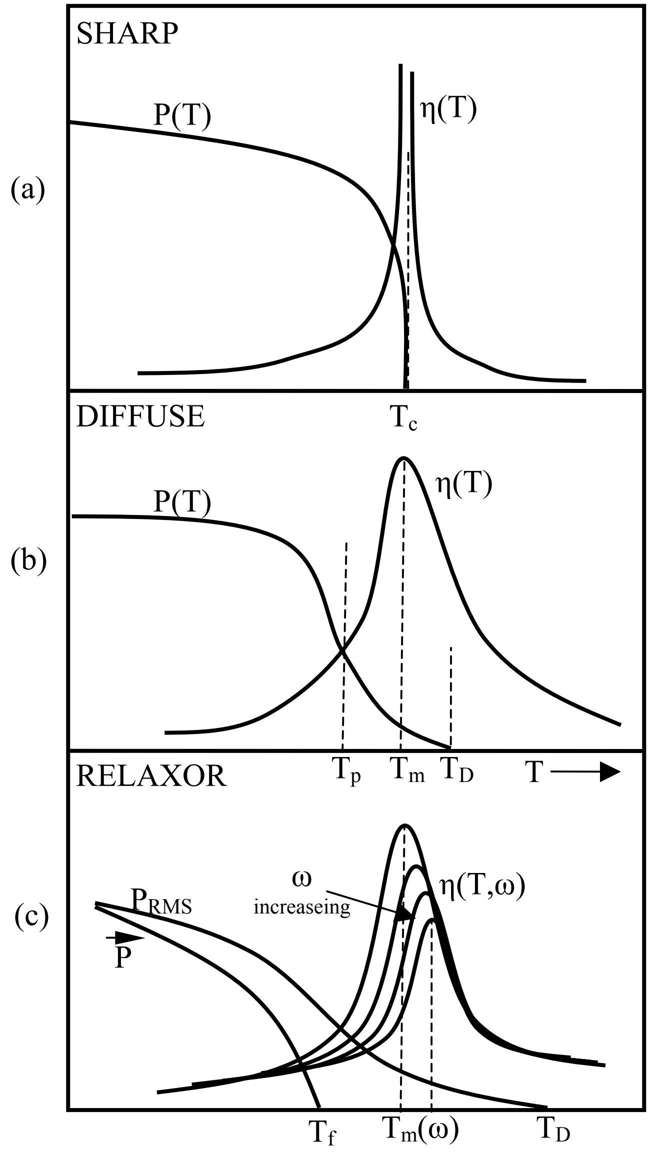

Figure 2.4: Types of ferroelectric phase transitions. (a) simple proper ferroelectric: sharp second order phase change in highly perfect single crystal. (b) diffuse phase transition associated with macroscopic heterogeneity as in practical capacitor dielectrics. (c) relaxor ferroelectric defining $T_m(\omega)$, T_D, T_F.

For many practical applications it is desired to use the very large property maxima in the vicinity of the ferroelectric phase transition, to move the transition into the temperature range of interest and to broaden and diffuse the very large sharp peak values.

In solid solution systems this is accomplished by trimming the mean composition to move the Curie point and at the same time making the sample (often a ceramic) deliberately inhomogeneous. In these diffuse transition systems the dielectric maximum is now much 'rounder' and polarization persists for a short range of temperature above T_m (Figure 2.4 (b)). Almost all practical Z5U and Y5V capacitor dielectrics use such diffuse transitions.

In the relaxor ferroelectrics, three features of the dielectric response are qualitatively different. The transition is clearly diffuse and rounded, but the response is now markedly dispersive below T_m and T_m is a function of frequency (Figure 2.4(c)). The response at weak fields above T_m is no longer Curie Weiss. In the polarization the RMS value persists to a temperature (T_D) 200°C to 300ºC above T_m but the mean polarization P decays to zero at a temperature T_F which is well below T_m. Unlike the sharp transition materials there are no abrupt changes and non linearity persists to temperature well above T_m.

The original explanation offered by Bokov and Mylnikova[50] for this behavior was that the diffuseness was again due to heterogeneity, giving a range of Curie points, but that now the scale was very small and therefore below the resolution of X-ray and optical probes,. Considering this model of nano-scale polar regions, it appeared probable to use that since the energy barriers to reorientation in any ferroelectric are linearly related to the volume, at these very fine scales the electrocrystalline anisotropy energy ΔH_r might become comparable to kT leading to super-paraelectric behavior at higher temperature.

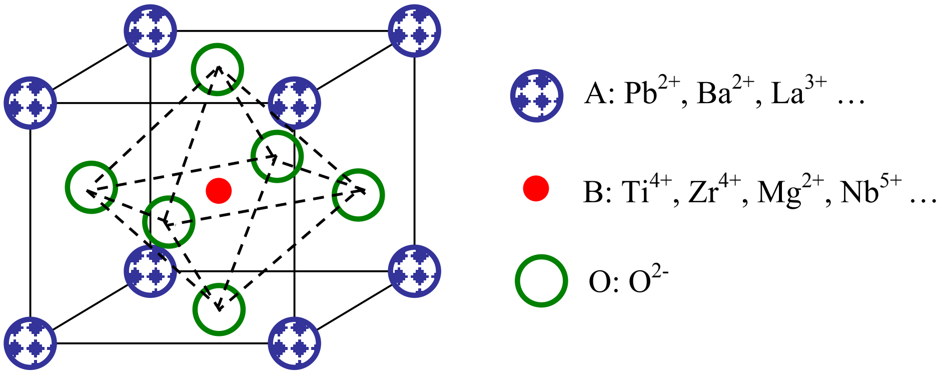

ABO_3 Unit Cell

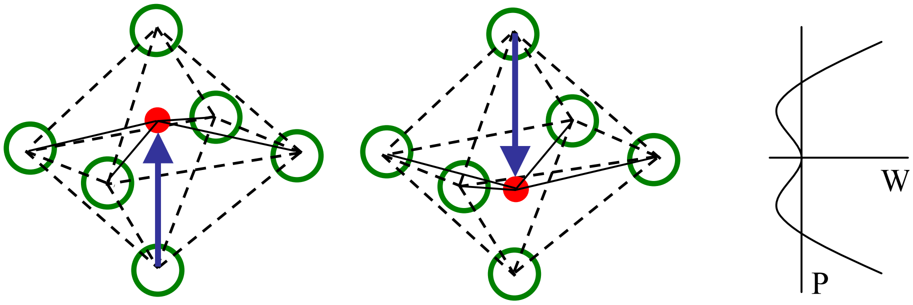

Polarization Up Polarization Down Energy State

Figure 2.5: Perovskite ABO_3 unit cell. Illustrating 180° polarization reversal for two of the six possible polarization states produced by displacement of the central cation in the tetragonal plane.

2.1.3 Perovskite Structure, Principal Ferroelectric Ceramics, and their Applications

The interesting oxygen octahedron structures which show strong ferroelectric properties with high usable temperature ranges are all based upon corner linking of oxygen octahedral. Four groups of most important of these structures are described in Figure 2.2, which are (1) the tungsten-bronze group, (2) the oxygen octahedral group, (3) the pyrochlore group, and (4) the bismuth layer-structure group. Of these, the second group (ABO_3 perovskite type) is by far the most important category economically. The families of compositions listed ($BaTiO_3$, PZT, PMN, PT, and $(Na,K)NbO_3$) represent the bulk of the ferroelectric ceramics manufactured in the world today.

A typical ABO_3 unit cell structure is given in Figure 2.5. In this structure, B^{x+} is usually much smaller than A^{y+} and O^{2-} and it occupies the corner-linked network of oxygen octahedral. Because of size mismatch, local dipole-dipole coupling, and local static electric interaction, there are two stable positions for B^{x+} as illustrated in Figure 2.5 and they are not in the center of oxygen octahedral. B^{x+} can switch between these two positions easily since the energy needs to be overcome is very low. Due to this feature, spontaneous polarization can occur more easily in perovskite type crystal structure than other crystal structures.

Table 2.1: Compositions and properties of typical ferroelectric ceramics

Composition	**Density (g/cm^3)**	**T_C (°C)**	**ε**	**k_{33}**	**d_{33} $\times10^{-12}$ (C/N)**	**g_{33} $\times10^{-3}$ (V(m/N))**	**M_{11} $\times10^{-16}$ (m^2/V^2)**
$BaTiO_3$	5.7	115	1700	0.5	190	11.4	
PZT-4	7.5	328	1300	0.7	289	26.1	
PZT-5A	7.8	365	1700	0.71	374	24.8	
PZT-5H	7.5	193	3400	0.75	593	23.1	
PMN-PT(65/35)	7.6	185	3640	0.70	563		
PMN-PT(90/10)	7.6	40	24000	0	0	0	3.6
$PbNb_2O_6$	6.0	570	225	0.38	85	43.1	
$(Na_{0.5}K_{0.5})NbO_3$	4.5	420	496	0.61	127	29.5	
PLZT 7/60/40	7.8	160			710	22.2	
PLZT 8/40/60	7.8	245	980				
PLZT 12/40/60	7.7	145	1300		235	12	
PLZT 7/65/35	7.8	150	1850		400	22	
PLZT 8/65/35	7.8	110	3400		682	20	
PLZT 9/65/35	7.8	80	5700	0	0	0	5.8
PLZT 9.5/65/35	7.8	75	5500	0	0	0	
PLZT 7.6/70/30	7.8	100	4940				
PLZT 8/70/30	7.8	85	5100	0	0	0	11.7

Table 2.1 is a list of major industrialized ferroelectric materials and their properties. According to composition, these materials can be categorized into three groups, $BaTiO_3$, PZT or PLZT, PMN or PMN-PT.

(1) $BaTiO_3$

$BaTiO_3$ is the first piezoelectric transducer ceramic ever developed; however, its use in recent years has shifted away from transducers to an almost exclusive use as high-dielectric constant capacitors of the discrete and multilayer (MLC) types. The reason for this are primarily twofold: (1) its relatively low T_c of 120ºC, which limits its use as high-power transducers, and (2) its low electromechanical coupling factor in comparison to PZT (0.35 vs 0.65), which limits its operational output.

When $BaTiO_3$ is used in its primary application as a capacitor, a different group of additives is used, because the intent in this case is to suppress the ferroelectric and piezoelectric properties as much as possible while maintaining or increasing its dielectric constant. Two general types of modifiers are commonly used: T_C shifters and T_C depressors. The T_C shifters, such as $SrTiO_3$, $CaZrO_3$, $PbTiO_3$, and $BaSnO_3$, have the effect of shifting T_C to a higher or lower value, depending on the intended result. However, it is usually the case that a lower T_C is desired, such that the higher permittivity values associated with the T_C occur nearer room temperature or the temperature of operation. Depressors, such as $Bi_2(SnO_2)_3$, $MgZrO_3$, $CaTiO_3$, $NiSnO_3$, as well as the shifters, are added in small (1–8 wt%) quantities to the base $BaTiO_3$ composition to lower or depress the sharpness of the dielectric constant peak at the T_C, thus giving a flatter dielectric constant–temperature profile. The net results of these efforts is to produce ceramic capacitors with dielectric constants up to 3000, loss tangents of ~1% or less, and temperature stabilities of ±15% for the X7R-type capacitors. Higher dielectric constants (to 12 000) can be achieved with a concurrent loss in temperature stability (+22%/-56%) for the Z5U-type capacitor, as designated by the Electronic Industries Association (EIA).

(2) PZT

PZT is mainly used for transducer applications. This is because PZT (1) possess higher electromechanical coupling coefficients than $BaTiO_3$, (2) have higher T_C values, which permit higher temperatures of operation or higher temperatures of processing during the fabrication of devices, (3) can be easily poled, (4) possess a wide range of dielectric constants, (5) are relatively easy to sinter at lower temperatures than $BaTiO_3$, and (6) form solid-solution compositions with many different constituents, thus allowing a wide range of achievable properties.

PZT is almost always used with a dopant, a modifier, or other chemical constituent or constituents to improve and optimize their basic properties for specific applications. Examples of these additives include off-valent donors, such as Nb^{5+} replacing Zr^{4+} or La^{3+} replacing Pb^{2+}, to counteract the natural p-type conductivity of the PZT and, thus, increase the electrical resistivity of the materials by at least 3 orders of magnitude. The donors are usually compensated by A-site vacancies. These additives (and vacancies) enhance domain reorientation; ceramics produced with these additives are characterized by square hysteresis loops, low coercive fields, high remnant polarization, high dielectric constants, maximum coupling factors, higher dielectric loss, high mechanical compliance, and reduced aging.

Off-valent acceptors, such as Fe^{3+} replacing Zr^{4+} or Ti^{4+}, are compensated by oxygen vacancies and usually have only limited solubility in the lattice. Domain reorientation is limited, and, hence, ceramics with acceptor additives are characterized by poorly developed hysteresis loops, lower dielectric constants, low dielectric losses, low compliances, and higher aging rates.

Isovalent additives, such as Ba^{2+} or Sr^{2+} replacing Pb^{2+} or Sn^{4+} replacing Zr^{4+} or Ti^{4+}, in which the substituting ion is of the same valency and approximately the same size as the replaced ion, usually produce inhibited domain reorientation and poorly developed hysteresis loops. Other properties include lower dielectric loss, low compliance, and higher aging rates.

Dopants are usually added in concentrations of ≤ 3 at.%. Modifiers are substituted into the original PZT composition as solid-solution constituents in concentrations of ≥ 5 at.%. The most common examples of modifier systems are $(Pb,La)(Zr,Ti)O_3$, $(Pb,Sr)(Zr,Ti)O_3$, $(Pb,Ba)(Zr,Ti)O_3$, $Pb\text{-}(Zr,Ti,Sn)O_3$, $(Pb,La)TiO_3$, and $Pb(Mg,Nb)O_3$–$PbZrO_3$–$PbTiO_3$, although, in actuality, there are many of these lead containing, solid-solution systems. One system that embraces all compositional aspects of the dielectric, piezoelectric, pyroelectric, ferroelectric, and electrooptic ceramics is the PLZT system. Modification of the PZT system by the addition of lanthanum sesquioxide has a marked beneficial effect on several of the basic properties of the material, such as increased squareness of the hysteresis loop, decreased coercive field, increased dielectric constant, maximum coupling coefficients, increased mechanical compliance, and enhanced optical transparency.

(3) PMN or PMN-PT

PMN belong to the category of relaxor. Its study began from early 1960s with work on single-crystal PMN and continued in the mid-1960s with PMN as one of the triaxial components in the PZ-PT-PMN solid-solution system, more recent work in the early 1980s with PMN based ceramics has led to their successful application as high-strain electrostrictive actuators and high dielectric constant capacitors, in late 1990s, the successful growth of practical size PMN single crystal with extremely high dielectric constant and electro-mechanical coefficient lead to their application as high end actuators and electro-optic devices.

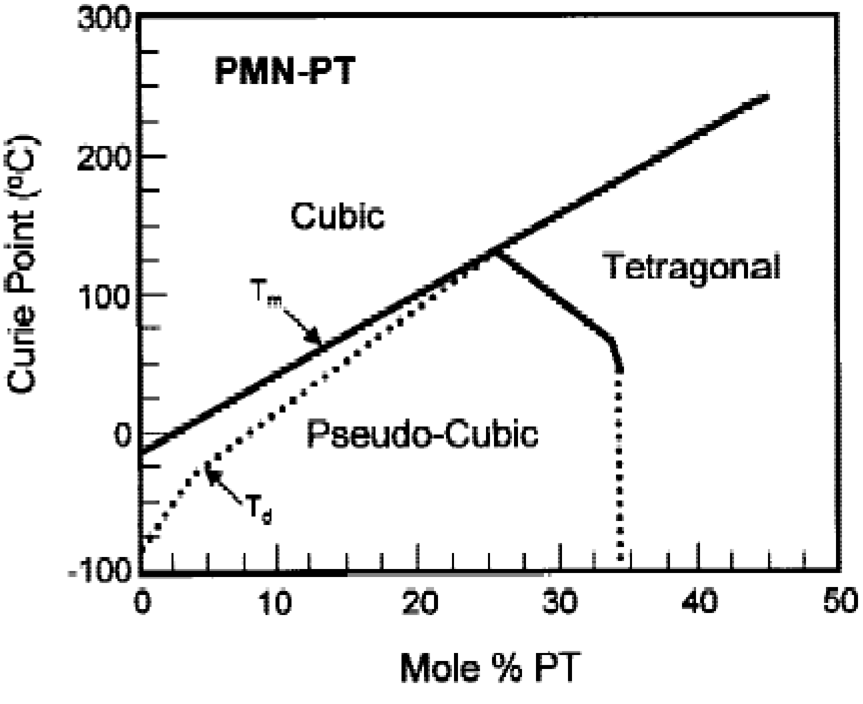

Figure 2.6: Phase diagram of PMN-PT [51]

Usually PMN is utilized in the form of PMN-PT solid solution. Figure 2.6 is the phase diagram of PMN-PT. The most widely studied and utilized compositions are 0.9PMN-0.1PT and 0.65PMN-0.35PT. At 0.9PMN-0.1PT, the temperature of maximum dielectric constant and maximum electrostrictive coefficient is at the range of room temperature. So this composition is mainly utilized as capacitors and electrostrictive actuators. The composition of 0.65PMN-0.35PT is near the so-called morphotropic phase boundary (MPB). It is the phase transformation boundary between Pseudo-Cubic (Rhombohedral) and Tetragonal and also the transformation boundary between relaxor and regular ferroelectric. The piezoelectric coefficient is very high at this MPB composition and is mainly utilized as actuators.

2.2 Colloidal Particles Interaction and Stability

In Chapters 3 and 4 of this thesis, colloidal coating processing and its simulation will be studied. These studies are based on the basic principles of colloidal interaction in solution. The concepts of these basic principles will be briefly introduced here as the fundamental of further studies. These are within the framework of colloidal chemistry.

During the studies of colloidal particles behavior in solution, it is found that both attraction and repulsion exists between particles as described in Figure 2.7 (a). Both attraction and repulsion decrease with the distance of separation between the bodies involved. Figure 2.7(b), Figure 2.7(c), and Figure 2.7(d) are the different scenarios for the combination of the attraction and repulsion force. In Figure 2.7 (b), the attraction is stronger than repulsion. So the bodies involved are in lower energy state if they move together. Therefore flocculation will occur in this condition. On opposite, repulsion is stronger than attraction in Figure 2.7 (d). So it is more stable for the bodies involved to keep a distance with each other. Therefore stable colloidal state can be achieved without flocculation in this condition. Figure 2.7 (c) is an intermediate state, in which attraction and repulsion each have regions of dominance. In this case, there are a shallow minimum at large separation and a deep minimum at small separations. In order to reach stable deep minimum condition an energy barrier need to be overcome. Such a system may be viewed as metastable, possessing a degree of kinetic stability even though it lacks thermodynamic stability: that is flocculation is predicted, but it is expected to occur slowly. The attraction and repulsions force originate from a variety of reasons. 2.2.1 discusses three types of intermolecular force that cause attraction between colloidal particles. Collectively, these are known as van der Waals forces. 2.2.2 discusses the origination of repulsion force.

2.2.1 Attraction

To understand the origin of the attraction between colloidal particles, it is necessary to consider the interactions between individual molecules. Basically the majority of attraction between individual molecules comes from the following originations: (1) ion and ion columbic interaction; (2) ion and permanent dipole interaction; (3) permanent dipole and permanent dipole interaction; (4) permanent dipole and induced dipole attraction (Debye); (5) induced dipole and induced dipole attraction (London); (6) attraction between permanent dipoles with free rotation (Keesom). Among which (1), (2), and (3) could be both attraction and repulsion, depending on the charge of ions or the orientation of the dipoles, or both. By contrast (4), (5), and (6) are always attractive.

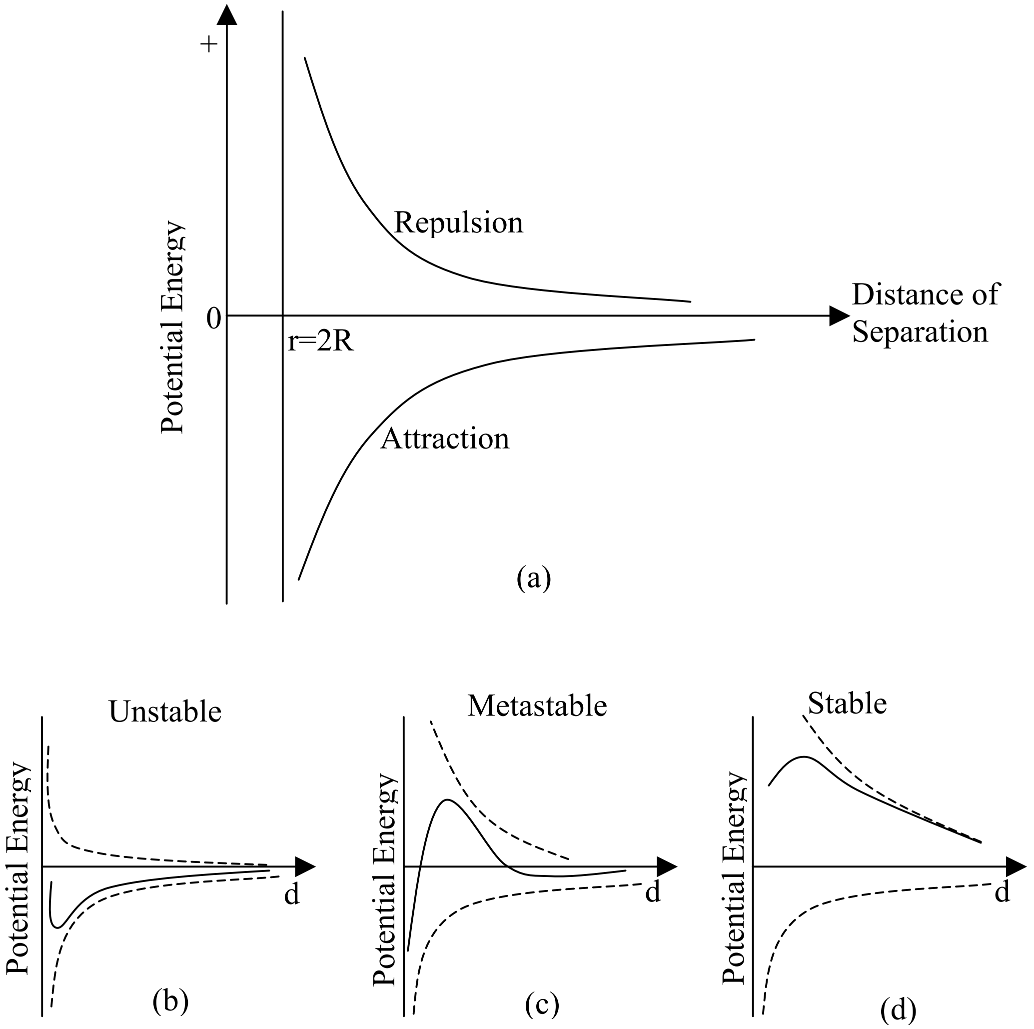

Figure 2.7: Potential energy curves for the interaction of two colloidal particles. Negative values correspond to attraction, and positive values to repulsion. (a) Definition of variables. (b) Repulsion less than attraction in magnitude and/or range. (c) Repulsion and attraction comparable in magnitude and range. (d) Attraction less than repulsion.

For (4) Debye attraction:

$$\Phi_D = \frac{(\alpha_{0,1}\mu_2^2 + \alpha_{0,2}\mu_1^2)}{(4\pi\varepsilon_0)^2 x^6} \tag{2.6}$$

For (5) London attraction:

$$\Phi_L = -\frac{2h}{3}\frac{\nu_1\nu_2}{\nu_1+\nu_2}\frac{\alpha_{0,1}\alpha_{0,2}}{(4\pi\varepsilon_0)^2 x^6} \tag{2.7}$$

For (6) Keesom attraction:

$$\Phi_K = -\frac{2}{3}\frac{\mu_1^2\mu_2^2}{(4\pi\varepsilon_0)^2 k_B T x^6} \tag{2.8}$$

Where α is polarizability, it is always negative. ν is characteristic vibrational frequency of electrons. This set of attractive interactions is collectively known as van der Waals attractions. They all involve an inverse sixth-power law. Collectively van der Waals attraction has the following relationship with distance x:

$$\Phi = \Phi_D+\Phi_K+\Phi_L = (\beta_D+\beta_K+\beta_L)x^{-6} = \beta x^{-6} \tag{2.9}$$

On the equation above, the expression is for the attraction between individual dipoles. The inter-particle attraction is a combination of these attractions between individual molecules:

$$\Phi_{\text{attraction}} = \iint -1/2(\frac{\rho N_A}{M})^2 \beta \frac{dV_{particle1}dV_{particle2}}{x^6} \tag{2.10}$$

Where $\rho N_A/M$ is the number of molecules per volume in the particle. It is traditional to designate $(\frac{\rho N_A \pi}{M})^2 \beta$ as the Hamaker constant A. The Hamaker constant has the unit of energy and is generally tabulated for different materials. It is a parameter that represents the relative strength of attraction. Its value depends on the particles material, medium between the particles and temperature, but independent of particles geometry.

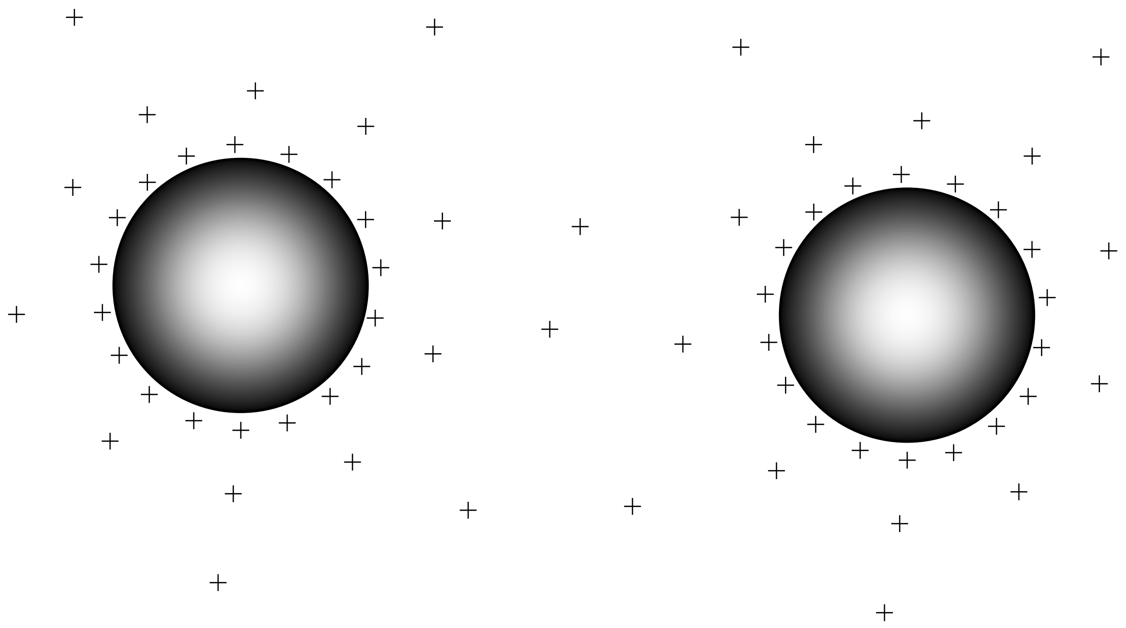

Figure 2.8: Colloidal particle surface charge distribution in solution

2.2.2 Repulsion

For a medium like water, both anion and cation exist in it. Anions could be OH^- or others from solvent. Cations could be H^+ or others from solvent. When bodies like particles present in the media, an interface exists. Both anion and cation have the tendency to be adsorbed to the interface. In most situations, the ability of anion and cation being adsorbed to the interface are different. So the charges on the surface tend to be unbalanced as Figure 2.8. In colloidal chemistry, the charged interfacial region is called electrical double layer. Because the bodies with the same materials will have the same type of charge on the surface, repulsion exists between them. The magnitude of repulsion depends strongly on the geometry of particles and shape of the double layer. It is hard to describe it in an equation. The following is an expression, after many approximations, for the most common case of repulsion between two spherical particles of diameter a and a distance x between their surface:

$$\Phi_{repulsion} = \frac{\pi\varepsilon_0\varepsilon_r a^2\psi_0^2}{(x+a)}\exp(-kx) \qquad (2.11)$$

for small particles with a large double layer.

$$\Phi_{repulsion} = \pi\varepsilon_0\varepsilon_r a\psi_0^2 \ln[1+\exp(-kx)] \qquad (2.12)$$

CHAPTER 3: MONTE-CARLO SIMULATIONS OF SOL-GEL COATING ON COLLOIDAL PARTICLES

The central idea of this thesis is to produce perovskite phase PMN-PT by coating $Mg(OH)_2$ on the surface of Nb_2O_5 to improve contact and reactivity between the various elements. To realize this, a fundamental understanding of colloidal coating that can be utilized to devise a method to coat $Mg(OH)_2$ on Nb_2O_5 is needed. In this chapter, we will examine the coating in a colloidal suspension and the various factors that affect the coating quality using numerical simulations. Since colloidal coating is a general technique that can be applied to different materials systems, the coating simulations will be carried out from a more general and fundamental point of view. The specific experimental detail of how to coat $Mg(OH)_2$ on Nb_2O_5 will be described in next chapter.

3.1 Introduction

It has been showed that coating was a good way of modifying particle surface property and the structure and the composition of ceramics on the microscale. For example, Shih et al[52, 53] developed a sol-gel coating technique to distribute the additives onto the surface of silicon nitride. They showed that the coating approach not only distributes additives uniformly, but also the boehmite (AlOOH) coating improves the rheological and consolidation properties of silicon nitride particles. Hu et al[54] obtained uniformly distributed nearly fully dense ZnO and ZrO_2 composite ceramics by coating ZnO on the surface of ZrO_2.

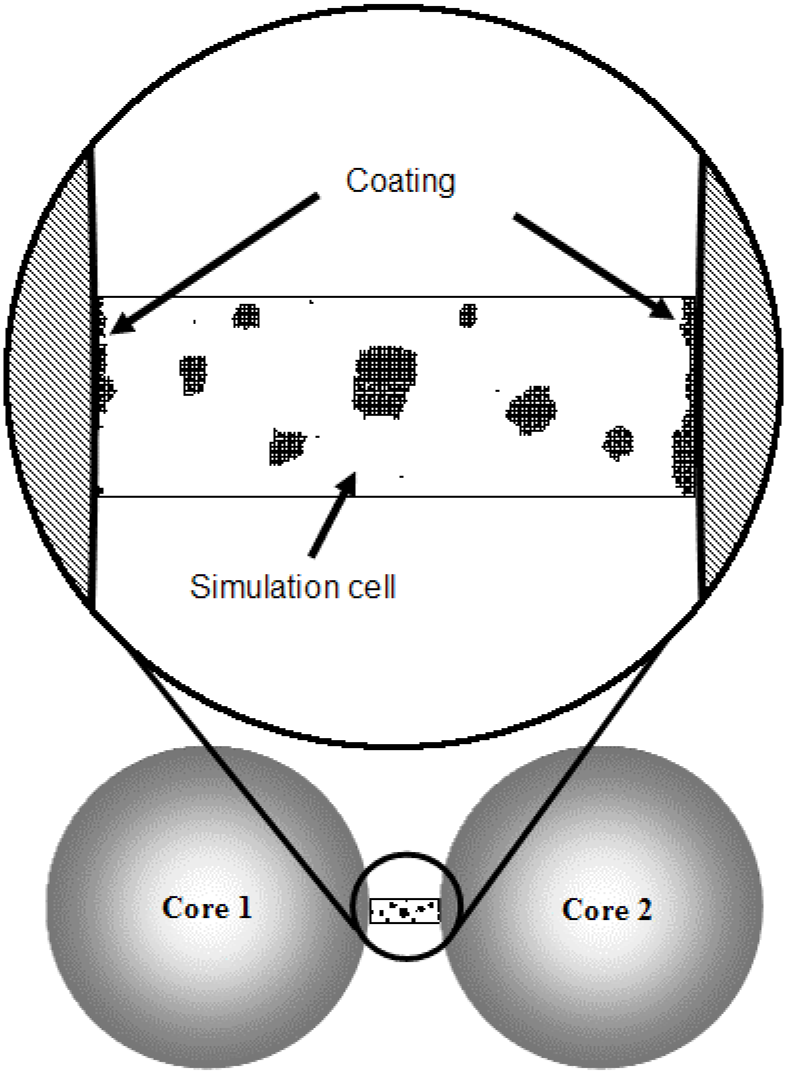

Figure 3.1: Snapshot of colloidal coating simulation by Yang et al. The black dots in the "Simulation cell" represent the coating species precipitation units or monomers. Coating occurred when the coating-species attached to the left or right walls. The aggregation of the coating species in the solution is regarded as precipitations.

The colloidal method is an important way of coating one species onto another. So far, coating has been achieved on a variety of particles with the colloidal method. For example, Yang et al[55] coated boehmite (AlOOH) on the surface of SiC; Ohmori et al[56] coated SiO_2 on the surface of spindle-type hematite particles; Haq et al[57] coated TiO_2 on the surface of Cu compounds. Although coating by a colloidal method has been carried out in a number of materials systems, there have been very few published theoretical or simulation studies about colloidal coating. Yang et al[58] first studied the colloidal coating by numerical simulations using a modified Shih-Aksay-Kikuchi (SAK) model[59] where they used the walls on the right and left edges of the simulation cell to represent the surface of the core particles and the black dots in the simulation cell to represent the coating species (see Figure 3.1). As described by the authors, the SAK model is a reversible-growth model, which allows colloidal particles and clusters to aggregate via the cluster-cluster aggregation mechanism, while taking into account the effect of a finite interparticle attraction energy that allowed particles to unbind from a cluster. These features enabled the model to be able to simulate a wide range of colloidal phenomena from aggregation, dispersion, micro-phase separation to colloidal coating. Using this model, Yang et al successfully demonstrated that under high particle surface charge (away from IEP) conditions, coating thickness first increased with the coating species concentration and became saturated when the coating species concentration reached a certain level. In addition, the simulations showed that only when the attraction energy between the coating species and the core species was larger than or equal to the attraction energy between the coating species themselves, complete coverage could be achieved. However there are still some limitations in his model. For example, using the cell walls to represent core particle surfaces assumed that the core particles were infinitely large. Meanwhile, since the core particles were not realistically represented, the core particle concentration could not be changed and the distance between the core particle surfaces was fixed. Therefore, the model only represented the colloidal coating processes in a very limited space between two very large particles with a fixed distance as shown in Figure 3.1.

In this chapter, based on the SAK model, we constructed a more realistic model that could examine the effects of the core particle size, the core particle concentration, and the coating species concentration. Periodical boundary conditions were used, so that the simulations can represent a larger system.

The model we used is also based on the Shih-Aksay-Kikuchi (SAK) model,[59, 60] which has been used to study the effect of finite inter-particle attraction energy on the fractal dimension of colloidal aggregates,[59, 60, 61] the effect of restructuring on the structure of particulate networks,[62, 63] the stability of binary colloidal suspensions with depletion flocculation and depletion restabilization,[64, 65] and heterogeneous aggregation.[66] Recently, Yang et al used this model to study the nucleation and growth process of colloidal particles,[67] and to simulate coating in a colloidal suspension assuming the core particles size was much larger than the coating thickness.[58] The advantage of the SAK model is that it allows both aggregation and relaxation by energetic considerations, so it can simulate both particle formation and dissolution, and hence give a more accurate picture of the process dynamics in colloidal systems. Because of this feature and its success in multiple colloidal simulation systems mentioned above, it is realistic to construct a new colloidal coating model based on this SAK model.

Once the coating model is constructed, we will use it to demonstrate the micro-process of colloidal coating. Also, we will use it to examine the factors that affect the precipitation of the coating species and the coating thickness. In the experiments, it was found that in some conditions all the coating species coated the core surface, in other conditions besides coating the core surface they also precipitated and form agglomerates.[56, 58] For most applications, it is preferred to have all the coating species coat the core surface. Experimentally, it was found that the precipitation of the coating species occurred when the coating species concentration was high. At the same time, the coating thickness saturated above a certain coating species concentration. Exactly how the saturation concentration and the saturated coating thickness were affected by the experimental factors was not well understood. For example, if the mole ratio between the coating species and the core particles must be fixed as required by the applications, it is not clear how one can change other experimental conditions to have the entire coating species coat the core particle surface. Simulations will help answer such questions.

3.2 Model

The model was extended from the SAK model and was simulated on a two dimension square lattice as illustrated in Figure 3.2. For convenience, the lattice constant of the underlying square lattice was defined as unity. As has been shown in the previous studies based on the SAK model, the two-dimensional simulations were sufficient to illustrate the physics involved. In the square lattice, each lattice point can be occupied by one monomer or precipitation unit, which is the smallest unit in our simulation system. In principle, the monomers may represent the individual molecules or atoms. However, this would require a large number of monomers that is beyond the present calculation power. For practicality, the monomers or precipitation units represent microscopic or mesoscopic clusters of atoms or molecules that further aggregate to form colloidal particles. In Figure

3.2 and other illustrations, black dots were used to represent core-species monomers and gray dots to represent coating-species monomers. Correspondingly, we also use the subscript "1" to represent the core species and the subscript "2" to represent the coating species. If two or more monomers collide, they formed a particle or clusters, which represented colloidal particles in the experiments.

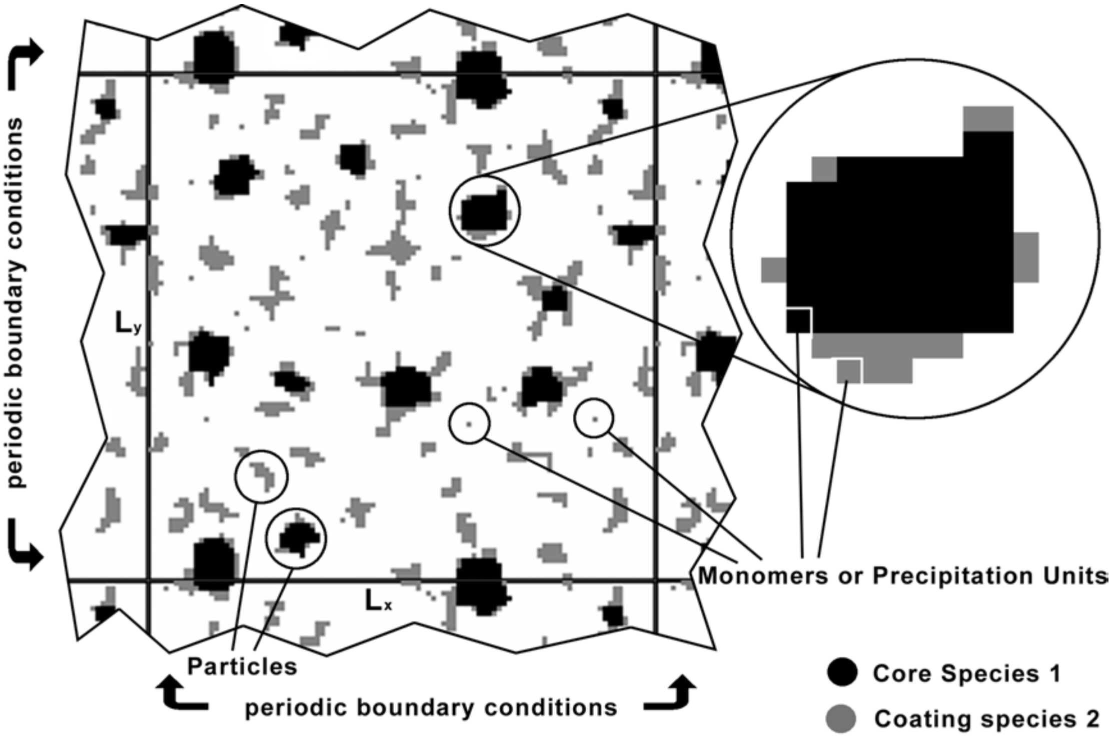

Figure 3.2: A schematic of the simulation cell. The gray dots represent the coating species. The black dots represent the core species.

Initially, as illustrated in Figure 3.2, N_1 core particles that contained a total of M_1 monomers were randomly distributed in an $L_x \times L_y$ lattice simulation cell. The N_1 core particles were generated by aggregating the randomly introduced core monomers. The detail will be described in the next section. The core particle average diameter can be approximated with $(M_1/N_1)^{1/2}$. Then M_2 coating monomers were randomly introduced into the simulation cell. The total starting coating monomer concentration was $M_2/(L_xL_y)$. After a time interval τ_D, each monomer moved to one of its empty neighboring sites randomly to simulate diffusion. When a monomer moved next to another monomer or particle, they formed a bigger particle as illustrated in Figure 3.3 (a). At the same time, particles could also diffuse randomly. According to the Einstein relationship, the diffusion coefficient is inversely proportional to radius of the particles, the time interval for a particle of m monomers to diffuse as a whole by one lattice constant is determined to be $m^{1/2}\tau_D$. When a particle moves next to other particles or monomers, they also formed a bigger particle. If the coating species monomers or particles move to the surface of core particles and attached there, the cluster formed on the core particle surface was referred to as the coating layer. If all core particles surface were covered with the coating monomers, we called it complete coverage. Meanwhile, between monomers, we considered a nearest-neighbor finite attraction energy, -E. We used E_{11}, E_{22}, E_{12} to represent the attraction energy between two core monomers, that between two coating monomers, and that between a coating monomer and a core monomer, respectively as illustrated by Figure 3.3 (a). Because E was finite, the bonds between a monomer and its neighbors within a particle could break by thermal agitation as illustrated in Figure 3.3 (b). The probability for a monomer to break the bonds with its neighbors and move to one of its unoccupied neighboring sites at random was determined by the Boltzmann factor $(1/\tau_R)\exp(-\Delta E/k_BT)$, where ΔE was the change in energy due to the movement and $1/\tau_R$ is the unbinding attempt frequency. If a monomer is surrounded by four neighbors within a cluster, it will not be able to break up with it neighbors because it did not have an unoccupied neighboring site to move to after the breakup. As what Yang et al[67] has shown that the inter-monomer attraction energy –E is related to the monomer solubility. A large/small E corresponds to a small/large solubility. For example, for the boehmite (AlOOH) coating on SiC system, boehmite becomes more soluble in acidic conditions.[55] Therefore, lowering the pH value is equivalent to decreasing E. In the experiments, core particles were usually added externally and were not soluble in the coating conditions. Therefore, in the coating simulations, we gave E_{11} a very large value to keep the core particles insoluble and in a stable shape.

In this model, the interactions between particles were also considered. According to colloidal chemistry, both attractive and repulsive interactions exist between colloidal particles. The long-range repulsive interactions come from the surface charge. When the surface charge is low (near IEP), the repulsive interaction is weak. Under such conditions, the attractive interaction dominates and particles tend to agglomerate. When the surface charge is high (away from IEP), the repulsive interaction becomes important. In order for particles to aggregate, they must overcome an energy barrier as illustrated in Figure 3.4 (a).[68] The probability for this to happen goes like $P_{agg} \propto \exp(-V_{barrier}/k_BT)$, where $V_{barrier}$ is the height of the energy barrier. The height of the energy barrier strongly depends more on the size of the smaller particle of the two that collide. Thus, the probability for two particles to aggregate decreases sharply as the particle size increases as illustrated in Figure 3.4 (b). In the simulations, two conditions for interparticle interactions were used. One was the attractive condition, under which particles could freely aggregate. We used this to represent low surface charge conditions (near IEP). Another was the repulsive condition. Under the repulsive condition, a cut-off size N_c was set as illustrated in Figure 3.4 (b). When both of the two particles were larger than the cut-off size, they could not aggregate. When one or both of the particles is smaller than the cut-off size, they could aggregate to form a larger particle. We used this to represent high surface charge conditions (away from IEP).

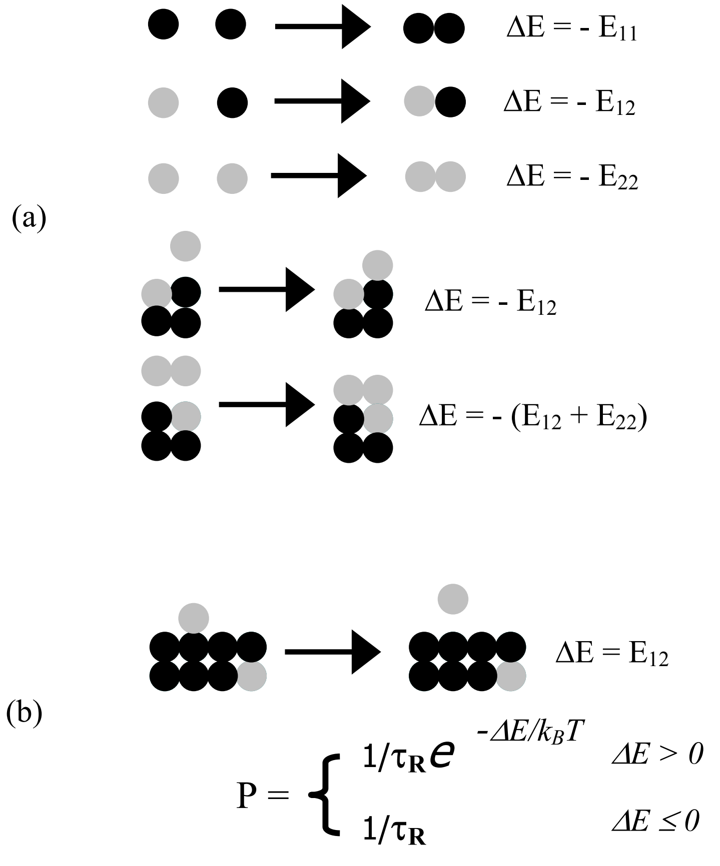

Figure 3.3: Schematics of (a) aggregation, (b) dissolution. The gray dots represent the coating species monomers 1. The black dots represent the core species monomers 2. E is nearest-neighbor attraction energy. τ_D is the diffusion interval.

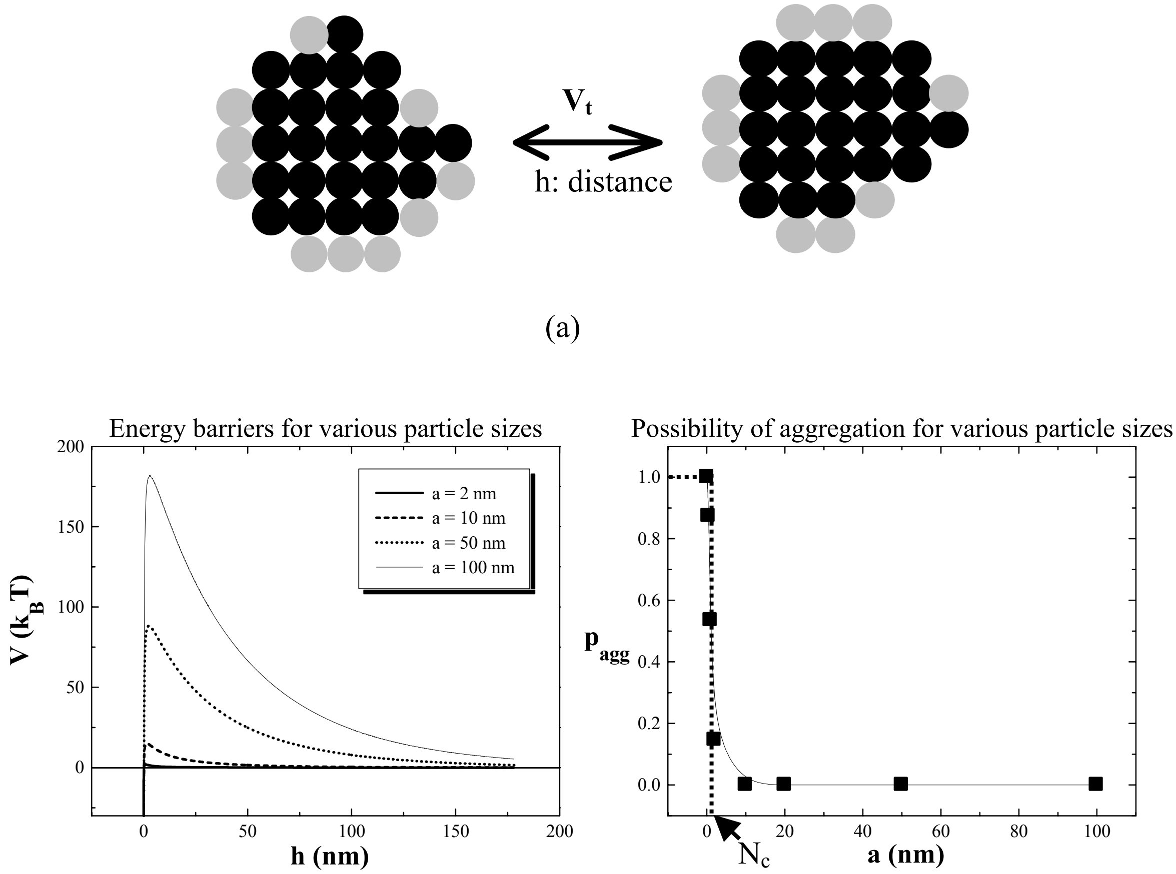

(a)

(b)

Figure 3.4: (a) A schematic shows the interparticles interaction energy, $V_t(h)$ (b) A example of interparticles energy barriers and its possibility of aggregation (P_{agg}).[58] N_C denotes the cut-off size, below which aggregation possibility is 1, above it aggregation possibility becomes 0.

During the simulations, the simulation cell was connected by the periodic boundary conditions so that the simulations can represent a larger system as illustrated in Figure 3.2. Care has been taken to make sure that the simulation cell was large enough to represent a random system. Note that in principle, the time constant τ_D for diffusion and the constant τ_R for the unbinding process could be different. For convenience, we chose

$\tau_D = \tau_R = \tau$, i.e., after every time interval every monomer in the solution attempted random walk once and every monomer in a particle attempted to unbind once.

3.3 Results and Discussion

To examine the coating process, we started with N_1 core particles with a total of M_1 monomers randomly distributed in a 200×200 simulation cell. The N_1 core particles were generated by aggregating the randomly introduced M_1 core monomers with the nearest-neighbor attraction energy E_{11} set to 5 k_BT. Once the core particles were generated, the E_{11} was set to 30 k_BT to ensure the core particles remain insoluble and stable in shape. After the introduction of core particles, M_2 coating species monomers were randomly distributed in the simulation cell. The starting coating monomer concentration was $M_2/40000$. Here we defined the monomer concentration as the number of individual monomers in the solution. Once the simulation starts, the concentration of individual monomers in the solution will decrease as monomers aggregate to form particles (precipitate). After a large number of simulation steps (long time), the monomer concentration will reach a stable value which strongly depends on the E_{22} value, as first shown by Yang et al.[67] The monomer concentration under this stable condition is the equilibrium concentration. Another concentration we used was the total concentration, which represents the total volume fraction of a species in the simulation cell. For example, in our system, the total concentration of the coating species was $C_2=M_2/40000$. For the core species, the total concentration was $C_1=M_1/40000$. The total concentration did not change during the course of the simulation. The particles size was calculated as the square root of the number of monomers (area) in one particle, which approximated the diameter of a particle, d. According the results of Yang et al,[58] to obtain complete coverage, the attraction energy between the coating species and the core species E_{12} must be larger than or equal to the attraction energy between the coating species E_{22}. Therefore, we examined conditions where $E_{12}>E_{22}$ only in this study.

We allowed the simulations to run for a very long time until the solutions reached equilibrium, by which we meant the final monomer concentration reached a constant value and the particle size was stabilized. Here “stabilized” means the average particle size variation is within ±2% compared with a doubled simulation run-time. We studied the temporal evolution of coating suspensions with $C_1=6\%$, $C_2=10\%$, $d_1=6$, $E_{12}=5k_BT$ and $E_{22}=4k_BT$. The snapshots were taken at (a) $t=0\ \tau$, (b) $t=100\ \tau$, (c) $t=10{,}000\ \tau$, (d) $t=100{,}000\ \tau$, and (e) $t=300{,}000\ \tau$. Figure 3.5 shows the simulation results under repulsive conditions (high surface charge). The repulsive cut-off monomer number was 15, which meant two particles did not aggregate when both contained more than 15 monomers. For ease of programming, we used the number of monomers contained in a particle as the criterion for cut-off instead of the particle size. A particle containing 15 monomers is roughly equivalent to a particle of diameter 4. Figure 3.6 shows the results under the attractive condition (low surface charge). For both the attractive and the repulsive conditions, it can be seen that the snapshots shown at $t=100{,}000\ \tau$ and $t=300{,}000\ \tau$ were more or less the same. Also the monomer concentration and the particle size in these two snapshots were almost the same, indicating that the system reached the equilibrium when at $t \geq 100{,}000\ \tau$. In the later part of this chapter, all the results were obtained with t up to $300{,}000\ \tau$.

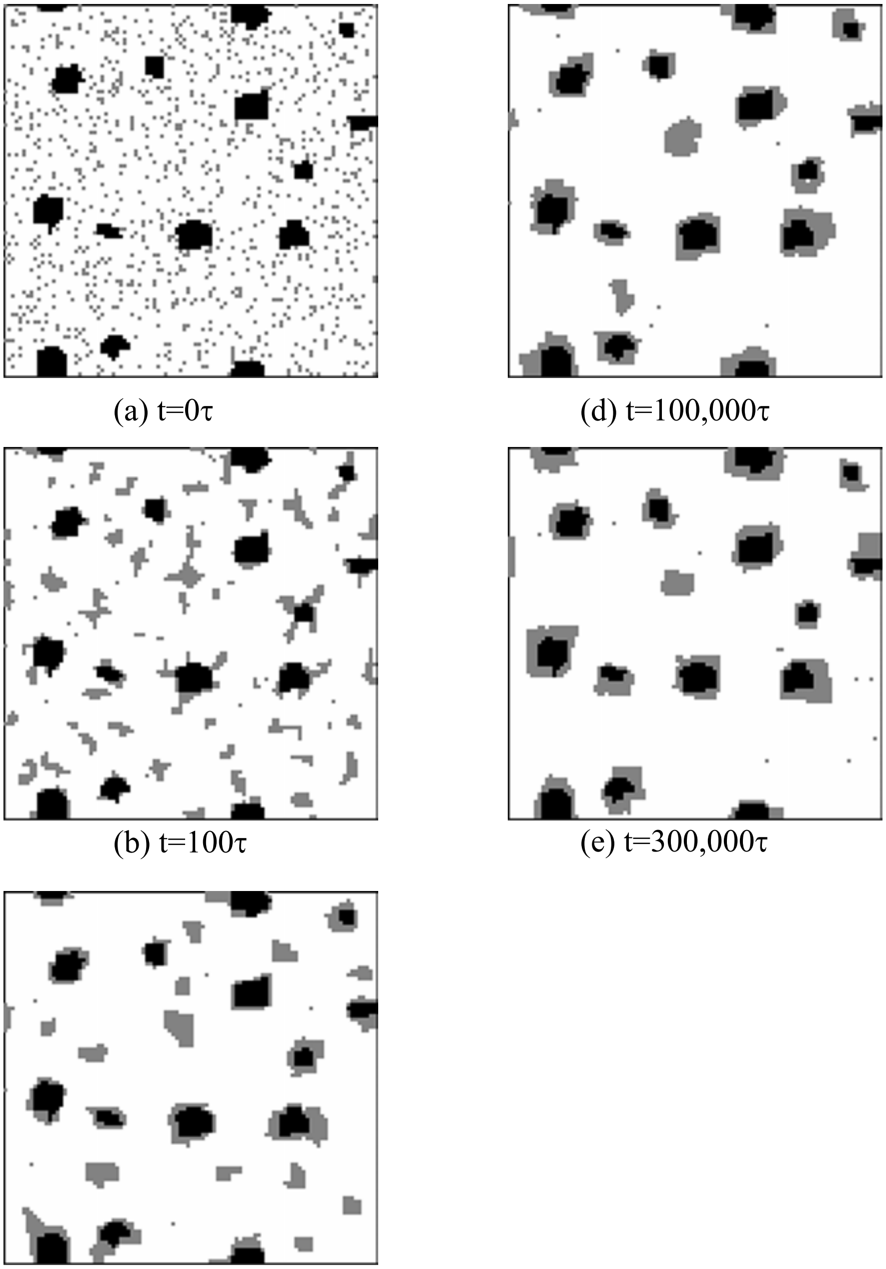

(a) t=0τ

(d) t=100,000τ

(b) t=100τ

(e) t=300,000τ

(c) t=10,000τ

Figure 3.5: Temporal evolution of a coating suspension under the repulsive condition with C_1=6%, C_2=10%, d_1=6, $E_{12}=5k_BT > E_{22}=4k_BT$, at (a)t=0τ, (b)t=100τ, (c)t=10,000τ, (d)t=100,000τ, (e)t=300,000τ

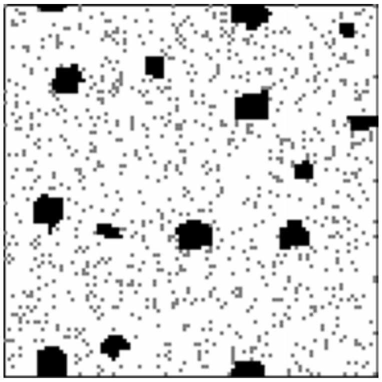

(a) t=0τ

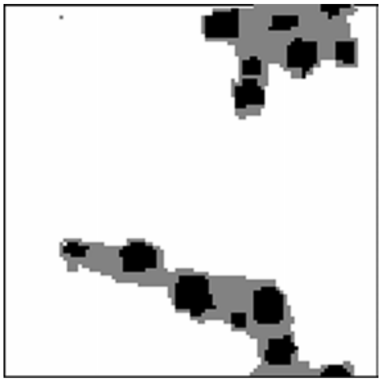

(d) t=100,000τ

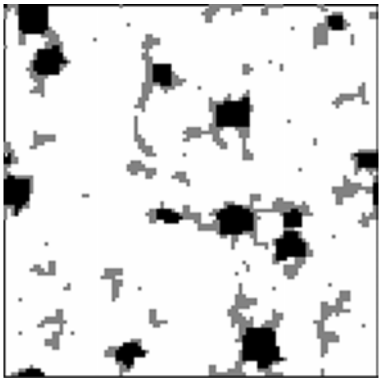

(a) t=100τ

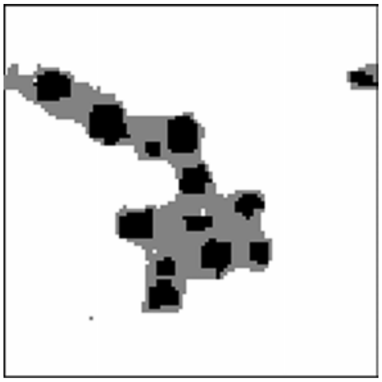

(e) t=300,000τ

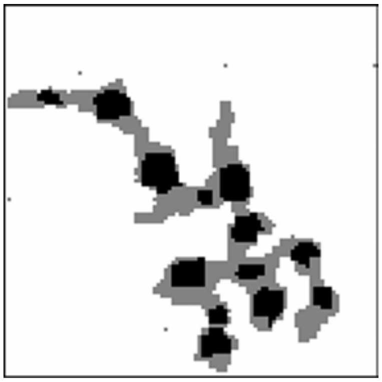

(c) t=10,000τ

Figure 3.6: Temporal evolution of a coating suspension under the attractive condition with C_1=6%, C_2=10%, d_1=6, $E_{12}=5k_BT > E_{22}=4k_BT$, at (a)t=0τ, (b)t=100τ, (c)t=10,000τ, (d)t=100,000τ, (e)t=300,000τ

Figure 3.5 and 3.6 vividly illustrate how the coating species coat the core particle surface. After the coating species monomers were introduced, some went on the core particle surface immediately; others precipitated to form particles of the coating species only. For the attractive conditions, since there existed no repulsive interactions, particles aggregated quickly, and eventually a very large particle formed. These phenomena agreed with experimental results very well. In the experiments, when the suspension was near the IEP, the particles were not stable. They tended to aggregate to form large clusters and settle out. For the repulsive condition, when the particle size was large enough, they could not aggregate because of large repulsive energy barrier. But individual monomers could still dissolve from a particle and re-precipitate on the surface of another particle. According to the Kelvin effect, smaller particles have a higher solubility than a larger particle. The SAK model can simulate this effect as illustrated in the work of Yang et al.[67] As a result, some of the initially precipitated small particles of pure coating species dissolved while larger particles grow. Coated particles with the core inside had a much higher chance to grow bigger than particles of the pure coating species because of the larger initial size and their larger attraction energy to the coating monomers ($E_{12}>E_{22}$). Eventually when the suspension reached a stable condition only the larger particles remained in the suspension as illustrated in Figures 3.5 (d) and (e). The results and analysis above show that the main mass transfer mechanism for the attractive condition was particle aggregation. This happened quickly. The main mass transfer mechanism for the repulsive condition was dissolution and re-precipitation. This process was relatively slow, but it reached an equilibrium state eventually. For the attractive condition, a big chunk formed at the end. Although all the cores were seemingly surrounded by the coating species, this was more the combined result of agglomeration and precipitation, not coating. The later part of this chapter will focus more on studying the repulsive condition.

From Figure 3.5, it was clear that, as the simulation went on, more and more coating was formed on the core particle surface. The coating layer became thicker and more complete. In other words, the quality of coating got better with time. Since the number of simulation steps corresponded to time in the experiment, it can be said that aging helped improving the coating quality (thicker and more uniform), which has been proven by the experiments as Luo et al[69] showed in coating $Mg(OH)_2$ on Nb_2O_5 particles and Ohmori et al[56] showed in coating SiO_2 on spindle-type hematite particles.

Note in Figure 3.5(e) that still one pure coating species particle remained in the simulation cell after 300,000 τ. This was a phenomenon that was also observed experimentally asYang et al[58] showed in the coating of boehmite on SiC. When the boehmite concentration is 5 wt%, all the boehmite were coated on SiC particles. But when the boehmite concentration increased to 15 wt%, pure boehmite particles were observed. Same phenomena were also observed in the coating of SiO_2 on Hematite.[56] Figure 3.7 was the simulation results of this phenomenon. The simulations were done with C_1=2%, d_1=10, E_{12}=5, E_{22}=4 and C_2 varied from 2% to 20%. The simulations were carried out for 300,000 Monte Carlo steps to ensure that the system reached the stable condition. Figure 3.7 shows that that under the repulsive condition (high surface charge), when C_2 was low, all coating monomers went to the surface of core. When C_2 increased, the pure coating species particles started to appear. Figure 3.8 plots the coating thickness versus C_2 for both the attractive and the repulsive conditions. Since the total surface area of the core particles was fixed in this case. If all the coating monomers coated the core particle surface, the coating thickness would increase linearly with C_2. This was described by the attractive condition in Figure 3.8. Under the repulsive condition, the coating thickness initially increased linearly with the increasing of C_2 and saturated at higher C_2. We divided the coating behavior into two regions. One was the linear region where the coating thickness increased linearly with C_2 and no pure coating species particles appeared. Another was the saturated region where the coating thickness increased very slowly with C_2 and particles of pure coating species monomers appeared. We defined the C_2 that particles of pure coating species began to appear as C^* and defined the coating thickness at C^* as T^*. Since for most coating applications, the formation of pure coating species particles were unwanted, it would be very helpful to find the experimental conditions to push both C^* and T^* to higher values. Because of the difficulty of precise parameters control, it is difficult to identify these conditions experimentally. Figures 3.9 and 3.10 are the simulation results of the relationship between C^*, T^* and experimental conditions with the model constructed in this chapter.

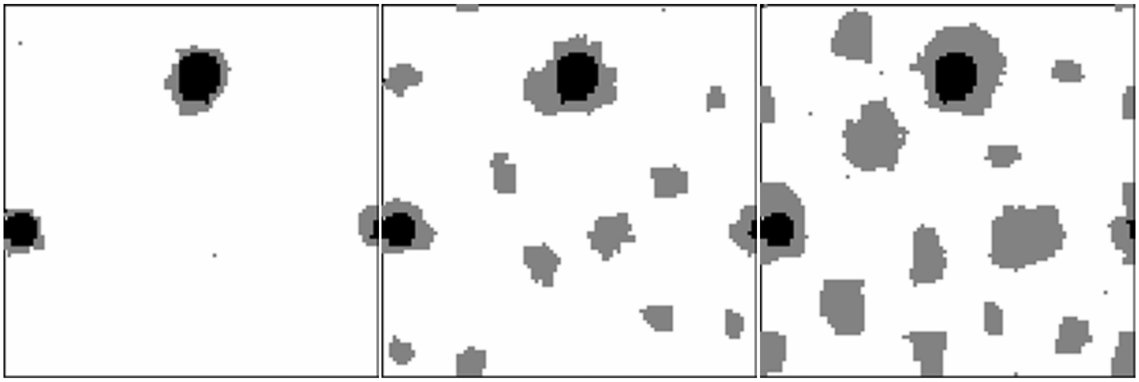

(a) C_2=2% (b) C_2=10% (c) C_2=20%

Figure 3.7: Snapshots of coating simulations under the repulsive condition with C_1=2%, d_1=10, E_{12}=5k_BT, E_{22}=4k_BT, at (a)C_2=2%, (b)C_2=10%, (c)C_2=20%

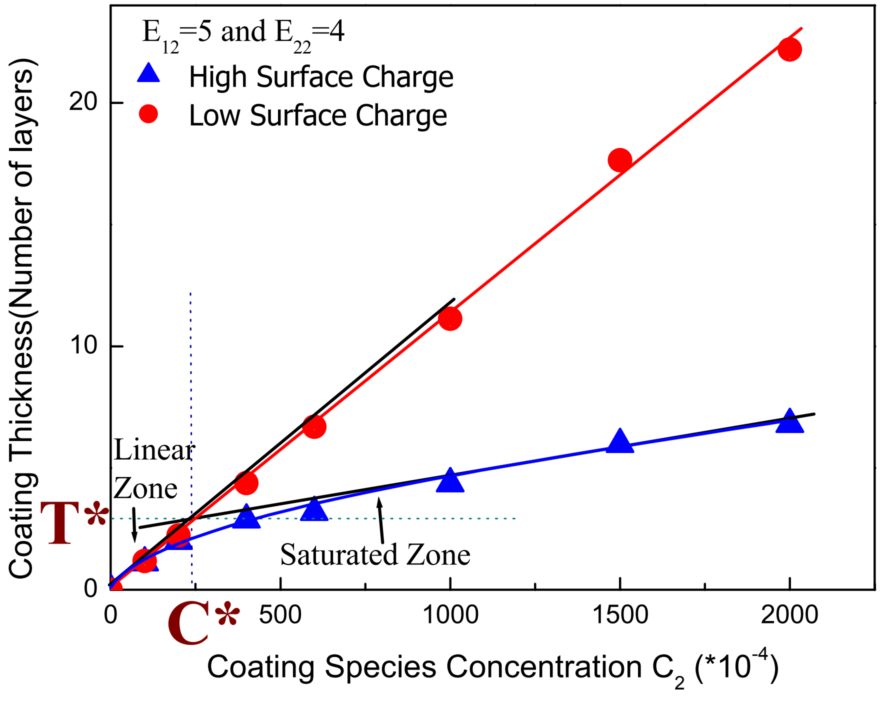

Figure 3.8: Coating thickness versus the starting coating species concentration at C_1=2%, d_1=10, E_{12}=5k_BT, E_{22}=4k_BT. The linear region meant $C_2<C^*$ and saturated region meant $C_2>C^*$ under the repulsive conditions (high surface charge).

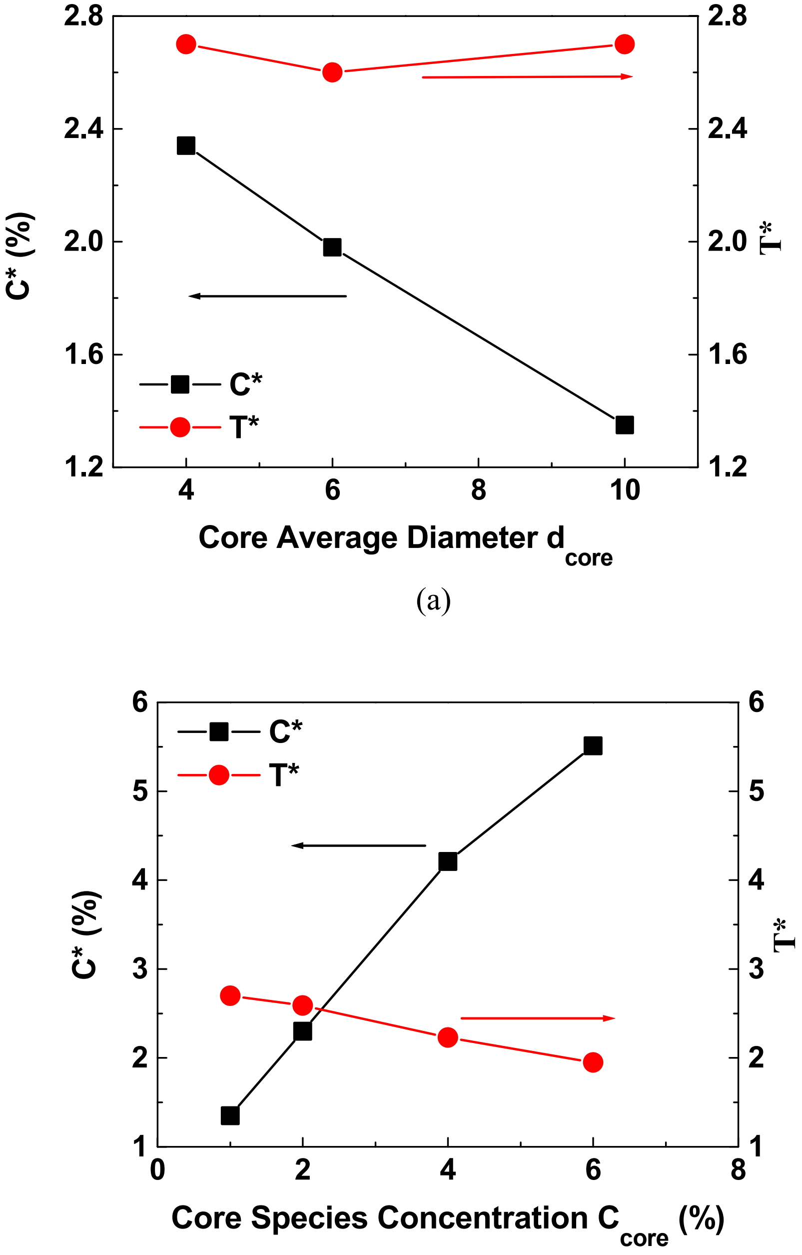

(a)

(b)

Figure 3.9: T^* and C^* versus core particle size where C_1, C_2 were fixed (a), and T^* and C^* versus core species concentration with the core particle size and C_2 fixed (b) at $E_{12}=5k_BT$ and $E_{22}=4k_BT$.

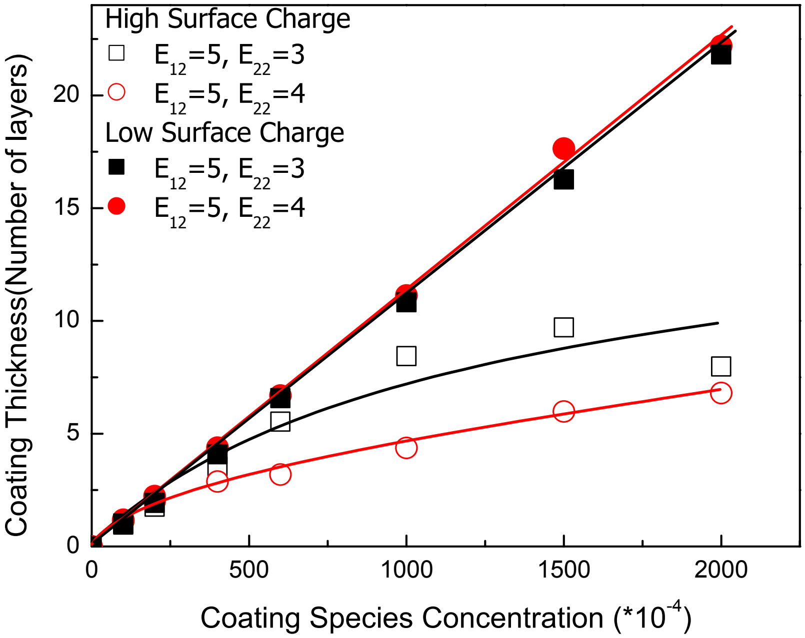

Figure 3.10: Coating thickness versus the coating species concentration at various E_{22} (coating species solubility) where C_1=2%, d_1=10, E_{12}=5k_BT.

Figures 3.9, and 3.10 show $C^*$and T^* versus the core particle size, and $C^*$and T^* versus the core particle concentrations at two different E_{22}. From Figure 3.9 (a), it can be seen that C^* increased with the increase of the core particle size and T^* did not change significantly with the core particle size. Note that, when C_1 was fixed, decrease in particle size increases the number of cores and the core surface area. Therefore, the coating monomers have a much higher probability to collide with a core particle and coat on it instead of forming pure coating species particles. This indicated that smaller core particle size would push C^* higher. Figure 3.9 (b) shows that C^* increased with the increase of C_1 almost linearly and T^* increased slightly with the decrease of C_1. Theoretically, when C_1 increases, the number of the core particles and the core particle surface area also increase.

Similarly, decrease in core particle size increases C^*. Figure 3.10 shows that both C^* and T^* increased with the decrease in E_{22}. Yang et al[58] showed that the inter-monomer attraction energy E was related to the monomer solubility. A lower E meant a lower solubility. Figure 3.10 indicates that a higher coating species solubility will increase T* and C*. In summary, these results indicate that, a smaller core particle size, a higher core particle concentration, and a higher coating species solubility could all help prevent the formation of the pure coating species particles with a fixed coating species concentration C_1.

For many applications, the stoichiometry of the coating species and the core species is fixed. In other words, the mole ratio between the coating species and the core species must be kept constant. From Figure 3.9(a), T^* did not change significantly with the decrease of the core particle size, indicating that, for a fixed amount of the core materials, more coating species will participate as coating before the saturation concentration is reached if the core particles is smaller. Therefore, under stoichiometric conditions, a decrease in particle size will help prevent the formation of particles of pure coating species. According to Figure 3.10, since a higher solubility increases C^* and T^* for a fixed core particle size, it will also help prevent the formation of the pure coating species under stoichiometric conditions.

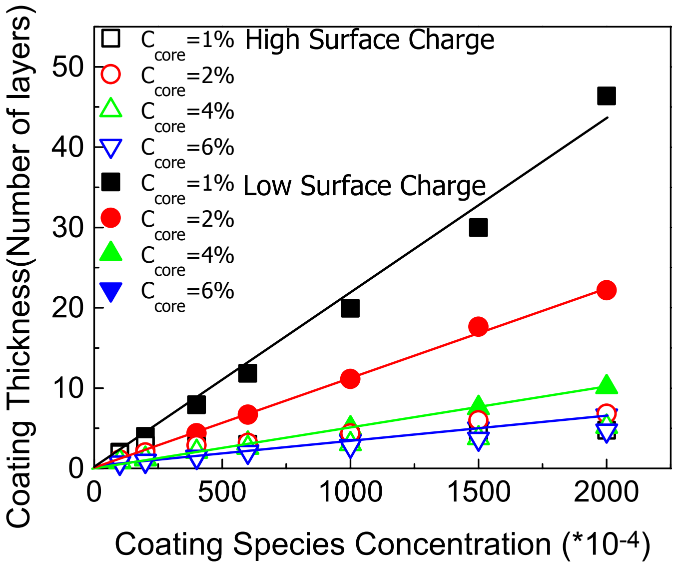

(a)

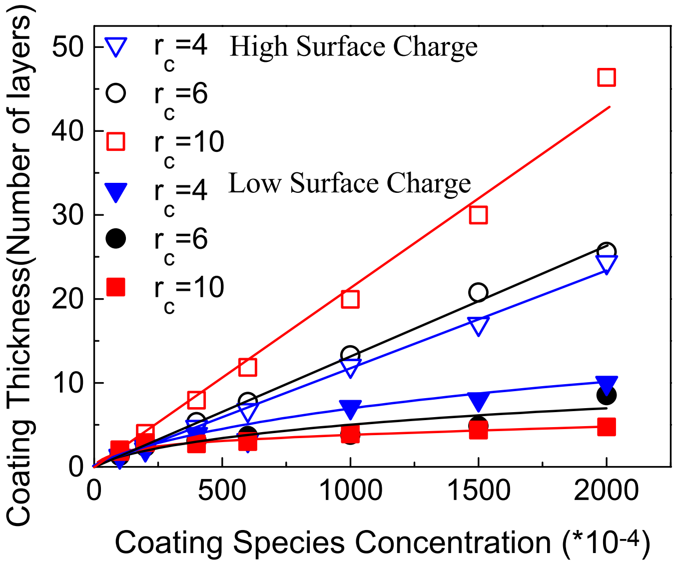

(b)

Figure 3.11: Coating thickness versus the coating species concentration at various core particle sizes with C_1, C_2 fixed (a) and at various core species concentrations with the core particle size and C_2 fixed (b) where $E_{12}=5k_BT$, $E_{22}=4k_BT$.

For completeness, the behavior of linear region and saturation region in Figure 3.8 was also studied. In the linear region, all the coating species monomers were coated on the core particle surface. Understandably, the coating thickness increased linearly with C_2 and decreased linearly with C_1. Note that a decrease in the particle size increased the surface area. Thus, the coating thickness decreased with the decrease of the core particle size. Similar to the linear region, in the attractive conditions, all the coating species monomers were on the core particle surface. Therefore, the average thickness is linear to C_2 as similar to as the linear region under the repulsive conditions, as can be seen in Figures 3.8, 3.10 and 3.11. For the saturation region under repulsive conditions (high surface charge), an increase in C_2 steadily increased the coating thickness as shown in Figure 3.8. Figure 3.10 showed that the increased coating species solubility increased the coating thickness. Figure 3.11 (a) showed that a decreased core particle size increased the coating thickness slightly. Figure 3.11 (b) showed that the coating thickness was not sensitive to the core species concentration. From these results it can be concluded that an increase in C_2, increased the coating species solubility and a decrease in the particle size helped achieve a thicker coating under the repulsive conditions (high surface charge).

3.4 Summary

In this chapter, a Monte Carlo model based on the SAK model was used to simulate coating in a colloidal suspension. Similar to the SAK model, this model considered both the colloidal particles aggregation and took into account the effect of a finite interparticle energy that allowed precipitation units to unbind from a particle. In addition, we included core particles in the simulations to allow multiple species to be realistically represented in a simulation cell. Compared with the previous colloidal coating model,[58] the introduction of both the core and the coating species into the system allows more factors such as the core particle size, the core particle concentration, and the coating species concentration to be considered. This simulation was carried out by starting with pre-generated core particles and randomly distributed coating species monomers in the simulation cell.

Our model has succeeded in reproducing and explaining experimental phenomena. For example both the experimental and simulation results showed that, with a high particle surface charge (a lower aggregation cut-off size), individual coating species particles formed in the solution at a high coating species concentration. Long-time aging could help achieve better coating and possibly eliminate the individual coating species particles. The simulation results revealed that this was due to the coating species monomers mainly precipitated as individual particles at the early stage and the coating was accomplished mainly by the dissolution of the individual particles and the re-precipitation of the monomers on the coating layers. According the Kelvin equation, $\frac{c_s(r)}{c_s(\infty)} = \exp(\frac{2\sigma}{k_B T}\frac{1}{r})$, the difficulty for particles to dissolve and re-precipitate as a coating increase sharply at an exponential relationship with the inverse of the particle size. The requirement to dissolve relative larger individual coating species particle for the case of higher coating species concentration in later stage decreases the possibility of their complete dissolution. Also according the Kelvin effect, the individual coating species particles tends to coat on the core and form larger particles. Therefore, longer time will always favor the completely dissolution of the individual coating species particles and the formation of better coating layers. However, according to the Kelvin equation above, the difficulty for particles growth increases at an exponential relationship with the particle size. Therefore, the relative speed for the individual coating species particles to dissolve will decrease with time. The success of our model in reproducing and explaining experimental phenomena assured its accuracy and practicality in simulating coating in colloidal suspension.

In addition, in theoretical point of view, this model could also help answer some important questions that has not been answered by the experiments and cannot be answered by previous model. For example, how to improve (eliminate) the coating quality (the individual coating species particles) within limited amount of time or under a fixed core/coating species mole ratio or under a desired core and coating species concentration? Our simulation showed that, in general, decreasing the core particle size, increasing the core particle concentration and increasing the coating species solubility are effective methods to prevent the formation of particles of the pure coating species. Increasing the coating species solubility and decreasing the core particle size helped increase the coating thickness and obtain a better coating. Under stoichiometric conditions, i.e., fixed molar ratio of the coating species over the core species, decreasing the core particle size is effective in eliminating the precipitation of individual coating-species particles. Increasing the coating species solubility is effective in both preventing the formation of individual coating-species particles and improving the coating quality.

CHAPTER 4: PYROCHLORE FREE PMN-PT POWDER PROCESSING BY A COATING METHOD

The major objective of this thesis is to find a simplified, lower temperature sintering method for perovskite phase PMN-PT processing. The approach is to coat $Mg(OH)_2$ on the surface of Nb_2O_5 to improve homogeneity and reactivity, therefore the desired perovskite PMN-PT phase could be obtained by one-step calcination. After the colloidal coating phenomena is studied by simulation in previous chapter, experimentally coating $Mg(OH)_2$ on Nb_2O_5 and the one-step calcination processing of PMN-PT powder will be studied in this chapter.

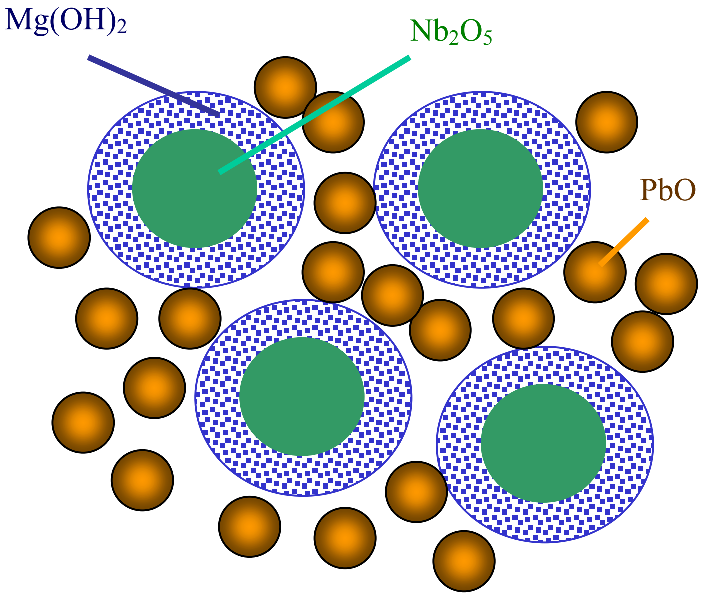

Figure 4.1: Schematic of the $Mg(OH)_2$-coated Nb_2O_5 particles mixed with PbO particles

4.1 Introduction

As explained in Chapter 1, many PMN-PT perovskite phase processing methods have been found so far, including two-step calcination Columbite method[32] and one-step calcination processing methods.[70, 25, 71, 36, 37, 39, 40, 41, 42] In this chapter, a simpler, one-step calcination method to produce single-phase perovskite PMN-PT and PMN powders based on colloidal coating method will be reported. In this method, Nb_2O_5 powder is coated with $Mg(OH)_2$ in the first step. In the second step, the $Mg(OH)_2$-coated Nb_2O_5 powder is mixed with PbO for calcination, as schematically illustrated in Figure 4.1.

4.2 Experimental Procedure

Starting materials used in this study were Nb_2O_5 (99.9%, Aldrich Chemical Co., Milwaukee, WI), $PbTiO_3$ (99.+%, Aldrich), PbO (99.9+%, Aldrich), $Mg(NO_3)_2{\cdot}6H_2O$ (99%, Aldrich), and NH_4OH (5.08N, Aldrich). The 0.9PMN–0.1PT and PMN precursors were prepared in the following sequence. $Mg(NO_3)_2{\cdot}6H_2O$ (0.105 mol) was dissolved in 500 mL of distilled water, followed by the addition of 0.1 mole of dispersed Nb_2O_5 powder suspension in the solution. This mixture, denoted as suspension I, was then stirred and ultrasonicated (50 MHz, 50 W, Model Ultrasonic Homogenizer 4710 series, Cole-Parmer Instrument Co., Vernon Hills, IL) for 10 min to break up the Nb_2O_5 agglomerates. At this point, the suspension pH was between 5 and 6. For $Mg(OH)_2$ to precipitate on the Nb_2O_5 surface, NH_4OH (5.08N) then was added drop wise into the mixture until the pH reached 10 and the mixture was stirred for 30 min. The reason that the coating pH was chosen to be 10 was that the solubility product of $Mg(OH)_2$ is $K_{sp}=1.2\times10^{-11}$.[72] With $K_{sp}=[Mg^{2+}][OH^-]^2$ and $[Mg^{2+}]=0.21M$, we estimated the lowest precipitation pH for $Mg(OH)_2$ was ~8.9. Therefore, at pH 10, the precipitation of $Mg(OH)_2$ was expected. Furthermore, the surface of Nb_2O_5 was negatively charged at pH >6, (see Figure 4.3) and, thus, was attractive to the Mg^{2+} ions. Also the calculated value of the Hamaker constant between Nb_2O_5 and $Mg(OH)_2$ is larger than the Hamaker constant between $Mg(OH)_2$ themselves.[69] The Nb_2O_5 and $Mg(OH)_2$ have opposite surface charge at precipitation pH. All these factors should promote the precipitation of $Mg(OH)_2$ on the Nb_2O_5, making the coating of $Mg(OH)_2$ on Nb_2O_5 possible.

The coated suspension was mixed with a suspension of PbO and $PbTiO_3$ and denoted as suspension II. Suspension II was prepared by mixing 200 mL of distilled water with 0.303 mol of PbO and an appropriate amount of $PbTiO_3$, depending on the composition of the PMN–PT solid solution. Suspension II was ultrasonicated for 10 min before it was added to suspension I. The mixture then was stirred for 60 min and dried by rotary evaporation. The dried powders were ball-milled in isopropyl alcohol for 20 h and rotary evaporated. The ball-milled powders were calcined at 800° or 900°C for 2 h with a heating rate of 5°C/min.

The coating of $Mg(OH)_2$ on Nb_2O_5 particles was examined using optical microscopy and zeta-potential measurements. The optical microscopy sample was prepared by dropping 10 drops (~0.5 mL) of the coated suspension (suspension I) into 200 mL of distilled water for dilution, and the pH of the diluted suspension was maintained at 11 by adding an appropriate amount of NH_4OH to prevent complete dissolution of $Mg(OH)_2$. At this dilution condition, with $K_{sp}=1.2\times10^{-11}$, we estimated that the dissolution of $Mg(OH)_2$ occurred at pH < 10.2. Therefore, the suspension pH had to be adjusted to > 10.2 to prevent $Mg(OH)_2$ from completely dissolving. Two drops of the diluted suspension were placed on an optical slide and dried by evaporation. The dried powders were examined using optical microscopy (Model PMG-3, Olympus Optical Co., Tokyo, Japan). Zeta-potential measurements were performed (Model Zeta-Meter System 3.0+, Zeta-Meter, Inc., Staunton, VA).

To prepare green bodies, the calcined powders were mixed with 3 wt% of an aqueous solution of 5 wt% of poly(vinyl alcohol) (PVA) for granulation. The granulated powders then were pressed at 200 MPa into pellets 1 mm thick and 25 mm in diameter. The pellets were heated in air at 5°C/min to 500°C, held for 4 h to remove the PVA binder, and heated at 5°C/min to 1150°C for 2 h for sintering. During the heat treatment, $PbZrO_3$ (PZ) powders were stacked between the pellets. The entire assembly was fired in a closed alumina crucible with a small amount of PbO added to minimize lead loss. After the pellets were sintered, both sides were polished and electroded with a silver paste.

The phases of the powders were examined using X-ray diffractometry (XRD; Model D500, Siemens, Madison, WI). The step in varying the diffraction angle was 0.01°, with a scan rate of 1 s/step. The sintered density was measured using the Archimedes method in kerosene. The dielectric constant and the loss factor were measured using an impedance analyzer (Model HP 4192a LF, Hewlett-Packard, Palo Alto, CA). Scanning electron microscopy (SEM; Model 1830, Amray, Bedford, MA) was used to examine the fracture surface of the sintered ceramic piece. Particle-size distribution was measured using a laser-scattering particle-size analyzer (Model LA-910, Horiba, Irvine, CA).

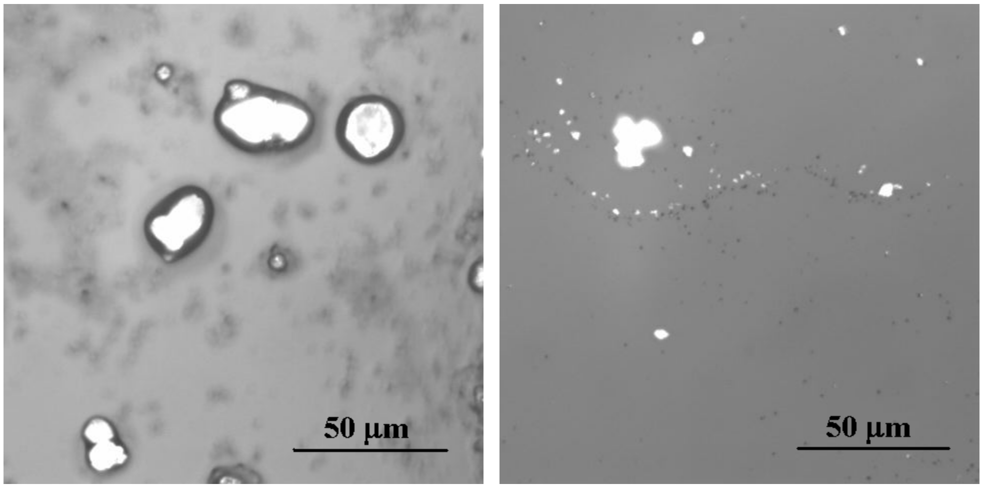

(a) (b)

Figure 4.2: Optical micrograph of (a) $Mg(OH)_2$-coated Nb_2O_5 particles and (b) uncoated Nb_2O_5 particles.

4.3 Results and Discussion

An optical micrograph of the coated Nb_2O_5 particles is shown in Figure 4.2(a) with light-colored particles surrounded by dark-colored coating layers. For comparison, an optical micrograph of uncoated Nb_2O_5 particles is shown in Figure 4.2(b). Figure 4.2(b) shows that uncoated Nb_2O_5 particles appear as light-colored particles in the micrograph. This indicates that the light-colored core particles in Figure 4.2(a) are Nb_2O_5 particles. The dark-colored coating layers surrounding the Nb_2O_5 particles were designated as $Mg(OH)_2$, because the XRD study showed the powder obtained by the same precipitation procedure but without the Nb_2O_5 core particles, i.e., suspension I without Nb_2O_5, were $Mg(OH)_2$. Moreover, the XRD pattern of the coated powder after heat treatment at 500°C showed MgO peaks. Therefore, we expected the coating layer to be $Mg(OH)_2$. The measured coating thickness was consistent with the amount of $Mg(NO_3)_2{\cdot}6H_2O$ added to the system. Moreover, the measurements of zeta-potential of the coated particles showed that the Nb_2O_5 particles were coated with $Mg(OH)_2$. Figure 4.3 shows the zeta-potential versus pH of the coated Nb_2O_5 particles. Also shown in Figure 4.3 are the zeta-potentials of $Mg(OH)_2$ and Nb_2O_5, for comparison. At pH >10, the zeta-potential of the coated particles was similar to that of $Mg(OH)_2$. Furthermore, at pH >10, we observed that all particles in the electrophoretic cell moved in the same direction. This was quite significant, because, at pH >10, the zeta-potential of $Mg(OH)_2$ had a sign opposite to that of Nb_2O_5, as shown in Figure 4.3. The fact that all particles in the coated suspension moved in one direction under an applied electric field and that all particles had a zeta-potential similar to that of $Mg(OH)_2$ indicated that $Mg(OH)_2$ was indeed coated on the surface of Nb_2O_5. At pH <10, the zeta-potential of the coated particles became similar to that of Nb_2O_5. As discussed in the previous section, $Mg(OH)_2$ dissolved at pH <10 on dilution. Thus, at the dilute concentrations that were suitable for zeta-potential measurements, the $Mg(OH)_2$ coating layers dissolved at pH <10. As a result, the Nb_2O_5 surface became exposed, and the zeta-potential of the coated particles became that of Nb_2O_5. The fact that the surface of the coated particles behaved similar to that of $Mg(OH)_2$ at pH >10 and reverted to that of Nb_2O_5 at pH <10 because of the dissolution of $Mg(OH)_2$ further confirmed that the $Mg(OH)_2$ was indeed coated on Nb_2O_5.

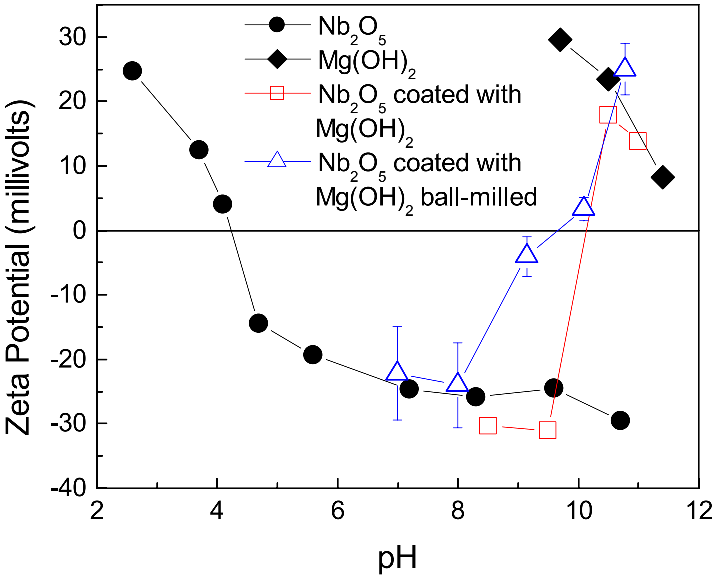

Figure 4.3: Zeta-potential versus pH of the $Mg(OH)_2$-coated Nb_2O_5 particles and zeta-potential versus pH for the $Mg(OH)_2$ particles and the Nb_2O_5 particles.

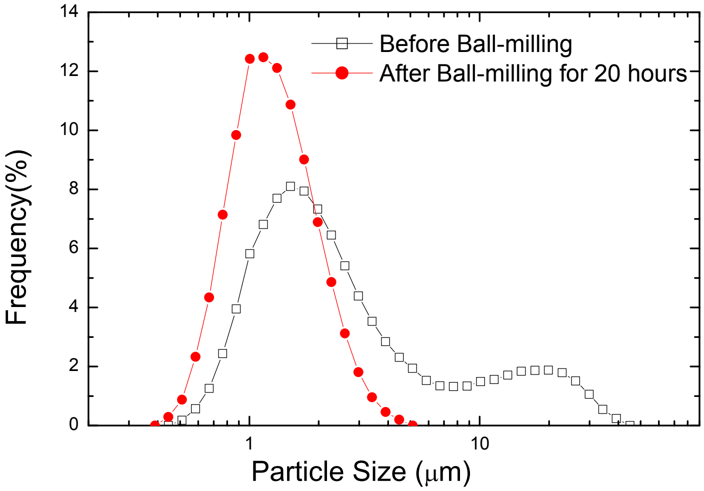

Figure 4.4: Particle-size distribution of $Mg(OH)_2$-coated Nb_2O_5 before and after ball milling for 20 h.

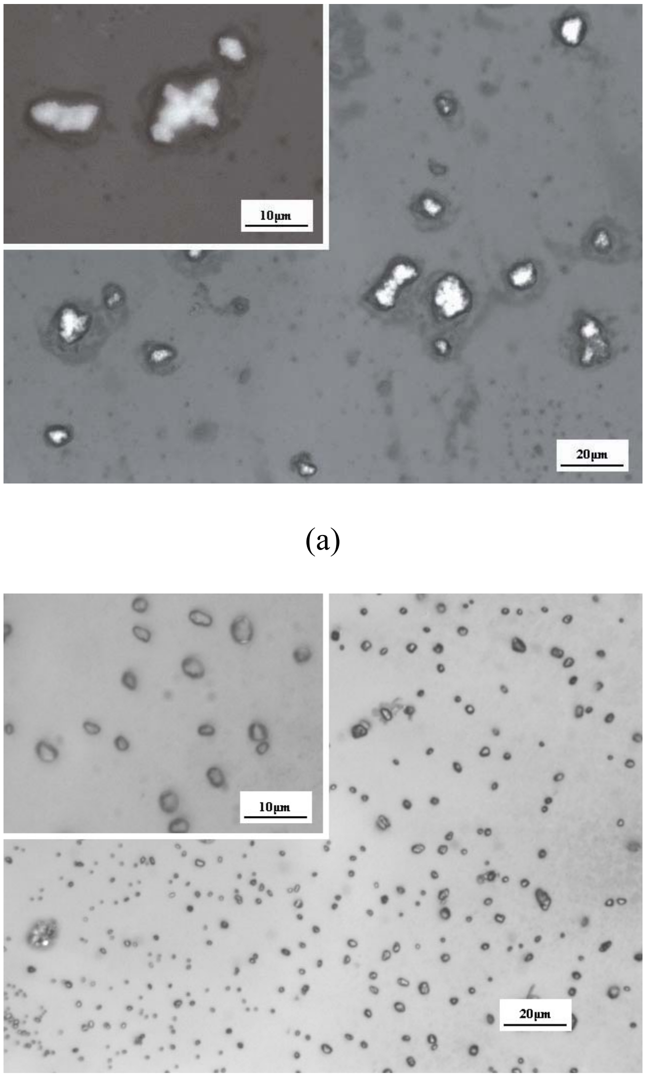

(a)

(b)

Figure 4.5: Optical micrographs of $Mg(OH)_2$-coated Nb_2O_5 particles (a) before and (b) after ball milling for 20 h.

To determine the effect of ball milling on the $Mg(OH)_2$ coating, we measured the particle-size distribution and performed optical microscopy of coated powders before and after milling. Figure 4.4 shows the particle-size distribution of $Mg(OH)_2$-coated Nb_2O_5 particles before and after ball milling. The particle-size distribution shows a bimodal distribution before milling and uniform size distribution after milling. The results indicated that agglomeration of particles occurred, leading to agglomerates, which were then broken up by the milling process. Figure 4.5 shows an optical micrograph of $Mg(OH)_2$-coated Nb_2O_5 particles before (Figure 4.5(a)) and after (Figure 4.5(b)) ball milling. Figure 4.5 shows that, before milling, particles were agglomerated and that the agglomerates were coated. After they were milled, the particles become smaller and isolated but remained coated. The dark-colored ring of $Mg(OH)_2$ continued to exist on the light-colored Nb_2O_5 particle surfaces. The conclusion of $Mg(OH)_2$ remaining as coating on the surface of Nb_2O_5 after ball milling was also proven by the zeta-potential data in Figure 4.3. It was speculated that, during the coating process, the $Mg(OH)_2$ coated the agglomerates of Nb_2O_5 particles. During ball milling in isopropyl alcohol, the agglomerates were broken, and the stripped coating materials may have precipitated on the individual Nb_2O_5 particles through a dissolution and reprecipitation process.

The dried powders were calcined at 800° or 900°C for 2 h for X-ray study. The percentage of the perovskite phase was estimated using the formula

$$X_{pero}(\%) = \left(\frac{I_{(110)perovskite}}{I_{(110)perovskite} + I_{(222)pyrochlore}}\right) \times 100\% \qquad (4.1)$$

where $I_{(110)perovskite}$ and $I_{(222)pyrochlore}$ are the intensity of the (110) peak of the perovskite phase and that of the (222) peak of the pyrochlore phase, respectively. Figures 4.6(a) and (b), respectively, show the diffraction patterns of the coated powder mixed with PbO (with the stoichiometry of PMN) and that of the coated powder mixed with PbO and 10% $PbTiO_3$ (with the stoichiometry of 0.9PMN–0.1PT) in the range $2\theta = 29°$ to $2\theta = 34°$. The coated powder mixed with PbO and the coated powder mixed with PbO and 10%

$PbTiO_3$ became 100% perovskite after calcination at 900°C for 2 h. There is a slight shoulder on the (110) peak in Figure 4.6(a). It was unclear what phase this represented, because no relevant additional peaks were found. The diffraction pattern of the coated powder mixed with PbO and 10% $PbTiO_3$ calcined at 800°C for 2 h is shown in Figure 4.6(b), which indicates that the powder is not 100% perovskite. Some amount (25 wt%) of pyrochlore phase was present in the powder after it was calcined at 800°C for 2 h. The results in Figures 4.6(a) and (b) indicate that complete conversion to the perovskite phase (or complete elimination of the pyrochlore phase) occurred between 800° and 900°C.

Several 0.9PMN–0.1PT sintered pieces (22 mm in diameter and ~0.5 mm in thickness) were prepared, and their dielectric properties were measured. Figure 4.7 shows the dielectric constant and loss factor versus temperature of a 0.9PMN–0.1PT sample at 0.1, 1, 10, and 100 kHz. As the frequency increased, the dielectric maximum shifted to a higher temperature, and the dielectric constant became smaller, which was consistent with typical relaxor behavior. When measured at 1 kHz, the maximum relative dielectric constant was 24,660, similar to values reported by other researchers. The density of the sintered ceramics was 7.9 g/cm^3, ~97.0% of the theoretical density of 8.1 g/cm^3.[40] Figure 4.8 is a SEM micrograph of the fracture surface of a 0.9PMN–0.1PT specimen. Figure 4.8 shows that the average grain size was ~5μm and that the distribution of the grain size was quite uniform. These results indicated that the coating method could produce pyrochlore-free PMN and 0.9PMN–0.1PT powders that could be sintered at 1150°C and that the sintered ceramics exhibited very high dielectric constants.

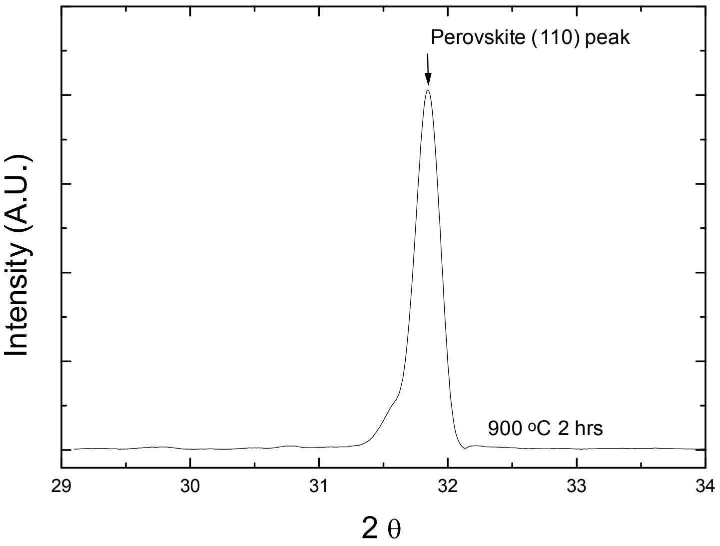

(a)

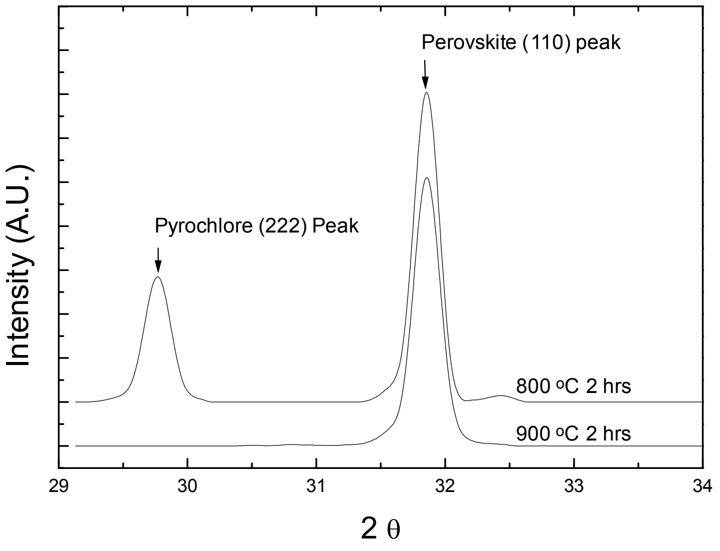

(b)

Figure 4.6: XRD patterns of (a) powder containing $Mg(OH)_2$-coated Nb_2O_5 and PbO (with the stoichiometry of PMN) calcined at 900°C for 2 h and (b) powder containing $Mg(OH)_2$-coated Nb_2O_5, PbO and 10% $PbTiO_3$ (with the stoichiometry of 0.9PMN-0.1PT) calcined at 900°C and 800°C for 2 h.

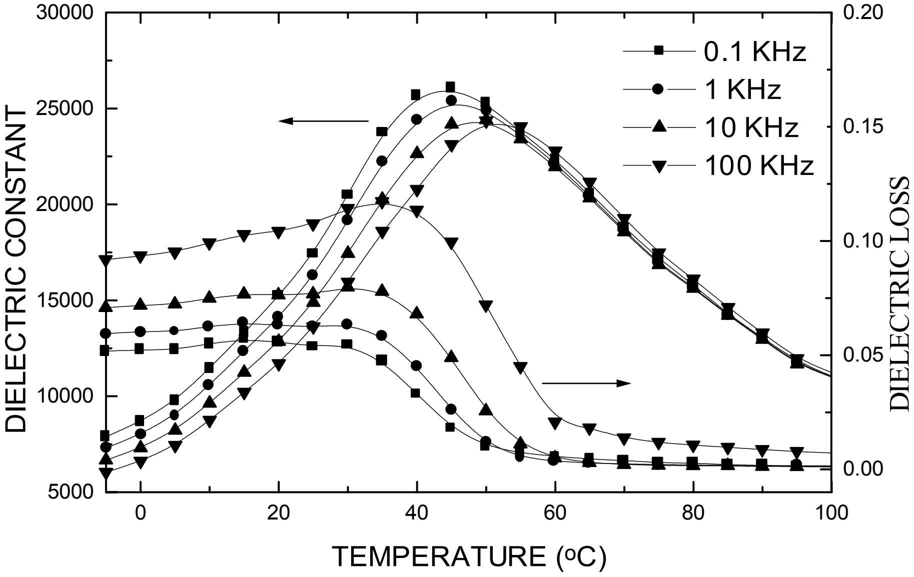

Figure 4.7: Dielectric constant and loss factor as a function of temperature of a 0.9PMN-0.1PT sample at various frequencies.

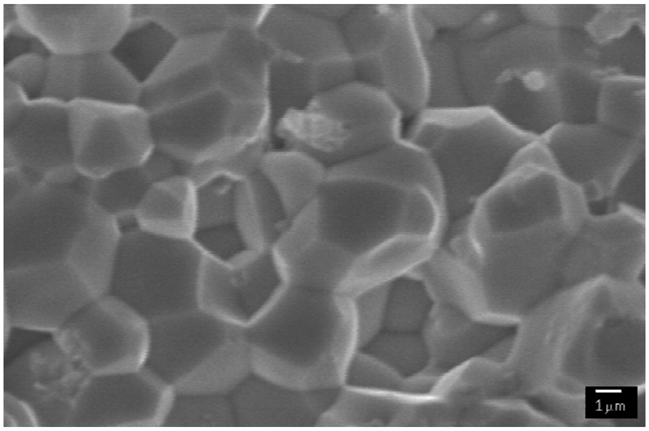

Figure 4.8: SEM fracture surface micrograph of a 0.9PMN-0.1PT specimen sintered at 1150°C for 2 h.

4.4 Summary

This chapter showed that the coating of $Mg(OH)_2$ on the surface of Nb_2O_5 could be obtained by precipitating $Mg(OH)_2$ in an aqueous Nb_2O_5 suspension at pH 10. Optical micrographs and zeta-potential measurements confirmed that the Nb_2O_5 surface was coated with $Mg(OH)_2$. Ball-milling after coating could break the agglomeration. Since the colloidal coating is a dynamic process, after ball-milling, $Mg(OH)_2$ still coated on the surface of Nb_2O_5. Pyrochlore free perovskite PMN or 0.9PMN-0.1PT could be produced after calcine the ball-milled coated powder to 900°C for 2 hours. 0.9PMN-0.1PT ceramics with good density and dielectric properties could be produced by sintering the pyrochlore free perovskite powders at 1150°C. Only a single step of calcination and a single step of ball-milling are needed to produce pyrochlore free PMN or PMN-PT powder. Also this method needs only regular micron size raw materials and regular equipment.

CHAPTER 5: STUDY OF MECHANISM OF PYROCHLORE FREE PMN-PT POWDER PROCESSING USING A COATING METHOD

Previous chapter showed that $Mg(OH)_2$ can be coated on Nb_2O_5 and pyrochlore free PMN or 0.9PMN-0.1PT powder could be obtained with only one-step calcination through this coated powder. The reasons why the coating method could prevent the formation of pyrochlore phase will be studied in this chapter. Since there were already many published results about the reaction mechanism and kinetics of PMN synthesis, our study will focus on the unique part of the coating method.

5.1 Introduction

In the past two decades, many efforts had been devoted to understand the reaction mechanism and kinetics for PMN-PT synthesis. Inada[18] first proposed the following the reaction sequence for the calcination of PbO, MgO, and Nb_2O_5 mixture:

$$3PbO + 2Nb_2O_5 \xrightarrow{500-600^\circ C} Pb_3Nb_4O_{13} \text{ (cubic pyrochlore)} \tag{5.1}$$

$$Pb_3Nb_4O_{13} + PbO \xrightarrow{600-700^\circ C} 2Pb_2Nb_2O_7 \text{ (rhombohedral pyrochlore)} \tag{5.2}$$

$$\begin{aligned} &Pb_2Nb_2O_7 + 1/3MgO \xrightarrow{700-800^\circ C} \\ &\qquad Pb(Mg_{1/3}Nb_{2/3})O_3 \text{ (perovskite)} + 1/3Pb_3Nb_4O_{13} \end{aligned} \tag{5.3}$$

In his study, two mid-phases, cubic pyrochlore $Pb_3Nb_4O_{13}$ and rhombohedral pyrochlore $Pb_2Nb_2O_7$, were produced. Bouquin et al[19] proposed a different reaction sequence later:

$$3\mathrm{PbO} + 2\mathrm{Nb_2O_5} \xrightarrow{500-600^{\circ}\mathrm{C}} \mathrm{Pb_3Nb_4O_{13}}\ \text{(Cubic Pyrochlore)} \tag{5.4}$$

$$\mathrm{Pb_3Nb_4O_{13}} + 2\mathrm{PbO} \xrightarrow{630-690^{\circ}\mathrm{C}} \mathrm{Pb_5Nb_4O_{15}}\ \text{(Rhombohedral Pyrochlore)} \tag{5.5}$$

$$\mathrm{Pb_5Nb_4O_{15}} + \mathrm{PbO} \xrightarrow{700-730^{\circ}\mathrm{C}} 2\mathrm{Pb_3Nb_2O_8}\ \text{(Tetragonal Pyrochlore)} \tag{5.6}$$

$$\mathrm{Pb_3Nb_2O_8} + \mathrm{MgO} \xrightarrow{750-800^{\circ}\mathrm{C}} 3\mathrm{Pb(Mg_{1/3}Nb_{2/3})O_3}\ \text{(Perovskite)} \tag{5.7}$$

Most other studies showed that only one pyrochlore phase was formed during the reaction with the following possible formulas: $Pb_{1.83}Nb_{1.71}Mg_{0.29}O_{6.39}$,[20] $Pb_2Mg_{0.32}Nb_{1.87}O_7$,[21] $Pb_{1.86}Nb_{1.76}Mg_{0.24}O_6$,[22] $Pb_{2.25}Nb_{1.79}Mg_{0.27}O_7$,[23] $Pb_2Nb_{1.75}Mg_{0.25}O_{6.62}$,[24] $Pb_2Nb_{1.33}Mg_xO_{5.33+x}(0<x<0.66)$,[25] $Pb_3(Mg_{1-x}Nb_{2+x})O_{9+3x/2}(0<x<0.625)$,[26] $Pb_{(3+3x/2)/2}(Mg_xNb_{2-x})O_{0.65}(0<x<0.5)$,[27] $Pb_{1.83}Mg_{0.29+x}Nb_{1.71-x}O_{6.39-1.5x}(0.1<x<0.522)$,[28] $Pb_{2-x}(Mg_{0.286}Nb_{1.714})O_{6.571-x}(0<x<0.286)$.[29] The common features of these studies are that the pyrochlore phase is composed mainly of PbO and Nb_2O_5. Small amount of MgO may appear in the pyrochlore lattice. The ratio of Pb:Nb in these pyrochlore phases are less than the ratio of Pb:Nb=1.5 in the perovskite phase. In essence, the transformation reaction from the pyrochlore phase to the perovskite phase is mainly a process of MgO diffusing into the lattice of pyrochlore.

There were also several kinetic studies on the influence of processing on the percentage of perovskite phase formed. Lejeune and Boilot[37] found that improving the reactivity and dispersibility of MgO by using $MgCO_3$ as a reactant and acetone as ball-milling media could increase the percentage of perovskite phase formed. Calcination in O_2 atmosphere also improves the percentage of perovskite phase. Multiple calcination cycles can improve the perovskite percentage but high temperature calcination for long time will decrease the perovskite phase because of PbO loss by evaporation. Desgardin et al[31] found that the uniform distribution of MgO was critical to the perovskite phase formation.

In this study, we will continue to study the reaction mechanism of perovskite phase formation. Our study will focus on why our coating method can prevent the formation of pyrochlore phase by using only micron-size Nb_2O_5 and PbO. We hope this study could add to our understanding of the one-calcination processing of perovskite PMN powder.

5.2 Experimental Procedure

The procedure of coated powder preparation was the same with the one described in the experimental procedure part of Chapter 4. Same as Chapter 4, the composition we used here is 5 at.% excess of MgO together with 1 at.% excess of PbO.

To study the reactions, differential thermal analysis (DTA, Model Universal V2.3C, TA Instruments, Inc., Newcastle, DE) and emission analysis were performed on the coated powder. The Quantachrome NOVA 2200 was used to measure the specific surface area of powders. Scanning electron microscopy (SEM, Model 1830, Amray, Bedford, MA) was used to examine the fracture surface of pressed samples. X-ray diffractometry (XRD, Model D500, Siemens, Madison, WI) was used to identify the phase.

As will be discussed in the Results and Discussions part of this chapter, nanosize MgO (92 nm) and Nb_2O_5 (35 nm) powder were also used. They were prepared by wet-chemical method. For nanosize MgO preparation, 0.105 mol $Mg(NO_3)_2 \cdot 6H_2O$ (99%, Aldrich) was first dissolved in 500 ml distilled water. While keeping the solution stirring, ammonium hydroxide (5.08N, Aldrich) was added dropwise until pH of the solution reached 10 resulting in the precipitation of $Mg(OH)_2$. The suspension was rotary evaporated and heat-treated at 500°C for 1 hour. The product was MgO powder of 92 nm in diameter. To prepare nanosize Nb_2O_5, 0.1 mole niobium oxalate (99%, Aldrich) was dissolved in 500 ml of distilled water. 30ml ammonium hydroxide (5.08N, Aldrich) was added dropwise while keeping the solution stirring. Precipitates were collected by centrifugation and followed by 80°C evaporation. Finally, it was heat-treated at 500°C for 3 hours. The product was Nb_2O_5 with 35 nm in diameter.

Besides the experiments above, some other experimental detail will also be explained when needed in results and discussions part.

5.3 Results and Discussion

Figure 5.1 shows the results of differential thermal analysis (DTA) and emission analysis of $Mg(OH)_2$-coated Nb_2O_5 powders with PbO powders. The DTA result (Figure 5.1(a)) showed that there were reactions at <200°C, 330°C, 434°C, 483°C, 569°C, and 807°C during calcination. Emission analysis results (Figure 5.1(b)) showed that three different kinds of gas with molecular weight 18, 30, and 46 were evaporated during calcination. Since only elements of Nb, Mg, Pb, Ti, O, N, and H existed in the system, the only possible gas emissions were H_2O or NH_3 for molecular weight 18, NO for 30, and NO_2 for 46.

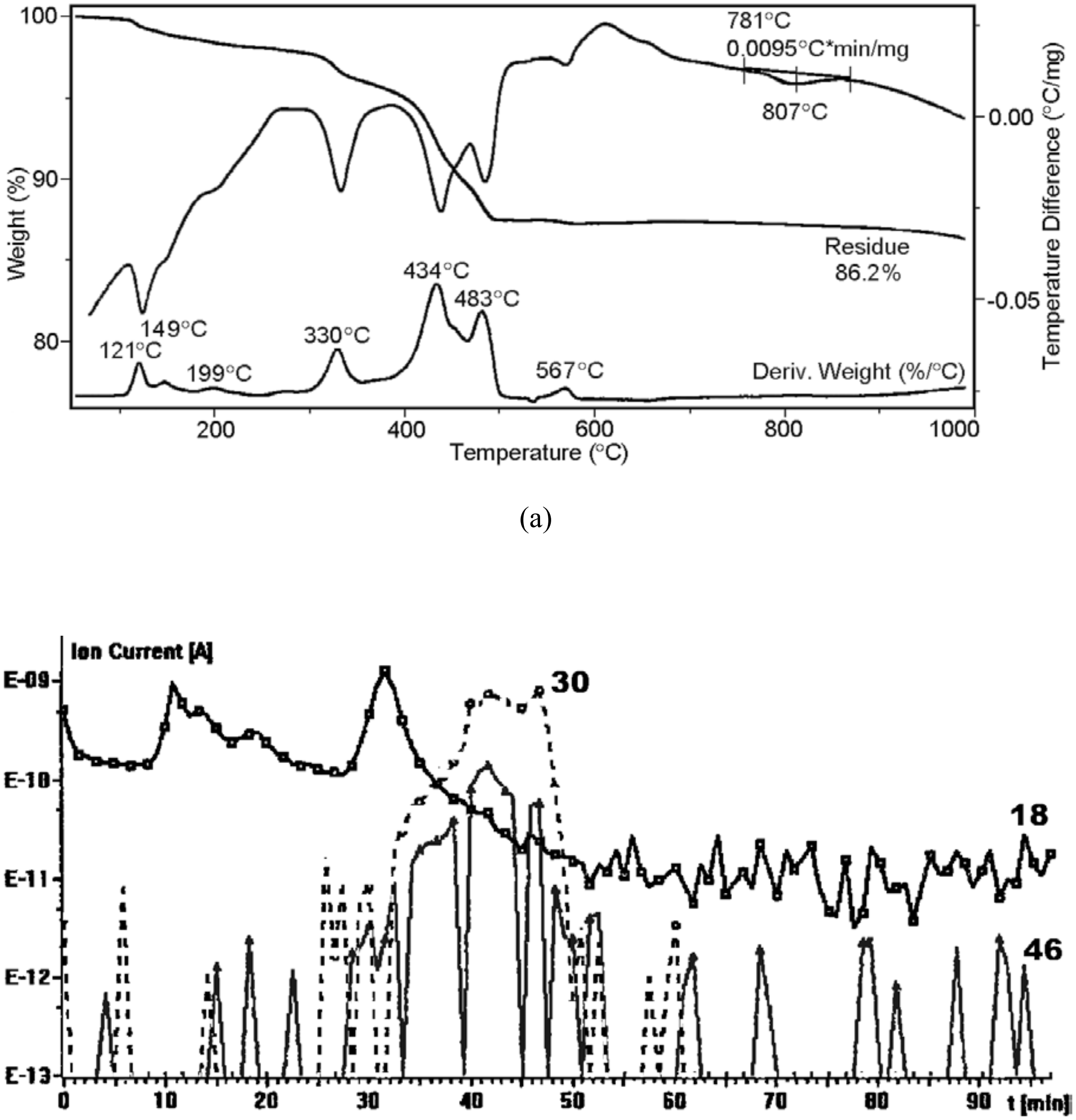

(a)

(b)

Figure 5.1: (a) DTA analysis and (b) emission analysis of the coated powder. The numbers in the emission analysis result represent the molecular weights of the emitted gas.

To analyze the reactions found in the DTA results, x-ray diffraction was performed on coated powders calcined at different temperatures. These samples were prepared by first heat-treating the as-synthesized coated powder to the desired temperature at the rate of 5°C/min. After holding at the temperature for 1 hour, the powders were cooled to room temperature at the rate of 10°C/min. Figure 5.2 shows the results of the x-ray diffraction. It can be seen that the as-synthesized powder was a mixture of Nb_2O_5 and $3Pb(NO_3)_2 \cdot 7PbO$ at room temperature. The PbO initially added has become $3Pb(NO_3)_2 \cdot 7PbO$ after coating, evaporation, and ball-milling. Since the reactant used to precipitate $Mg(OH)_2$ was $Mg(NO_3)_2$, it is possible for the $(NO_3)^-$ ions from the $Mg(NO_3)_2$ to react with PbO and forming $3Pb(NO_3)_2 \cdot 7PbO$ in the solution or during evaporation. However the detailed reaction mechanism is not clear yet. Reaction peaks below 200°C were observed in Figure 5.1(a). Considering there was a large amount of H_2O or NH_3 evaporating revealed in Figure 5.1(b) in this temperature range, we attributed these reaction peaks to the evaporation of bound water and NH_3. In Figure 5.2(a), no peaks of Mg-compound were found in the diffraction pattern below 300°C and there was only a barely noticeable MgO peak in the diffraction pattern at 350°C. This is consistent with the fact that MgO only occupy 4.2 wt% in $Pb(Mg_{1/3}Nb_{2/3})O_3$ and Mg-compound is likely in the amorphous state.

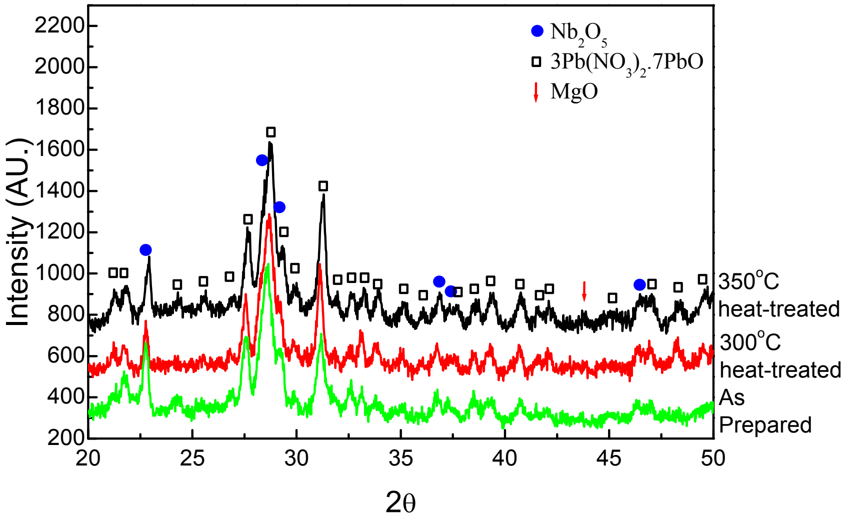

(a)

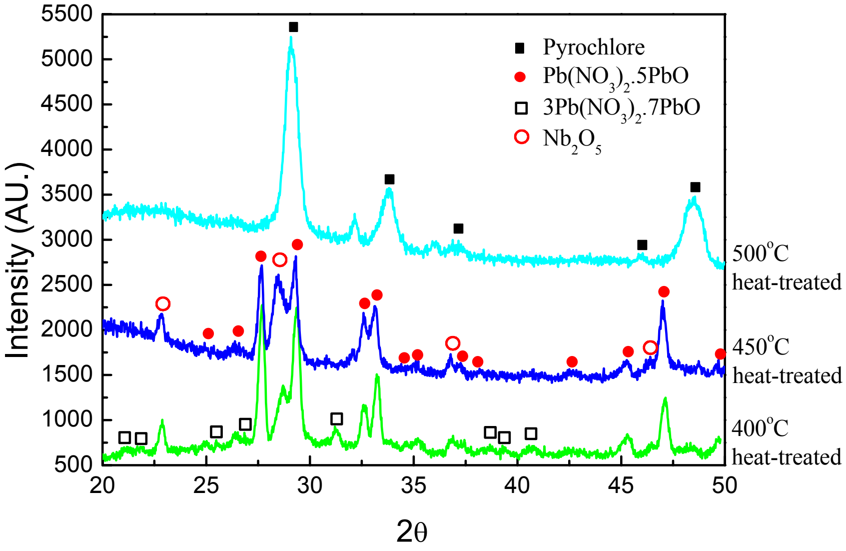

(b)

Figure 5.2: X-ray diffraction patterns for coated powder heat-treated at different temperatures for 1 hour.

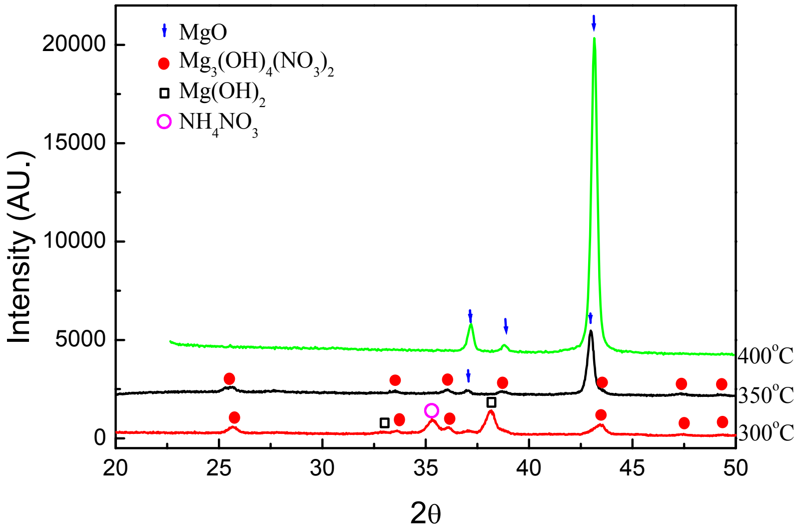

Figure 5.3: X-ray diffraction pattern of Mg-compound precipitation after 300°C, 350°C, 400°C heat-treatment for 1 hour.

In order to investigate the phase changes of the Mg-compound during calcination, a solution of $Mg(NO_3)_2$ with the same concentration as that used in the coating method were prepared. Similar to the coating method, ammonium hydroxide was added to precipitate $Mg(OH)_2$. Unlike the coating method, no Nb_2O_5 powder was added to coat $Mg(OH)_2$ on and no PbO were added after precipitation. In this way, the pure Mg-compound coating substance was prepared. The Mg-compound was heat-treated to several temperatures and the x-ray diffractions were performed. Figure 5.3 shows the x-ray diffraction pattern of the Mg-compound calcined to 300°C, 350°C, and 400°C. The pattern showed that, at 300°C, Mg-compound was composed mainly of $Mg(OH)_2$ with a small amount of $Mg_3(OH)_4(NO_3)_2$. At 350°C, the diffraction pattern showed $Mg(OH)_2$

disappeared and MgO was the dominant phase. This means that coating precipitation mainly consisted of $Mg(OH)_2$. The $Mg(OH)_2$ coating will decompose to MgO between 300°C and 350°C. This temperature range matched well with the $Mg(OH)_2$ decomposition temperature of 330°C from physical chemistry handbook. So we conclude that the reaction at 330°C detected by DTA (Figure 5.1 (a)) is the transformation reaction from $Mg(OH)_2$ to MgO with the following equation:

$$\mathrm{Mg(OH)_2} \xrightarrow{330°\mathrm{C}} \mathrm{MgO} + \mathrm{H_2O} \tag{5.8}$$

The emission peak of gas with molecular weight 18 at this temperature range in Figure 5.2 (b) confirms this reaction. A small amount of $Mg_3(OH)_4(NO_3)_2$ did not decompose until 400°C as shown by Figure 5.3. To investigate the particle size of MgO from the $Mg(OH)_2$ decomposition, specific surface area of MgO from $Mg(OH)_2$ precipitation calcined at 400°C and 500°C respectively were measured. The results were listed in Table 5.1. The particle size in the table was calculated from the specific surface area using equation $D = 6/\rho(SSA)$ where ρ is the theoretical density, SSA is the specific surface area, and D is the calculated particle size. The results of calculated particle size suggest that the MgO made from $Mg(OH)_2$ decomposition was about 100 nm in size. This size is much smaller than the commercial MgO, which is in the range of micrometer.

Table 5.1: Specific surface area and particle size of MgO from $Mg(OH)_2$ decomposition at 400°C and 500°C for 1 hour

	Specific Surface Area	**Particle size**
400°C heat-treated	9.3 m^2/g	180 nm
500°C heat-treated	18.3 m^2/g	92 nm

Figure 5.2 (b) was the x-ray diffraction pattern of coated powders calcined at temperatures 400°C, 450°C and 500°C. It showed that the powder was $3Pb(NO_3)_2 \cdot 7PbO$ plus Nb_2O_5 at 400°C, $Pb(NO_3)_2 \cdot 5PbO$ plus Nb_2O_5 at 450°C, and pyrochlore at 500°C respectively. In the same temperature range, peaks of NO and NO_2 were observed from the emission analysis (Figure 5.1(b)). As a result, the following equations are attributed to the 434°C and 482°C reactions found in DTA (Figure 5.1(a)).

$$3(3Pb(NO_3)_2 \cdot 7PbO) \xrightarrow{434^\circ C} 5(Pb(NO_3)_2 \cdot 5PbO) + 8xNO + 8(1-x)NO_2 + 2(2x+1)O_2 \quad (5.9)$$

$$\begin{aligned} &Pb(NO_3)_2 \cdot 5PbO + 6aNb_2O_5 + 6bMgO \xrightarrow{482^\circ C} \\ &\quad 6PbNb_{2a}Mg_bO_{1+5a+b}(\text{pyrochlore}) + 2xNO + 2(1-x)NO_2 + (x+1/2)O_2 \end{aligned} \quad (5.10)$$

where $0 \le x \le 1$, $1/3 \le a \le 1$, $0 \le b < 1/3$. The range of a and b were given to indicate all possible pyrochlore formulas discussed in the Introduction.

The specific surface area of coated-powder calcined at 500°C was measured to be 6.39 m^2/g, corresponding to a diameter of 132 nm. The corresponding surface area and particle size for powders obtained from regular oxide powder mixing calcined at the same temperature was 1.30 m^2/g and 649 nm.

The reactions above 500°C are related to the transformation from pyrochlore to perovskite phase. Several papers have studied these reactions[18, 19, 29] and we will not discuss them here. The general conclusions of these studies were that pyrochlore was an MgO-deficient phase. The transformation is a process of MgO diffusing into the pyrochlore lattice.

So far we have shown that the pyrochlore phase formed after calcination at 500°C for both coated powder and regular oxide mixed powder. The differences between the pyrochlore phase from these two methods are: The particle size of pyrochlore phase particle from the coating method was smaller than that from the oxide mixing method. The MgO in the coating method came from the decomposition of $Mg(OH)_2$. The particle size of MgO formed from decomposition is smaller. Initially the $Mg(OH)_2$ was coated on Nb_2O_5 so the configuration of MgO after 500°C calcination was different from that of oxide mixing.

In order to show the influence of particle size and particle configuration to the pyrochlore-perovskite phase transformation, three types of powder samples were prepared. The first type of sample was a regular MgO, Nb_2O_5, and PbO powder mixture ball-milled for 2 hrs. The average particle size was 320 nm. The second type of sample was a regular MgO, Nb_2O_5, and PbO powder mixture ball-milled for 48 hrs. The average particle size was 240 nm. The third type of sample was a nanosize MgO (92 nm), nanosize Nb_2O_5 (35 nm), and regular PbO powder mixture ball-milled for 48 hrs. The average particle size was 99 nm. Two groups of samples were made from each of the three types of powder. One group was made by heat-treating the powders at 900°C for 2 hrs and another group was pieces made by heat-treating 100 MPa compacted powders at 900°C for 2 hrs. The difference between these three types of powders was the particle size. The difference between the two groups of samples for each type was particle configuration. Here the particle configuration meant the geometric relationship between the components. For example, the pressed powders have higher particle coordination numbers than the loose powders; the coated powders have one substance sit around another. Figure 5.4 shows the percentage of pyrochlore phase formed in each sample.

This result showed that smaller particle size and close compact help the transformation from pyrochlore phase to perovskite phase. This meant that particle size and configuration have a significant effect on the transformation from pyrochlore phase to perovskite phase. This figure also showed that the small particle size itself was not sufficient to prevent the formation of pyrochlore phase.

As illustrated in the Introduction, composition distribution, especially the MgO distribution, is a key factor that influences the transformation from the pyrochlore phase to the perovskite phase. The more uniform the distribution of MgO, the more complete the transformation from the pyrochlore to the perovskite phase. Both particle size and configuration have an effect in influencing the composition distribution, which is a critical factor in completing the reaction. In order to compare these effects quantitatively, a simple simulation of randomly placing mixed oxide and coated powders that are either loose or pressed was performed.

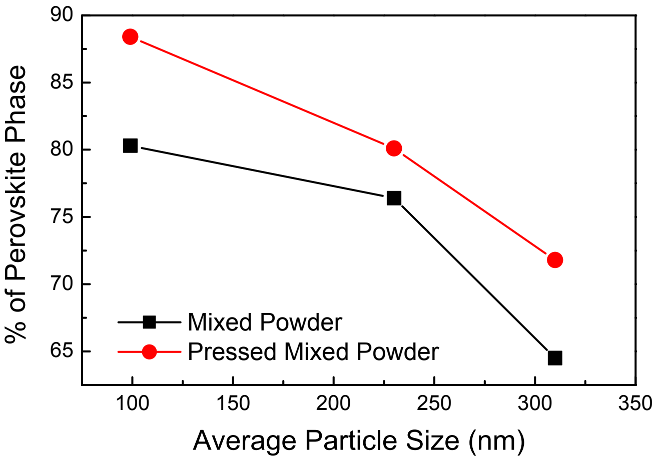

Figure 5.4: Percentage of perovskite phase for oxide mixed powder with different particles size and configuration level calcined at 900°C for 2 hours.

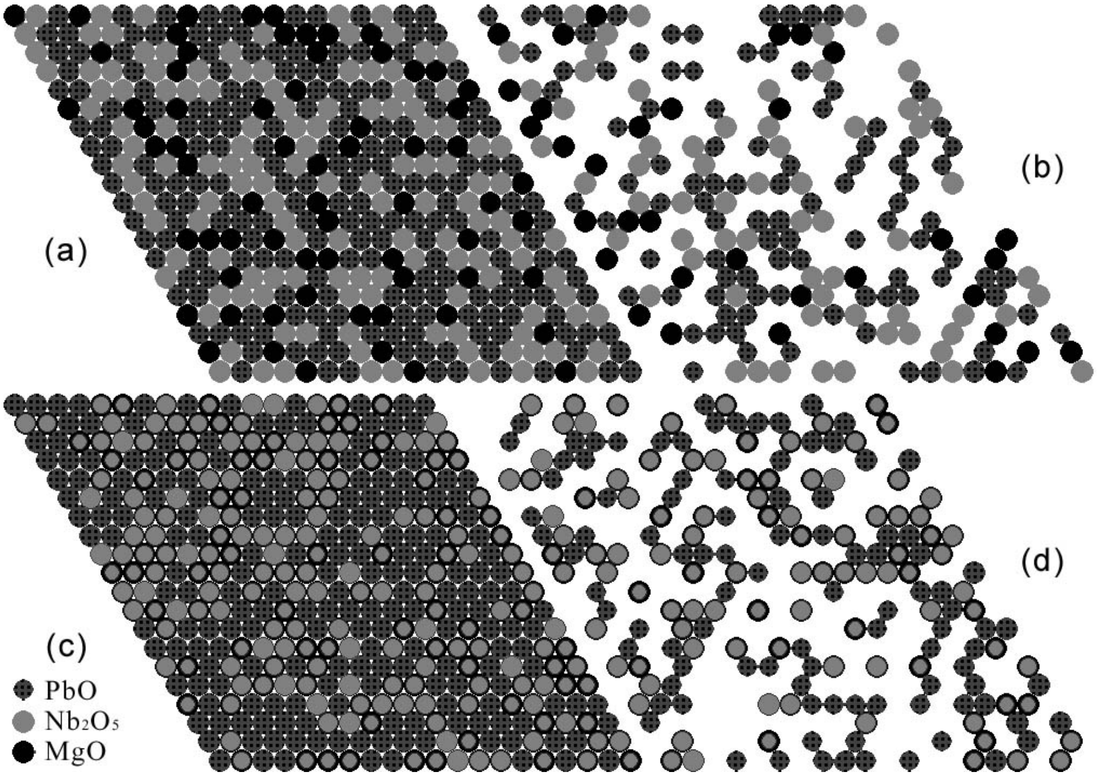

Figure 5.5: Simulation snapshots for (a) pressed oxide powder (b) loose oxide powder with 25% of the lattice occupied (c) pressed coated powder (d) loose coated powder with 25% of the lattice occupied. Mole ratio of $PbO:Nb_2O_5:MgO=3:1:1$ for all the four situations.

The simulation was done on a two-dimensional 200×200 hexagonal close packed lattice. Each lattice point could be occupied by one particle as illustrated in Figure 5.5. For the case of mixed oxide powders, three different particles representing PbO, Nb_2O_5, MgO respectively with the mole ratio 3:1:1 were placed on the lattice randomly. For the case of coated powders, particles with coating were used to represent MgO and Nb_2O_5. The coating thickness was distributed randomly from 50% to 150% of average thickness to represent the non-uniformity of thickness in the coating. The coated particles and the

PbO particles were randomly placed on the lattices. To represent the loose powder condition, only 25% of the lattice sites were occupied with particles. On the other hand, all lattices were occupied to represent the compacted powders. Figure 5.5 shows the snapshots of the simulation. In the snapshot, one lattice point was randomly picked. Based on this lattice point, a hexagon was drawn around it. The compositions of components in this hexagon were calculated and compared with the overall composition of PbO, MgO, and Nb_2O_5. We define the shortest edge of this hexagon in which all the composition were within a 5 % variation of the overall composition as the compositional uniform radius. Here we used a hexagon instead of a circle was for the ease of programming. As will be shown in later part of this chapter, hexagon was good enough to illustrate the concept. In essence, the solid-state reaction was a process of inter-diffusion between components with each other to form a compositionally uniform phase. Under certain temperature and reaction time, the shorter the diffusion distance, the more complete the reaction. This compositional uniform radius we defined was the minimum range for compositional uniformity. Each component would have to diffuse at least in the order of this distance to complete the reaction. So this compositional uniform radius is a parameter related to the diffusion distance. The larger the compositional uniform radius, the longer the components need to diffuse for reaction.

Figure 5.6 shows the simulation results for the compositional uniformity radius with error bars. The number was obtained from the average of 200 independent runs. The unit of radius was the average particles size initially added. The larger the initial average particle size, the longer the diffusion distance, and the more difficult for the reaction to run to completion. This could explain the higher perovskite yield percentage in Figure 5.4

for smaller particle size. Figure 5.6 also showed that the compacted piece has a shorter diffusion distance than the loose powder. This could explain the higher perovskite yield percentage in Figure 5.4 for pressed pieces. Figure 5.6 also showed that the coated powders have a shorter diffusion distance than the mixed oxide powders.

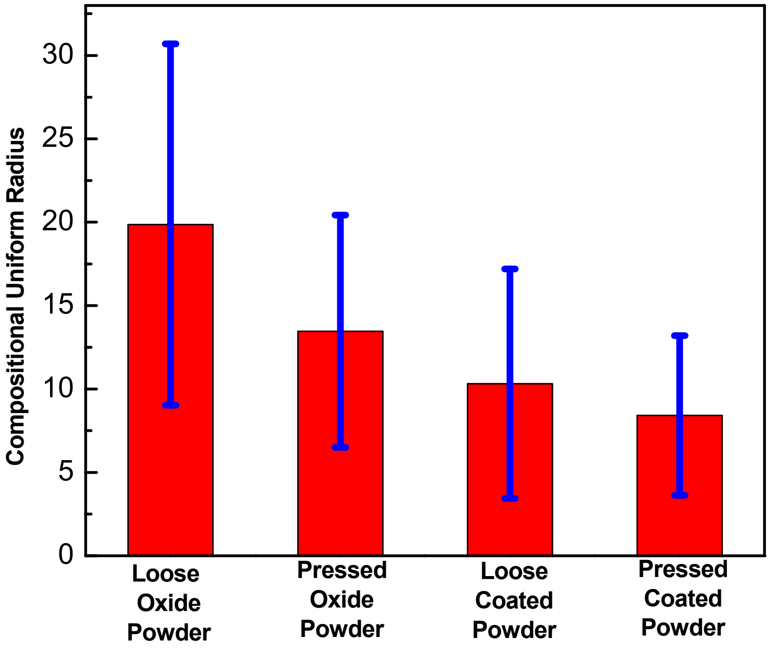

Figure 5.6: Simulation results for the simulation snapshots in Figure 5.5. The bar is the result of 200 independent run. The line on the bar is the standard deviation.

In order to show the beneficial effects of coating to the solid-state reaction, we heated the $Mg(OH)_2$-coated Nb_2O_5 powder at 800°C and 900°C for 2 hours respectively. Mixture of $Mg(OH)_2$ and Nb_2O_5 was also heated at 900°C for 2 hours for comparison. Figure 5.7 shows the XRD patterns after the heat treatment. It shows that, after calcination at 900°C for 2 hrs, the $Mg(OH)_2$-coated Nb_2O_5 powder was completely converted to the columbite phase, $MgNb_2O_6$, whereas mixtures of $Mg(OH)_2$ and Nb_2O_5 powders contained non-columbite phases, which indicated that a coating of $Mg(OH)_2$ on Nb_2O_5 promoted the conversion to the columbite phase.

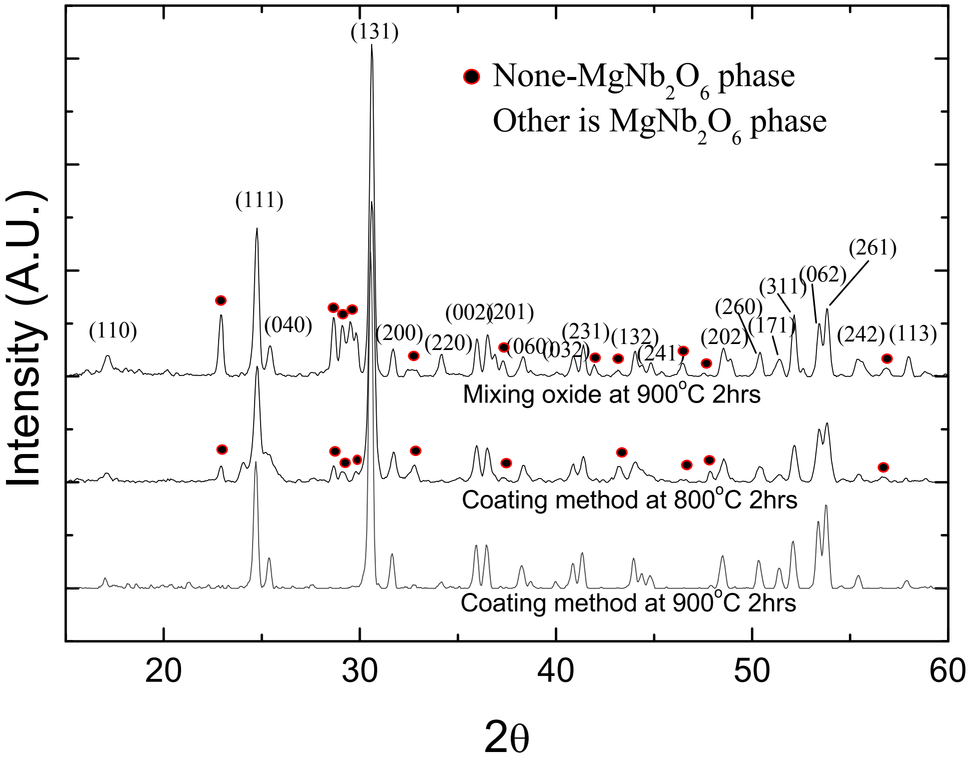

Figure 5.7: XRD pattern of a mixture of $Mg(OH)_2$ and Nb_2O_5 calcined at 900°C for 2 hrs (top curve) and that of the $Mg(OH)_2$-coated Nb_2O_5 powder calcined at 800°C for 2 hrs (middle curve) and at 900°C for 2 hrs (bottom curve). At 900°C for 2 hrs, the $Mg(OH)_2$-coated Nb_2O_5 powder was completely converted to columbite phase. Miller indexes of major peaks of columbite phase are shown.

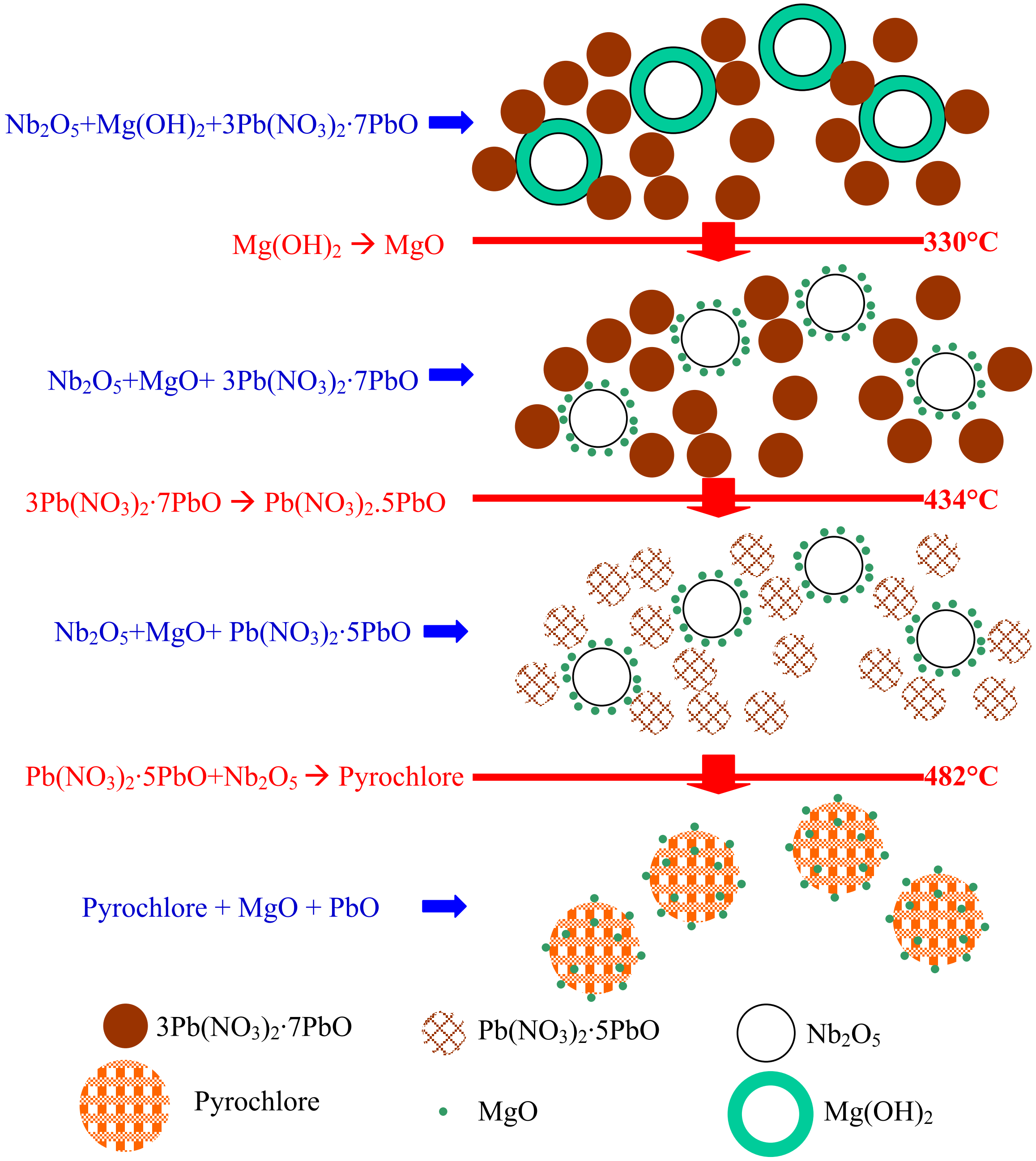

Figure 5.8: Summary of pyrochlore free PMN formation mechanism for the coating method

In summary, Figure 5.8 is an illustration of the phase and microstructure evolution for the calcination of the coated powder. At room temperature, $Mg(OH)_2$ is coated on Nb_2O_5 and PbO is in the form of $3Pb(NO_3)_2 \cdot 7PbO$. At 330°C, $Mg(OH)_2$ decomposes to MgO. The MgO produced still sit around the Nb_2O_5 since there is no related particle movement during the decomposition. At 434°C, $3Pb(NO_3)_2 \cdot 7PbO$ decomposes to $Pb(NO_3)_2 \cdot 5PbO$. At 482°C, $Pb(NO_3)_2 \cdot 5PbO$ reacts with Nb_2O_5 and with maybe a small amount of MgO into pyrochlore phase. The powder after this stage is a mixture of pyrochlore, MgO, and possibly some PbO with average size in the order of 132 nm. As illustrated by simulation, due to this smaller particle size and its coating nature, the distribution of composition was more uniform than simply mixing the components together. This uniform configuration is the reason that enables the complete transformation from pyrochlore to perovskite phase in later stage of calcination. Another reason that may improve the transformation reaction was the close contact between Nb_2O_5 and MgO in the coating method. For PMN calcination, the diffusion rate of PbO is very high due to its low melting temperature of 888°C. Therefore the actual bottleneck of the reaction is the inter-diffusion between MgO and Nb_2O_5. The close contact between Nb_2O_5 and MgO in coating method can significantly ease the diffusion and reaction between them as illustrated by Figure 5.7.

5.4 Summary

In this chapter we showed that several reactions occurred before 500°C during calcinations for the $Mg(OH)_2$-coated Nb_2O_5 powders. These reactions produce very small pyrochlore particles and maintain a configuration of MgO particle mixed uniformly with the Nb_2O_5 particles. The smaller pyrochlore particle size and the better mixing configuration decrease the diffuse distance in reaction and thus help complete the transformation from pyrochlore to perovskite phase near 900°C for the coated powders.

CHAPTER 6: LOW-TEMPERATURE SINGLE STEP REACTIVE SINTERING OF PMN-PT USING A COATING METHODS

Besides finding a one-step calcination method for PMN powder processing as introduced in Chapter 4, another objective of this thesis is to find a simpler, one-step, low temperature sintering method for dense PMN-PT part preparation. The method that can realize this objective is reported in this chapter. The mechanism why our method could decrease the sintering temperature will be discussed in Chapter 7.

6.1 Introduction

As introduced in Chapter 1, many methods had been found for both PMN powder and dense PMN part processing. The major requirements for dense PMN part processing are to prevent the formation of pyrochlore phase, simplify the processing steps, lower the sintering temperature, and avoid the use of expensive raw materials or equipment. So far, no method could meet these requirements simultaneously. In this chapter we will show that, by using the reactive sintering through the coating method, sintering at 1000°C for 2 hours is enough to obtain dense 0.9PMN-0.1PT part with good dielectric properties. With this method only a single ball milling and a single sintering operation are needed without any additional requirements to the raw materials and equipment.

6.2 Experimental Procedure

Similar to Chapter 4, the starting materials used in this study were Nb_2O_5 (99.9% Aldrich), $PbTiO_3$ (99.+%, Aldrich), PbO (99.9+%, Aldrich), $Mg(NO_3)_2.6H_2O$ (99%, Aldrich), MgO(99%, Aldrich) and ammonium hydroxide (5.08N Aldrich). The method of coating $Mg(OH)_2$ on Nb_2O_5 is the same as that described in Chapter 4. Unlike that method, after ball milling, the coated powders were mixed with 3 wt% of an aqueous solution of 5 wt% of polyvinyl alcohol (PVA) for granulation. The granulated powders were then dry pressed at 200 MPa into pellets 2 mm in thick and 25 mm in diameter. We refer to this process as the "coating method".

For comparison, we also prepared samples using the reactive columbite method introduced by Y. C. Liou[47] and the traditional method. For both methods, 0.105 mole MgO was pre-reacted with 0.1 mole Nb_2O_5 to form the columbite phase $MgNb_2O_6$. The calcination took place in an alumina crucible at 1100°C for 10 hours. After that, 0.303 mole of PbO and 0.0333 mole of $PbTiO_3$ were added to the columbite phase and ball-milled in isopropyl alcohol for 20 hours and dried by rotary evaporation. For the reactive columbite method, the powder were mixed with 3 wt% of an aqueous solution of 5 wt% of polyvinyl alcohol (PVA) for granulation and pressed into green bodies with the same pressure as the coating method. For the traditional method, the mixture was calcined at 800°C for 2 hours to form the perovskite phase. Then this reacted powder was ball-milled in isopropyl alcohol for 20 hours and dried. After granulation the mixture was dry pressed into green bodies with the same pressure as the coating method.

The green bodies from all three methods were stacked in the same closed alumina crucible to ensure a same sintering condition. Some perovskite 0.9PMN-0.1PT powders were also placed in the crucible to ensure an atmosphere of saturated PbO vapor. The temperature was raised to 500°C at a heating rate of 3°C/min. After the samples were kept at 500°C for 2 hours to burn out the binder, they were raised to the sintering temperature at a rate of 5°C/min. The samples were held at the sintering temperature for two hours and cooled to room temperature at 5°C/min. Figure 6.1 is the sintering curve. We investigated the sintering temperature of 700°C, 800°C, 900°C, 1000°C, 1100°C and 1200°C respectively and characterized the corresponding properties and microstructures.

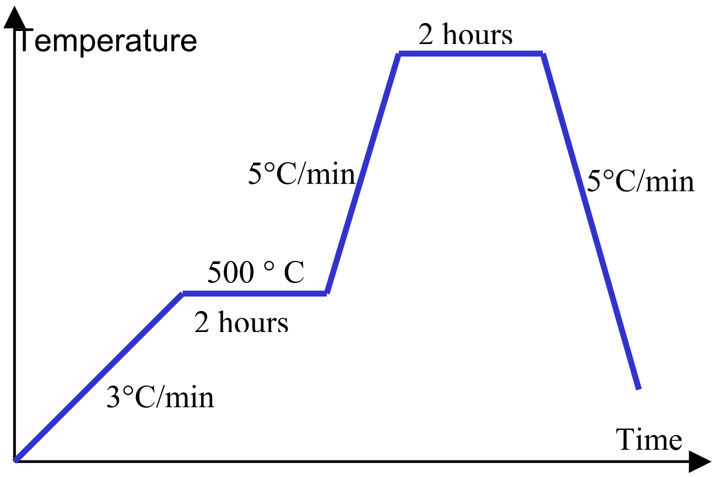

Figure 6.1: PMN-PT sintering curve

The phases of the powders were examined with the X-ray diffractometry (Model D500, SIEMENS, Madison, WI). The sintered density was measured with the Archimedes method in kerosene. The dielectric constant and the loss factor were measured using the HP 4192a LF Impedance Analyzer. Scanning electron microscopy (SEM) (Model 1830, AMRAY, Bedford, MA) was used to examine the fracture surface of the sintered ceramic pieces.

Table 6.1: Percentage of perovskite phase for samples sintered at different temperature for 2 hours

	700°C	800°C	900°C	1000°C	1100°C	1200°C
Coating method	27%	99%	99%	99%	99%	99%
Reactive columbite method	93%	99%	98%	98%	98%	99%
Traditional method	100%	98%	98%	99%	99%	99%

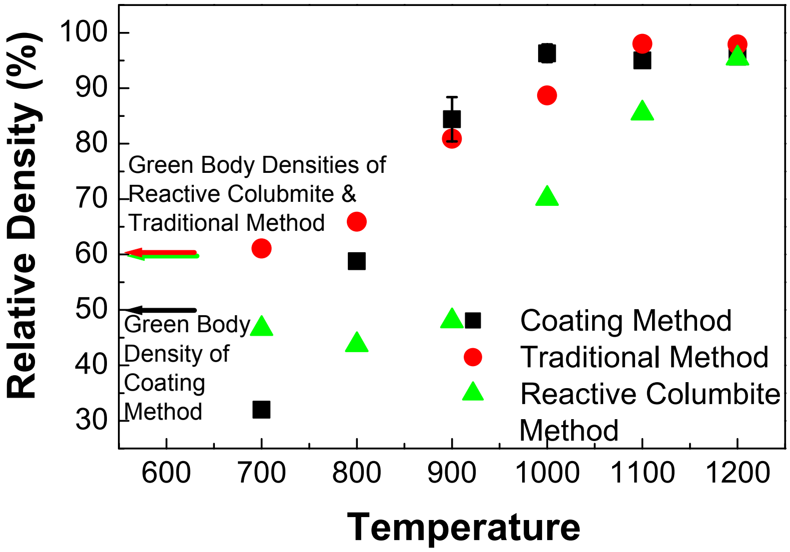

Figure 6.2: Relative density versus sintering temperatures for sintered samples. The error bar here is calculated from three completely independent processing and measurements.

6.3 Results and Discussion

The perovskite phase percentages of sintered samples were listed in Table 6.1. It shows that for both the coating method and the reactive columbite method, a sintering temperature above 800°C is required for the perovskite formation reaction to be complete. Since there were no reactions involved for the traditional method, the final product has nearly pure perovskite phase at all the sintering temperatures studied.

Figure 6.2 shows the densities of sintered samples at different temperatures. The green body density for the coating method is around 50% of the theoretical density. For both the reactive columbite method and the traditional method, the green bodies densities are around 60% of the theoretical density. As can be seen from Figure 6.2, the density after 700°C-2 hours of sintering for the coating methods and the densities after 700°C, 800°C and 900°C-2 hours of sintering for the reactive columbite method were all lower than their respective green body densities. There was already published papers addressed similar phenomenon.[73] [74] [75] In these papers, a large volume expansion was observed upon the perovskite phase formation reaction of the B-site component oxides (TiO_2, ZrO_2, $Zr_{0.53}Ti_{0.47}O_2$, $MgNb_2O_6$) with lead oxide. This expansion is believed to be associated with the unidirectional diffusion of PbO onto the surface of B-site oxide. Since the reaction product possesses larger molar volume than the B-site oxide, a significant volume expansion occurred. As will be seen in Chapter 7, for the coating method, pyrochlore phase formed at this expanding temperature. Similar to the volume expansion during perovskite phase formation introduced in these papers, large volume expansion during pyrochlore formation was observed here. Figure 6.2 also revealed that between 700°C and 1000°C the densification speed for the coating method was higher than that of the reactive columbite method and the traditional method. As a result, 96% of the theoretical density can be reached with only 2 hours of sintering at 1000°C with the coating method. The corresponding sintering temperatures for the traditional method and the reactive columbite method were 1100°C and 1200°C, respectively.

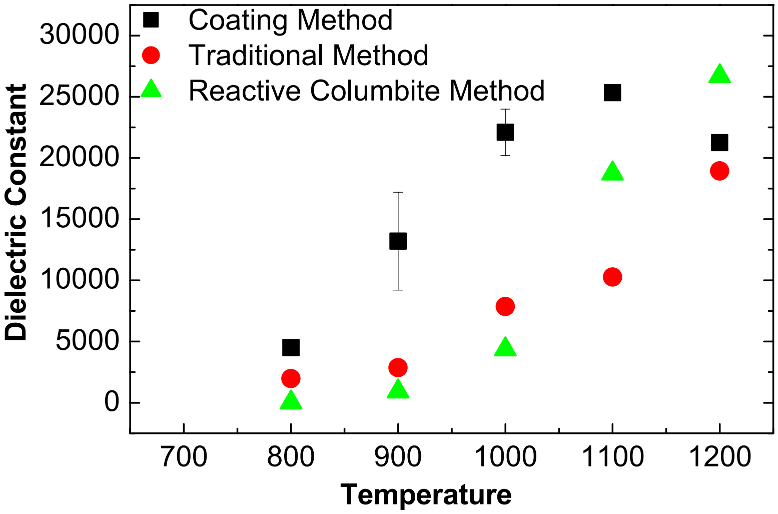

Figure 6.3: Peak dielectric constant measured at 10 KHz versus sintering temperature for sintered samples. The error bar here is calculated from three completely independent processing and measurements.

The peak dielectric constants measured at 10 KHz of sintered samples versus sintering temperature were plotted in Figure 6.3. The dielectric constant at 700°C was not presented because a non-negligible amount of pyrochlore phase still existed at this temperature for samples obtained from the coating method and the reactive columbite method. This figure show that when the sintering temperature was higher than 1000°C, the peak dielectric constant of the samples from the coating method was in the range of 20,000 and 26,000, a good number for 0.9PMN-0.1PT. Also observed in Figure 6.3 is that the dielectric constant peaks at 1100°C for the coating method. Sintering temperature higher than 1100°C decreases the dielectric constant of the sintered samples. This is believed to be caused by the more prominent PbO evaporation loss at higher sintering temperature, which will result in the decomposition of Perovskite phase PMN-PT into non-ferroelectric phase.[43] The relationship between PbO evaporation loss and sintering temperature could be found at Figure 8.1. For the traditional method and the reactive columbite method the dielectric constant increases with the sintering temperature and the dielectric constant is good only when the sintering temperature reaches 1200°C.

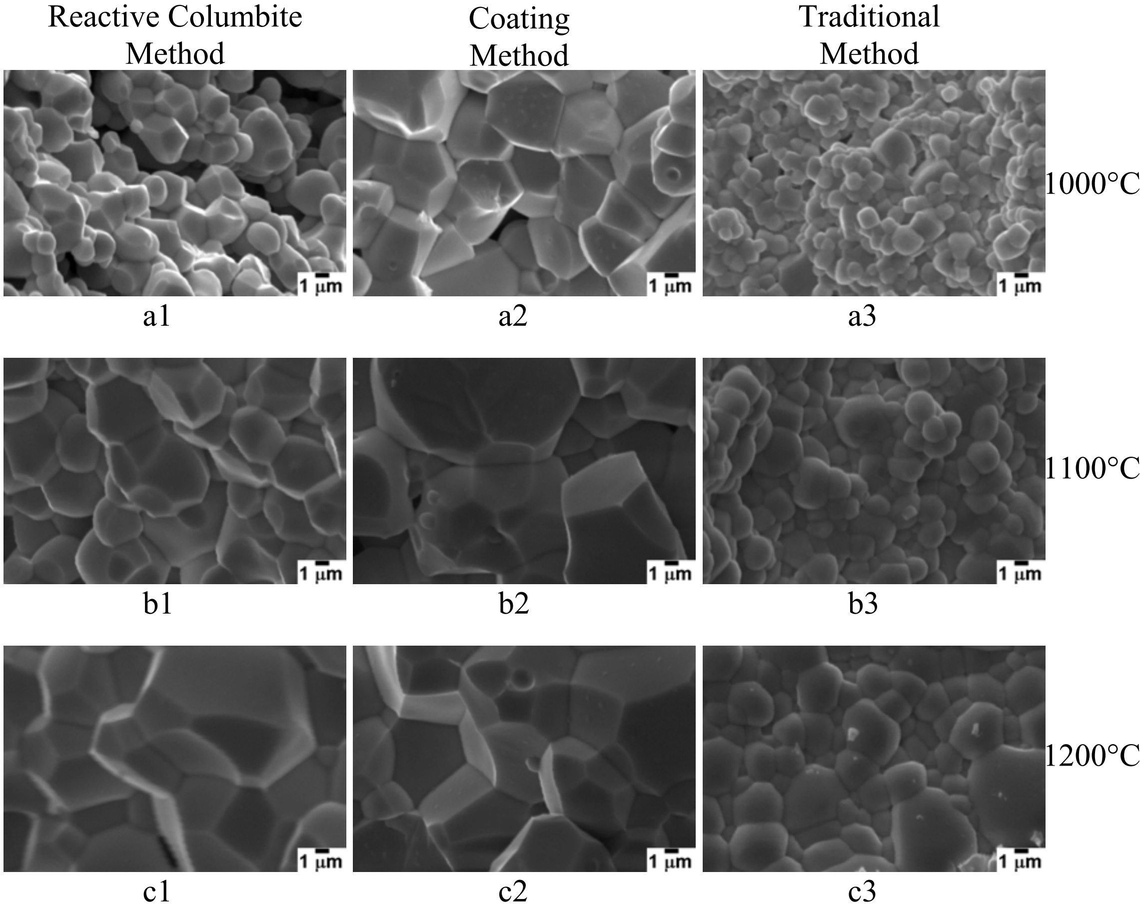

Figure 6.4: SEM fracture-surface micrographs of sintered samples made from the reactive columbite method (a1, b1, c1), the coating method (a2, b2, c2), the traditional method (a3, b3, c3). Row (a) represents the sintering temperature of 1000°C, (b) 1100°C, and (c) 1200°C.

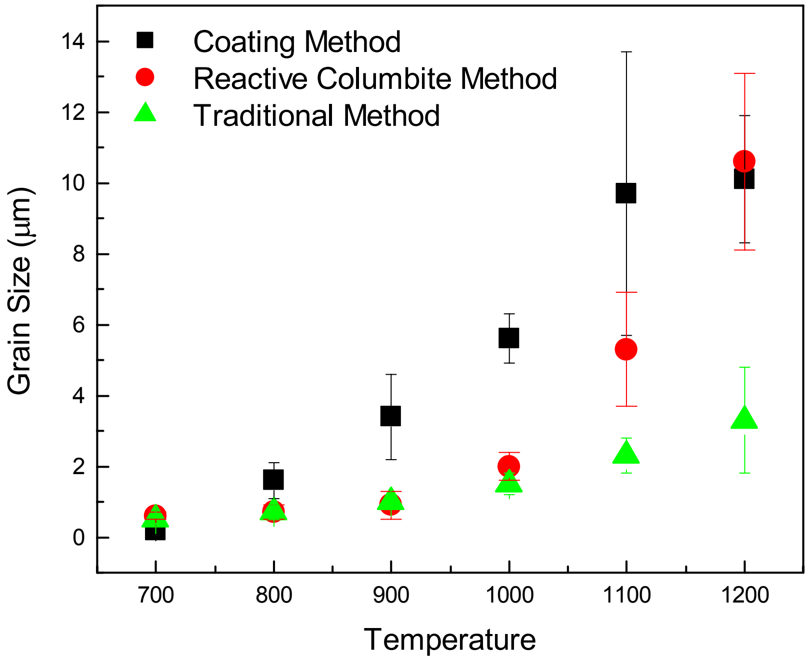

Figure 6.5: Grain sizes counted from SEM pictures versus sintering temperature for the sintered samples.

Figure 6.4 shows the SEM fracture surface pictures of samples sintered at 1000°C, 1100°C, and 1200°C respectively. Figure 6.5 contains a plot of average grain size counted from SEM pictures at difference temperatures. In these two figures, it is clear that the starting coarsening temperature of 900°C for the coating method and 1000°C for the reactive columbite method are lower compared with the 1100°C to 1200°C coarsening temperatures for the traditional method. Also after the completion of sintering, the grain sizes of samples from these two methods were larger than that of the traditional method. The larger dielectric constant of samples from these two reactive sintering methods revealed in Figure 6.3 is believed to be related to the larger grain size discussed above. According to previous studies, the dielectric constant of PMN and some other perovskite ferroelectric ceramics increase with grain size.[76 77] The reasons of the rapid coarsening of these two reactive sintering methods at lower temperature are not clear yet.

To check the applicability of this method to other PMN-PT compositions, pure PMN and 0.65PMN-0.35PT samples were prepared with the same coating method and sintered at 900°C and 1000°C respectively. These two compositions are selected because they are the other two most important compositions except 0.9PMN-0.1PT for PMN-PT. Pure PMN is the composition that many papers used to do basic processing and properties research. As introduced in Chapter 2, 0.65PMN-0.35PT is the composition close to the morphotropic phase boundary (MPB). PMN-PT has superior piezoelectric properties at this composition. The properties of these sintered samples are listed in Table 6.2. The data showed that a good dielectric constant for pure PMN and a reasonable piezoelectric coefficient for 0.65PMN-0.35PT were obtained. The success of the coating method on these two compositions demonstrated that this coating method was equally applicable to other PMN-PT compositions.

The dielectric constant of 22,100±1900 obtained by 1000°C-2hrs sintering of 0.9PMN-0.1PT is slightly higher than the commercial value of ~20,000 and is much higher than the value of 4000 for $BaTiO_3$ or ~10,000 for the modified $BaTiO_3$, which is widely utilized in Multi-Layer-Capacitor (MLC) industry.[78] The piezoelectric coefficient of 306 pC/N obtained by 1000°C-2hours sintering of 0.65PMN-0.35PT is lower than the commercial value of 730 pC/N.[79] This was suspected to be related to the un-optimized PT composition, un-optimized poling conditions, and the lack of dopant such as SrO in our samples.

From the phase, density, grain size and dielectric property data listed above, it can be said that the coating method can indeed lower the sintering temperature of PMN-PT to 1000°C with only a single step of sintering.

Table 6.2: Properties of PMN and 0.65-PMN-0.35PT samples sintered at 900°C and 1000°C for 2 hours

	Relative Density	**% of perovskite phase**	**Room Temperature Dielectric Constant**	**Peak Dielectric Constant**	**d_{33} ($C/N\times10^{-12}$)**
PMN 900°C Sintered	86%	99%	6200	8500	
PMN 1000°C Sintered	95%	98%	11,700	15,600	
0.65PMN-0.35PT 900°C Sintered	80%	99%	1900		260
0.65PMN-0.35PT 1000°C Sintered	96%	98%	3000		306

6.4 Summary

In this chapter, it is shown that by reactive sintering the coated powder, 0.9PMN-0.1PT pieces with good relative density, grain size, and dielectric properties can be obtained at 1000°C. This sintering temperature is lower than that of the traditional method and the reactive columbite method. Due to the reactive sintering, only a single step of coating, ball-milling, and sintering are required to obtain dense PMN-PT pieces.

Further experimental data showed that this coating method works equally well for other PMN-PT compositions.

CHAPTER 7: MECHANISM STUDY OF THE ONE-STEP LOW TEMPERATURE PMN-PT PROCESSING

In previous chapters we have shown that the coating method can eliminate the formation of pyrochlore phase and reduce both the sintering temperature and the processing steps in PMN preparation by reactive sintering. In this chapter, the mechanism for why the coating method can reduce the sintering temperature will be studied.

7.1 Introduction

As introduced in Chapter 1, many PMN low-temperature-sintering methods exist. For example, it was found that excess 5-21 wt% of PbO can decrease the sintering temperature to 950°C.[45] 1-4 at% of SrO doping will lower the sintering temperature to 800-900°C.[46] Using PMN powders made from $Mg(NO_3)_2$ mixing method, the sintering temperature can be decreased to 900°C.[41] By using thermal spray, pre-heat-treatment, directly press and reactive sintering the sintering temperature could be decreased to 1050°C.[42] Liou et al[47] found that by directly pressing the columbite phase and PbO into green body and then sintering, the whole processing steps of dense PMN part could be reduced to 2 ball-millings, 1 calcination, and 1 sintering. But the sintering temperature for this method was 1250°C. Later, with the same method, Kwon et al[48] succeeded in reducing the sintering temperature to 1000°C by using nanosize TiO_2, more reactive $(PbCO_3)_2Pb(OH)_2$ instead of PbO and O_2 sintering atmosphere. We found that by using the coating method the sintering temperature could be decreased to 1000°C without using nanosize powders.

Among these methods, the reactive sintering method is most promising since it could both decrease the sintering temperature and simplify the processing steps. There is no need for a doping substance to be introduced into the lattice. But the mechanism for the decrease of sintering temperature by the reactive sintering is not clear. By using the coating method as an example, the low-temperature reactive sintering mechanisms are studied in this chapter.

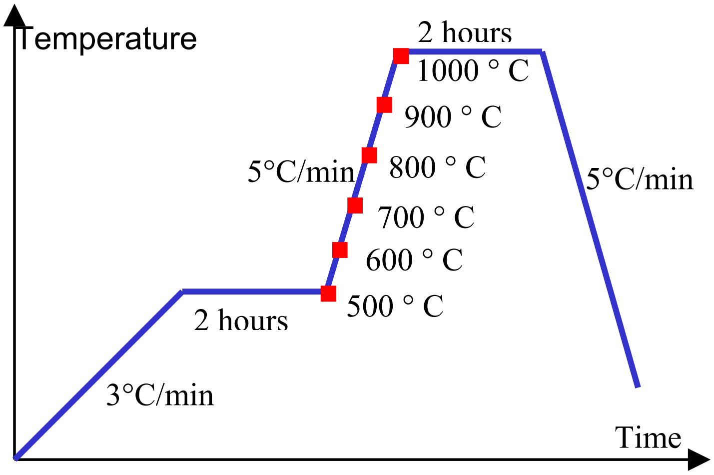

Figure 7.1: Temperature curve for PMN-PT sintering. The squares represent the air-cooling temperatures.

7.2 Experimental Procedure

In order to investigate the mechanism for why the coating method could decrease the sintering temperature, pressed green bodies from the coating method, the reactive columbite method, and the traditional method were air-cooled at 100°C interval between 500°C and 1000°C during sintering as illustrated in Figure 7.1. The air-cooling was realized by pulling the samples directly out of the furnace at the desired temperature and cooled in air. The cooling rate in this method is much higher than cooling within the furnace. Therefore the microstructure, density, phase, and other properties at the corresponding temperatures could be preserved for evaluation similar to the quenching process in metal processing. The composition and the preparation method of green bodies from the coating method, the reactive columbite method, and the traditional method were the same as that described in the experimental procedure part of Chapter 6.

A Quantachrome NOVA 2200 was used to measure the specific surface area of powders. Scanning electron microscopy (SEM: Model 1830, Amray, Bedford, MA) was used to examine the fracture surface of pressed samples. The X-ray diffractometry (XRD, Model D500, Siemens, Madison, WI) was used to identify the crystalline phase. The sintered density was measured with the Archimedes method in kerosene.

7.3 Results and Discussion

Figure 7.2 shows the phase change as a function of air-cooling temperatures for the samples obtained from the coating method and the reactive columbite method. The phases of samples from the traditional method were not listed because they were perovskite from the beginning and did not change during sintering. Figure 7.3 is the percentage of perovskite phase as a function of air-cooling temperature. Figure 7.2(a) shows that the pyrochlore phase formed after 500°C-2 hours of calcination for the coating method. At this temperature, $PbTiO_3$ still has its own peaks, indicating that it has not reacted with other components. On the other hand, at 900°C the diffraction pattern in Figure 7.2(a) shows that the inter-diffuse between the $PbTiO_3$ and the pyrochlore is complete. Figure 7.2(a) and 7.3 also show that the transformation from the pyrochlore to the perovskite phase was completed between 800°C and 900°C. This matched with the 807°C peak in the DTA data (Figure 5.1(a)). Figure 7.2(b) shows how the phases evolve for samples made from the reactive columbite method. It shows that the perovskite phase forms and the $PbTiO_3$ peaks disappear at a temperature between 600°C and 700°C. Unlike the coating method, the perovskite phase in this method does not come from the pyrochlore phase. It comes from the following reaction:

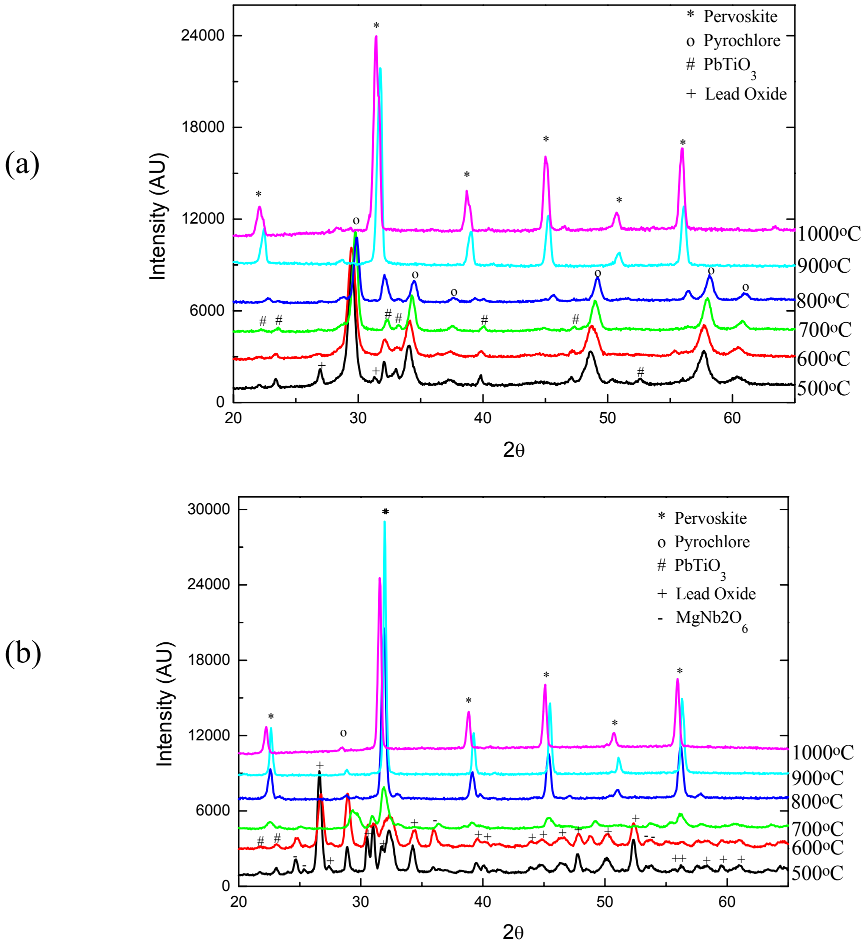

Figure 7.2: The XRD patterns of samples from (a) the coating method (b) the reactive columbite method at different air-cooling temperatures.

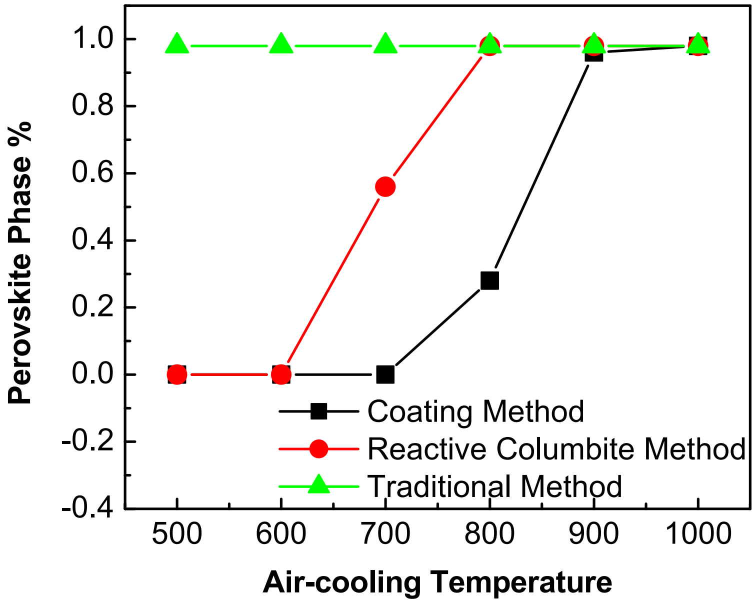

Figure 7.3: Percentage of perovskite phase as a function of air-cooling temperatures.

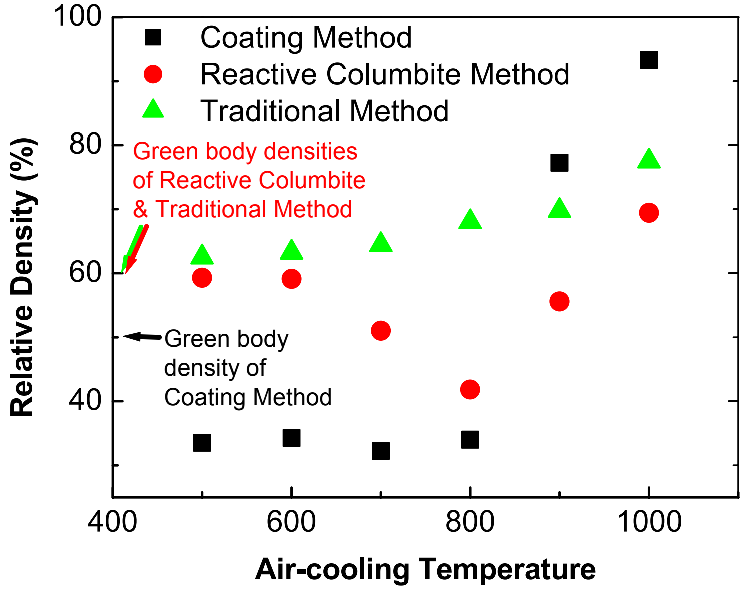

Figure 7.4: Relative densities as a function of temperature for the air-cooled samples. The green body densities are indicated with left arrows.

$$\mathrm{MgNb_2O_6\,(Columbite) + 3PbO \xrightarrow{700°C–800°C} 3Pb(Mg_{1/3}Nb_{2/3})O_3\,(Perovskite)} \quad (7.1)$$

This is the typical perovskite formation reaction from the columbite method.[32] The perovskite formation temperature is roughly 100°C lower than that of the coating method.

Figure 7.4 shows the behavior of relative density of air-cooled samples as a function of temperature. The green bodies from the traditional method and the reactive columbite method were around 60% and the green bodies from the coating method were around 50% of the theoretical density. For both the traditional method and the reactive columbite method, the densities of air-cooled samples are similar when the air-cooling temperature is lower than 600°C. At temperatures higher than 600°C, the density of samples from the traditional method increases with temperature – a typical densification behavior of ceramics. On the other hand, the density decreases as temperature increases between 600°C and 800°C for the reactive columbite method. This was attributed to the volume expansion occurred when PbO reacted with the columbite phase as described in Chapter 6. At temperatures above 800°C, the reaction was completed and rapid density increase was observed. For the coating method, the pyrochlore phase will form after 500°C calcination as shown in Figure 7.2(a) and in Chapter 5. Similar to the reaction between PbO and columbite phase, the reaction between Nb_2O_5 and PbO will also create large volume expansion. Therefore, the density of the samples was lower than the green body density after the calcination at 500°C. Due to the lack of phase transformation and the lack of high enough temperature for sintering, the density does not change much before 800°C. Above 800°C, the rate of density increases with respect to the temperature is the highest among the three methods. The mechanism of this fast sintering behavior will be explained in the later part of this chapter.

Figure 7.5 is the SEM fracture surface pictures of the samples air-cooled at the temperature of 800°C, 900°C, and 1000°C. Figure 7.6 is the average grain size calculated from these SEM pictures. In these two figures, the grain sizes for all methods begin to grow at 800°C. The grain-growth speed of samples from the coating method and the reactive columbite method is much higher than that of the traditional methods.

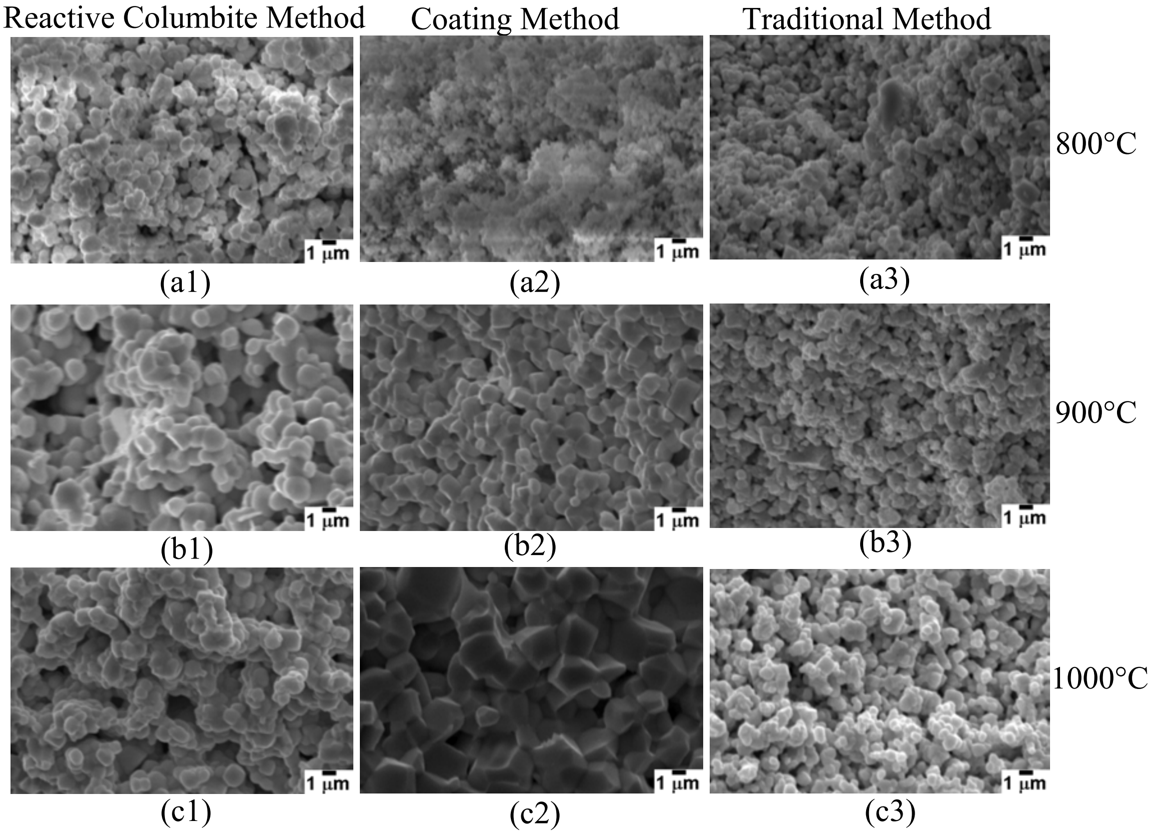

Figure 7.5: SEM fracture-surface micrographs of samples made from the reactive columbite method (a1, b1, c1), the coating method (a2, b2, c2), and the traditional method (a3, b3, c3). Row (a) shows the micrographs of air-cooled at 800°C, row (b) 900°C, and row (c) 1000°C.

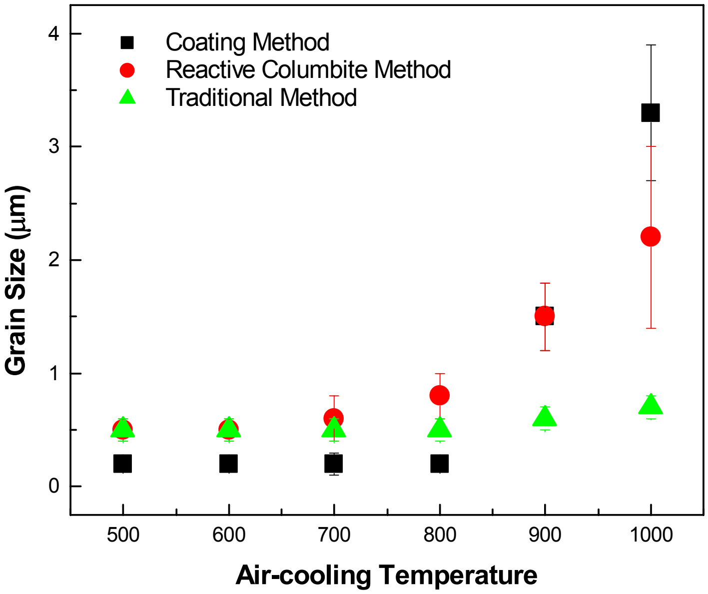

Figure 7.6: Grain size calculated from the SEM micrographs as a function of air-cooling temperature.

Table 7.1: Specific surface area of green bodies and air-cooled samples with the unit of m^2/g. In the parentheses are the particle sizes with the unit nm.

	Coating Method m^2/g (nm)	**Reactive Columbite Method m^2/g (nm)**	**Traditional Method m^2/g (nm)**
Green body	3.0 (250)	1.9 (390)	1.6 (470)
500°C air-cooling	5.7 (130)	1.1 (660)	1.0 (780)
800°C air-cooling	4.2 (180)	1.2 (600)	1.0 (780)

Figure 7.4, 7.5 and 7.6 show the two aspects of sintering: densification and grain growth. These figures suggest that 800°C is the temperature that sintering begins for all these methods.

It should be noted that the SEM pictures in Figure 7.5 are not good enough to give information for particle size smaller than 0.5 μm. In order to obtain information for small particle sizes, specific surface area of green bodies of samples air-cooled at 500°C, and samples air-cooled at 800°C were measured. The results are listed in Table 7.1. The particle size of the samples made from the traditional method increased with temperature. For the reactive columbite method, the particle size of sample air-cooled at 800°C is lower than that air-cooled at 500°C. This phenomenon has been described by Shrout et al.[73] They found that it was related to the reaction between $MgNb_2O_6$ and PbO. During the reaction, the diffusion of PbO into the lattice of $MgNb_2O_6$ caused the volume expansion. This volume expansion could create cracks and break the $MgNb_2O_6$ particle, thus decreasing the particle size. For the coating method, the smallest particle size appeared at 500°C. It could also be explained by the theory of Shrout et al. However, in this case, it is the pyrochlore phase formation reaction before 500°C that causes the volume expansion as suggested by the density data in Figure 7.4. Thus the lowest value of particle size appears at 500°C. This small particle size did not increase much before 800°C because the temperature is not high enough to cause significant grain growth. Table 7.1 showed that the particle size of the coating method were lower than the other two methods for all the three temperatures we investigated.

Until now, two factors that could have significant effect on sintering were compared for all the three methods we investigated: (a) average particle size (b) green body density. The corresponding particle size/density data at 800°C is 180 nm/34% for the coating method, 600 nm/42% for the reactive columbite method, and 780 nm/68% for the traditional method respectively. Based on the data at 800ºC, the contribution of the particle size and the green body density to sintering is compared in the following. We selected data at 800°C instead of data at room temperature for comparison because there is significant reaction-induced density and particle size reduction for both the coating method and the reactive columbite method before 800ºC as discussed in previous paragraphs. The reduction in density and particle size ends at 800ºC as illustrated in Figures 7.4, 7.5, 7.6, and Table 7.1. At the same time, the sintering has not begun yet at 800ºC. Therefore, it is more informative to compare the effect of particle size and densities to the sintering based on data at 800ºC.

The effect of particle size could be studied quantitatively by the Herring's Scaling Law:[80]

$$\Delta t_2(T)=\lambda^n \Delta t_1(T) \qquad (7.2)$$

where $\lambda=r_2/r_1$. r is the diameter of particle. Δt is the sintering time. T is the sintering temperature. The value n depends on the sintering mechanism. n=3 for lattice diffusion mechanism and n=4 for grain-boundary diffusion.

If the sintering rate obeys Arrhenius's law, then

$$\lambda^n = \frac{\Delta t_2}{\Delta t_1} = \frac{A\exp(-\frac{Q_2}{RT_2})}{A\exp(-\frac{Q_1}{RT_1})} = \exp[\frac{Q_1}{R}(\frac{1}{T_1}-\frac{Q_2}{Q_1 T_2})] \qquad (7.3)$$

where Q_1 and Q_2 are the diffusion activation energy of powder with a diameter of r_1 and r_2 at T_1 and T_2 respectively. If $Q_1=Q_2=Q$,

$$\exp[\frac{Q}{R}(\frac{1}{T_1}-\frac{1}{T_2})] = \lambda^n = (\frac{r_2}{r_1})^n \qquad (7.4)$$

Q is a material constant and its value is determined to be 277 KJ/mol for PMN-PT near 1000°C.[81] R=8.315 J/K·mol. According Figure 6.2 and Table 7.1, it is known that the sintering temperature for the traditional method is 1200°C at the average particle size of 780 nm. By using Equation 7.4, it can be calculated that, if n=3 and other conditions remain the same, the sintering temperature will be 964°C for the particle size of 180 nm and 1152°C for 600 nm respectively. If n=4 and other conditions are the same, the sintering temperature will be 902°C for 180 nm and 1136°C for 600 nm respectively. The calculated sintering temperatures are in the same range with the experimental data of 1000°C and 1200°C for the coating method and the reactive columbite method respectively.

Similar calculation on the particle size effect has been successfully applied on other oxide system such as Al_2O_3.[82,83] The calculation is based on several assumptions including, the sintering rate obeys Arrhenius's law, the diffusion activation energy is temperature independent and is the same for different particle size and for both grain-boundary diffusion and lattice diffusion, and the dominant mass transformation mechanism remains the same for all the particle sizes etc. The calculation suggests that smaller particle size for the coating method (180 nm) could decrease the sintering temperature in the order of a few hundred degrees. The corresponding contribution from the reactive columbite method is limited since the average particle size (600 nm) is not small enough compared with that of the traditional method (780 nm).

Besides the particle size, green body density is another factor that may influence the sintering temperature. Unfortunately, there is neither quantitative model nor theory available to evaluate the effect of the green body density to the sintering temperature.

What we know at this moment is that if all the other conditions, including agglomeration condition, are the same, lower green body density will not benefit the sintering.

Besides the differences in particle size and green density, compared with the traditional method, another difference is that reaction is involved in the reactive sintering for both the coating method and the reactive columbite method as shown in both Figure 7.2 and Figure 7.3. In order to investigate the effect of reaction to the sintering, two groups of samples were compared. The first group took the regular sintering route and was sintered at 1000°C for two hours. The second group took a reaction-sintering separated route. The reaction-sintering separated route means that after the samples were kept at 500°C to burn out the binder, they were heated to 800°C at 5°C/min and kept there for another 2 hours to let the reaction complete. Then the temperature was further increased to 1000°C at the rate of 5°C/min and kept there for 2 hours. Finally, the samples were cooled to room temperature at the rate of 5°C/min. The sintering curve was illustrated in Figure 7.7. The only difference between the reaction-sintering separated route and the regular route is the extra step of 800°C-2 hours in the reaction-sintering separated route. According to Table 6.1 and Figure 6.2, after 800°C 2 hours of heat-treatment, the density of samples made from all three methods are still low even though the pyrochlore-perovskite transformation reaction has been completed. As a result, the reaction-sintering separated route is designed to separate the reaction process from the sintering process. Table 7.2 is the density data for the two routes. According to the sintering theory, the density of ceramics obtained by the reaction-sintering separated route should not be lower than that of the regular route, since the samples were kept at high temperatures longer. This was what happened to samples made from the traditional method. But for samples made from the coating method and the reactive columbite method, the density by the reaction-sintering separated route was lower than that of the regular route. The density comparison is 76% vs. 94% for the coating method and 61% vs. 70% for the reactive columbite method. According to the sintering data of the traditional method in Figure 6.2, the difference in density of 76% and 94% corresponds to ~200°C difference in sintering temperature. Similarly, the difference in density of 61% and 70% corresponds to ~100°C difference in sintering temperature. The result suggests that if the sintering and reaction occurred in the same temperature range, the reaction can improve sintering significantly. This conclusion can also be shown by the higher densification rate of the coating method and the reactive columbite method compared with the traditional method between 800°C and 1000°C in Figure 7.4.

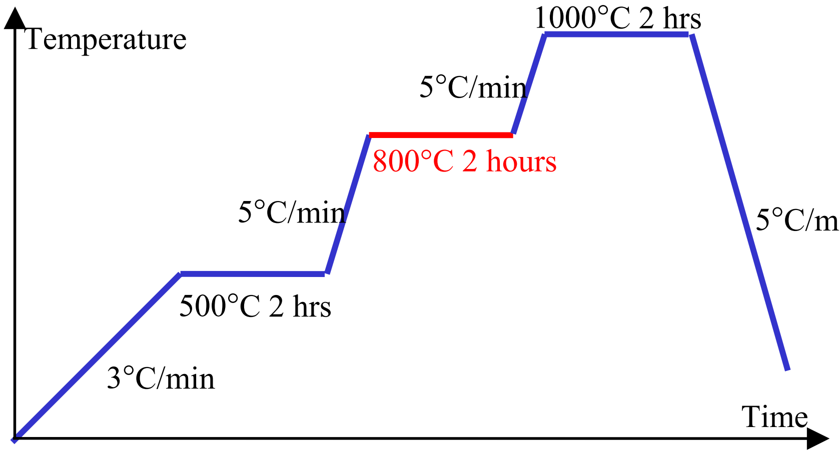

Figure 7.7: The reaction-sintering separated route for PMN-PT, it has an extra step of staying at 800°C for 2 hours

Table 7.2: Relative densities of sintered samples at 1000°C for 2 hours, the reaction-sintering separated route has an extra step of staying at 800°C for 2 hours

	Coating Method	**Reactive Columbite Method**	**Traditional Method**
Regular route	94%	70%	89%
Reaction-sintering separated route	76%	61%	89%

From Figure 7.2 and 7.3 it is clear that the perovskite phase formation reaction temperature is between 600°C and 800°C for the reactive columbite method and 700°C to 900°C for the coating method. From Figure 7.4, the sintering occurred mainly at 800°C and above. The overlap between the reaction and the sintering is limited for the reactive columbite method while there is at least 100°C overlap for the coating method. Due to its relative larger overlap with the sintering, the reaction could be more beneficial to the sintering in the coating method than in the reactive columbite method. This could explain the relatively larger density difference in Table 7.2 and relatively higher densification rate in Figure 7.4 for the coating method over the reactive columbite method.

Similar reaction-enhanced sintering phenomena have been observed in other reactive sintering system. For example, the formation of α-Al_2O_3 from γ-Al_2O_3 with wet chemical method occurs via a series of poly-morphic transformations on heating: γ-Al_2O_3 $\rightarrow$ δ-Al_2O_3 $\rightarrow$ θ-Al_2O_3 $\rightarrow$ α-Al_2O_3, where θ-Al_2O_3 transforms to α-Al_2O_3 at temperatures as high as 1200°C.[84] Kumagai and Messing demonstrated that the boehmite gels, when seeded with some α-Al_2O_3 can be sintered to nearly full density at 1200°C, much lower than the normal >1600°C sintering temperature.[85, 82] Kong and Ma demonstrated that the linear sintering rate/sinterability of PbO, ZrO_2, and TiO_2 oxide mixture is significantly higher than that of the perovskite PZT powders.[86] However the mechanism of how the reaction could enhance reaction is not clear. We think the following qualitative kinetics analysis may help explain the phenomena. Figure 7.8 is a diagram for regular and reactive sintering processes. The major mass transport mechanism for sintering includes grain-boundary diffusion, lattice diffusion, surface diffusion, viscous flow, and evaporation-condensation. For most inorganic powders, the diffusion mechanisms are dominant.[87] For very small particles, the most efficient processes are grain boundary and surface diffusion.[88] Due to the solid-state reaction, more grain boundaries will be created during reaction and sintering for the reactive sintering as demonstrated as in Figure 7.8. Therefore, larger area of grain-boundaries would be available for diffusion in the reactive sintering than the regular sintering. In addition, in the reactive sintering case, for the reaction to complete the grain-boundaries will move along the arrow as illustrated in Figure 7.8 from the initial contact point P until both A and B are completely consumed. Due to the lattice mismatch, the defect density, such as dislocation and vacancy, is much higher along grain boundary than that in the grain body. As the grain-boundaries move through A and B, these defects will be left in C. These defects will not reach equilibrium concentration immediately in the grain body C and their existence could significantly improve the diffusion and sintering.

In summary, based on the experimental data that we obtained, the following is what we think is happening during the reactive sintering of samples from the coating method. When the samples were heated to 500°C and kept for 2 hours, PbO, Nb_2O_5 and some MgO reacted to form pyrochlore phase. This reaction created a significant amount of volume expansion. The volume expansion decreases the density. However this volume expansion also breaks down particles and decreases the particle size. The decreased particle size could lower the sintering temperature in the order of a few hundred degrees. At temperatures higher than 700°C, the pyrochlore and perovskite phase transformation began and was completed at 900°C. This phase transformation reaction could further lower the sintering temperature by ~200°C. As a result of the combined effects of volume expansion, smaller particle, and the reaction, the samples were sintered after 1000°C-2 hours of heat treatment. Similar to the coating method, the reactive columbite method also involves volume expansion, density decrease, particle size reduction and the columbite-perovskite transformation reaction. But Table 7.1 showed that the particle size decrease caused by the columbite reaction was not significant. In addition, the temperature range overlap of reaction and sintering is limited. So the combined benefits from the reaction and smaller particle size to sintering were not as significant as that of the coating method. Therefore, the sintering temperature of the reactive columbite method was not lower than that of the traditional method.

7.4 Summary

Several factors influenced the PMN-PT reactive sintering. For the coating method, there is a particle size decrease during pyrochlore phase formation which is beneficial to sintering. Further investigation shows that the solid-state reaction also enhances sintering.

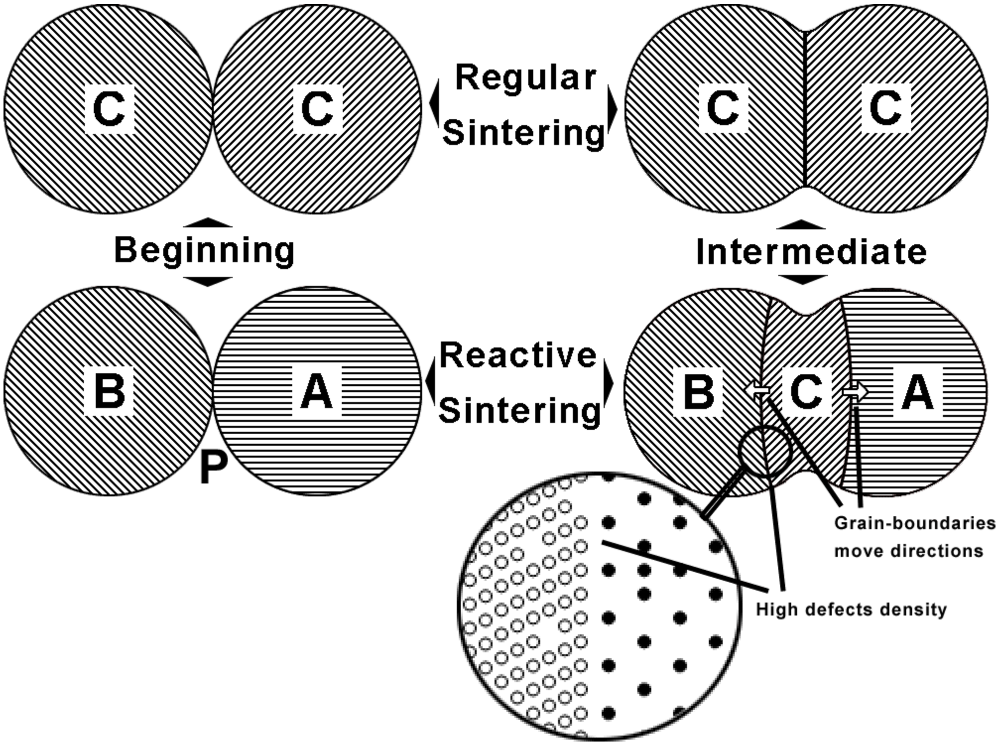

Figure 7.8: regular sintering and reactive sintering process. The lines represent the crystal orientation. A and B are the reactants and C is the solid state reaction product. For the case of intermediate stage, two grain-boundary faces created for reactive sintering instead of one for regular sintering.

CHAPTER 8: LEAD OXIDE EXCESS EFFECT IN PMN-PT AND PROCESSING OPTIMIZATION

In previous chapters it was shown that the coating method could generate almost pure perovskite phase and reduce both the sintering temperature and processing steps by reactive sintering. We will show here that PbO composition has a significant effect on the properties of PMN-PT. In order to find an optimized PbO composition for this coating method and investigate the phenomena accompanying the PbO composition variation, the effect of excess PbO in the reactively sintered PMN-PT through the coating method is studied in this chapter.

8.1 Introduction

Since the discovery of pyrochlore free PMN processing methods, many studies have been devoted to understand the effect of excess component composition on the dielectric properties, density, microstructure, and phase of PMN or PMN-PT. It is generally agreed that excess MgO up to 5 at% could increase the maximum dielectric constant and decrease the transition temperature.[89, 90, 91] This is because the excess MgO could reduce the percentage of pyrochlore phase formed and enhance grain growth during sintering. In samples with MgO excess, MgO rich precipitates were observed in the grains or between the grain boundaries. Despite understanding the effect of excess MgO, the effect of excess PbO is still uncertain. For example, it was found that PbO would form a thin layer in the order of 1nm in thickness between the grain boundaries in PMN.[92] It was generally agreed that, because of the poor dielectric properties of PbO, this layer was detrimental to the dielectric properties.[89, 90, 92] However, Gupta et al[93] found that excess PbO could improve dielectric constant of PMN and others[94, 95] found that there were no strong effect of PbO. Also it was found that excess PbO would produce a PbO rich liquid phase during sintering and this liquid phase could help decrease the sintering temperature.[45] However Costa et al[42] recently claimed that the formation of a PbO rich liquid phase was not responsible for the increase in density as compared with samples obtained by solid-state reaction of oxides. Furthermore, some reports[89, 95] showed that excess PbO will help decrease the amount of pyrochlore phase in the final ceramic, while others showed that the amount of pyrochlore phase has no relationship with the PbO excess.[90]

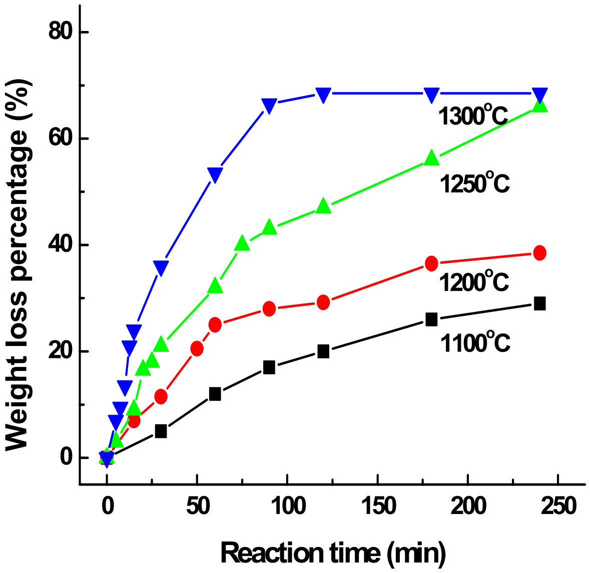

Figure 8.1: Weight loss of $Pb(Mg_{1/3}Nb_{2/3})O_3$ as a function of reaction time.[96]

The inconsistencies described above are related to the volatile nature of PbO at temperature higher than 1000ºC. Figure 8.1 is the weight loss behavior of PMN caused by PbO evaporation.[96] It was shown that 1200ºC-2 hours of heat treatment could cause PbO loss to be as much as 25 wt%. Almost all of the current excess PbO effect studies used the traditional columbite method to prepare the PMN samples, which involved a sintering temperature of 1200ºC. Such a high sintering temperature creates significant PbO loss, thus causing uncertainty in the PbO content in the sintered PMN samples.

In this chapter, the effect of PbO excess in PMN will be examined using the coating method involving reactive sintering. The advantage of this method is that the sintering temperature could be decreased to 1000ºC without doping. At this temperate, PbO loss could be greatly suppressed compared with the traditional 1200ºC sintering. The objective of this study is to provide a more precise understanding to the effect of PbO excess in PMN-PT.

8.2 Experimental Procedure

The sample preparation methods used in the chapter were similar to that described in previous chapters. The compositions investigated were 0.9PMN-0.1PT with 99 at%, 100 at%, 100.5 at%, 101 at%, 102 at%, 105 at%, and 110 at% of stoichiometric PbO content. Here < 100 at% represents PbO deficient, while > 100 at% represents PbO rich. For convenience, these samples were named 0.9PMN-0.1PT-99, 0.9PMN-0.1PT-100, 0.9PMN-0.1PT-100.5, 0.9PMN-0.1PT-101, 0.9PMN-0.1PT-102, 0.9PMN-0.1PT-105, and 0.9PMN-0.1PT-110 respectively.

After the green bodies were prepared as described in previous chapters, they were sintered in a double-closed-crucible setup as illustrated in Figure 8.2. In this setup, the pellets were placed in a small alumina crucible slightly larger than the pellets first. This small crucible was then loaded into a larger alumina crucible. Some amounts of perovskite 0.9PMN-0.1PT powders were placed between the two crucibles to ensure an atmosphere of saturated PbO vapor. Finally, the crucibles together with samples were raised to 500ºC for two hours for binder burnout and then sintered at 800ºC, or 900ºC, or 1000ºC for two hours at the heating rate of 5ºC/min. This double-closed-crucible setup could significantly suppress the PbO loss. But it still cannot fully prevent it. After many cycles of sintering, very light yellow PbO color was observed on the inner wall of the inner crucible indicating some PbO loss during sintering.

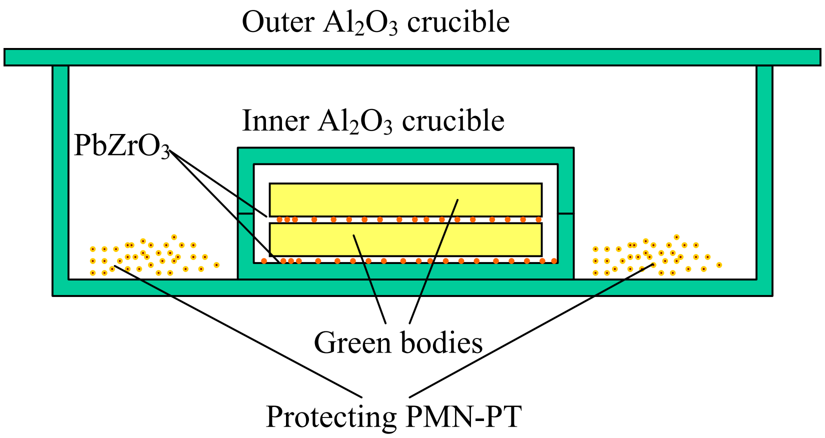

Figure 8.2: Double-close-crucible sintering setup with perovskite PMN-PT powder as protecting atmosphere and $PbZrO_3$ between samples to keep the samples separate after sintering.

Similar to previous chapters, the phases of the samples were examined by the X-ray diffractometry (XRD; Model D500, Siemens, Madison, WI). The sintered density was measured using the Archimedes method in kerosene. The dielectric constant and the loss factor were measured using an impedance analyzer (Model HP 4192a LF, Hewlett–Packard, Palo Alto, CA). Scanning electron microscopy (SEM; Model 1830, AMRAY, Bedford, MA) was used to examine the fracture surfaces of the sintered ceramics.

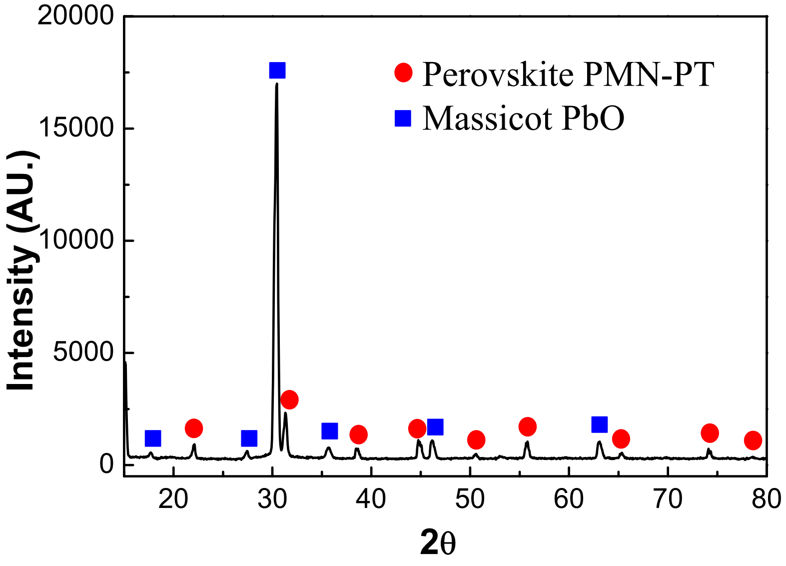

Figure 8.3: Surface XRD patterns of 0.9PMN-0.1PT-110 sintered at 1000°C

8.3 Results and Discussion

8.3.1 Phase

Figure 8.3 is an X-ray diffraction pattern for the surface of 0.9PMN-0.1PT-110 sintered at 1000°C. It showed that the phases on the sample surface are a mixture of perovskite PMN-PT and Massicot PbO. Phase analysis on all other samples showed that, except the 0.9PMN-0.1PT-99, all the samples sintered at 900°C and 1000°C have both Massicot PbO and perovskite phase on the surfaces. However, none of the samples sintered at 800°C have surface Massicot PbO peaks.

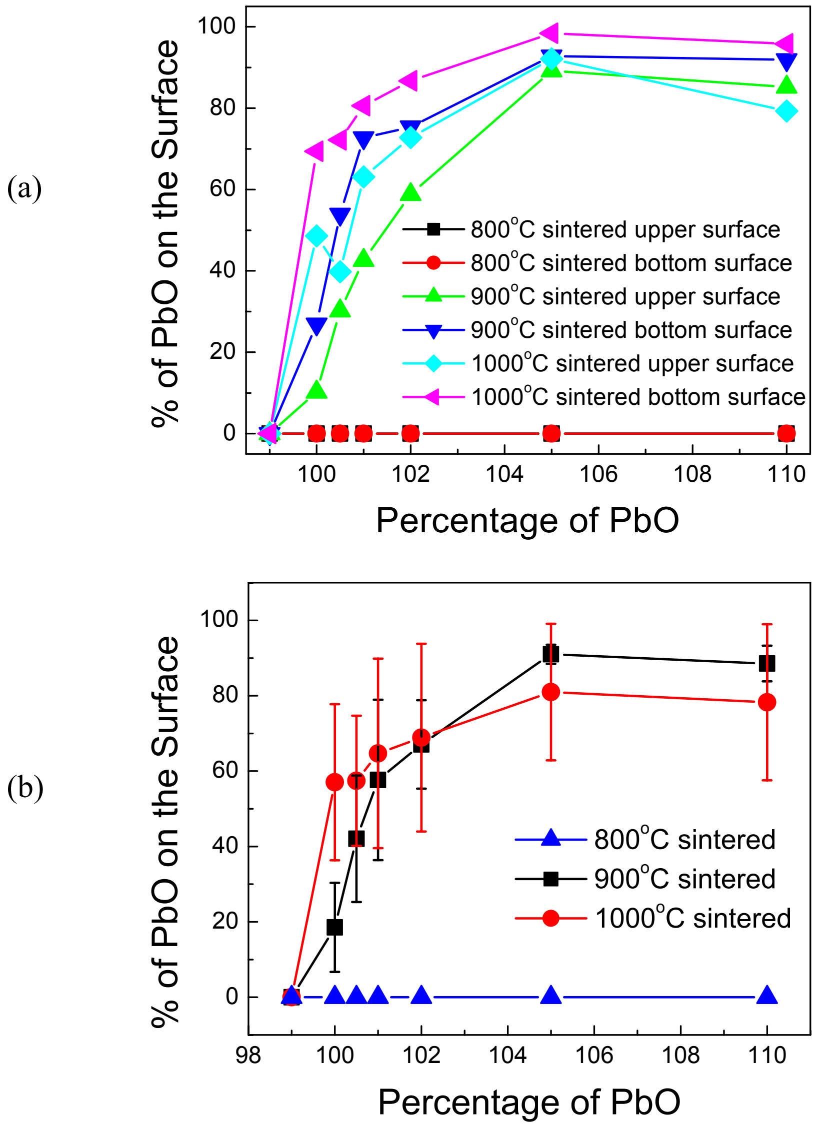

Figure 8.4: (a) Surface Massicot PbO phase percentage vs. PbO composition. Here upper surface and bottom surface refer to the two different surfaces of a sample during sintering. (b) An average of the surface Massicot PbO phase percentage for all the samples studied.

Figure 8.4(a) shows the surface Massicot PbO percentage as a function of the starting PbO amount. The percentage of Massicot PbO here was calculated from the X-ray diffraction data using the following equation:

$$\text{Content of compound i}(\%) = \frac{\text{major peak intensity of the compound i}}{\sum_{i} \text{major peak intensity of the compound i}} \qquad (8.1)$$

There are two sets of data for each sample in this figure. The two sets of data represent the upper surface and bottom surface of a sample. Figure 8.4(b) shows the behavior of the average surface Massicot PbO percentage. From Figure 8.4(a), it is clear that, for those samples that have Massicot PbO phase on the surface, the bottom surface of the sample always has more Massicot PbO than the upper surface. From Figure 8.4(b), it is clear that the amount of surface Massicot PbO increase with the amount of starting PbO.

After X-ray diffraction analysis, SEM pictures were taken on the upper surfaces of the samples. Except sputtering a very thin layer of gold in the order of a few nano-meters in thickness for the purpose of SEM sample preparation, no other treatments such as polish or etching were performed on the sample surface. These pictures should reflect the as-sintered surface condition. Totally more than 40 pictures were taken. Figure 8.5 shows the pictures of 0.9PMN-0.1PT-99 and 0.9PMN-0.1PT-105 sintered at 800°C, 900°C, and 1000°C respectively. In Figure 8.5(d) and (f), plate structures with dimension in the order of $30\times30\times1\mu m$ were observed on the samples sintered at 900°C or 1000°C. Figure 8.6(a) is the EDX analysis result of the plate structure. Compared with the perovskite phase EDX result in Figure 8.6(b), it can be determined that the plate is mainly composed of PbO together with ~10 mole% of Nb_2O_5. Considering the X-ray diffraction results showed that the sample surface is mainly PbO Massicot phase and perovskite phase, it can be concluded that the Nb_2O_5 exists as a solid solution in PbO lattice. Furthermore, by analyzing the X-ray diffraction data for all the PbO starting compositions and using the PMN perovskite phase peak of (110) at $2\theta=31.1370$ as reference, the surface PbO peak position of (020) was determined to be $2\theta=30.174\pm0.025$ (d=2.959±0.007Å), which is smaller than the data of $2\theta=30.3153$ (d=2.9459Å) given by ICDD PDF (Powder Diffraction File). This smaller lattice constant value in our samples further proved the existence of Nb_2O_5 as solid solution in the PbO lattice. The smaller lattice constant value is believed to be caused by the dissolution of smaller Nb^{5+}, compared with the size of Pb^{2+}, in the PbO lattice. As shown in Figure 8.5(a), (c), and (e), the PbO plates don't show up on the surface of 0.9PMN-0.1PT-99. It was also found that, except 0.9PMN-0.1PT-99, the surface PbO plates appeared on all samples sintered at 900°C and 1000°C. For those samples that show surface PbO plates, the surface area covered by PbO plate increased from ~3% for 0.9PMN-0.1PT-100 to ~30% for 0.9PMN-0.1PT-110 for both 900°C and 1000°C sintered samples.

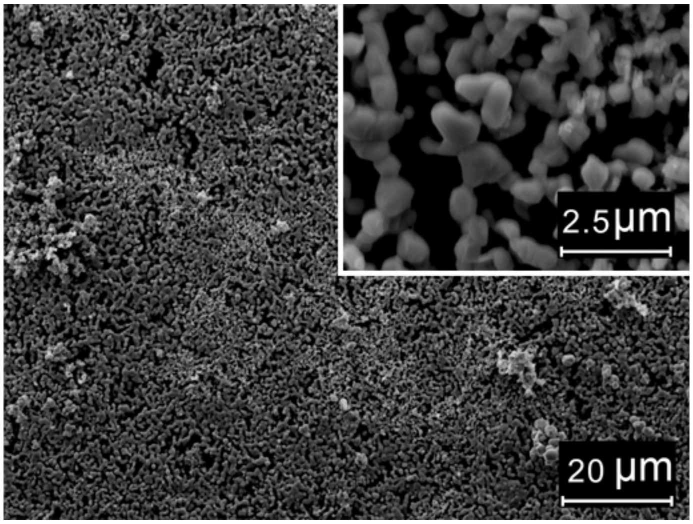

(a)

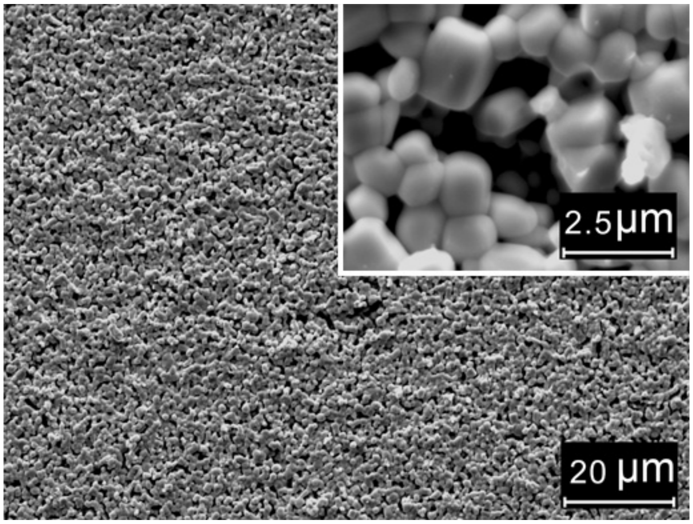

(b)

Figure 8.5: SEM micrograph of (a) 0.9PMN-0.1PT-99 sintered at 800°C (b) 0.9PMN-0.1PT-105 sintered at 800°C (c) 0.9PMN-0.1PT-99 sintered at 900°C (d) 0.9PMN-0.1PT-105 sintered at 900°C (e) 0.9PMN-0.1PT-99 sintered at 1000°C (f) 0.9PMN-0.1PT-105 sintered at 1000°C

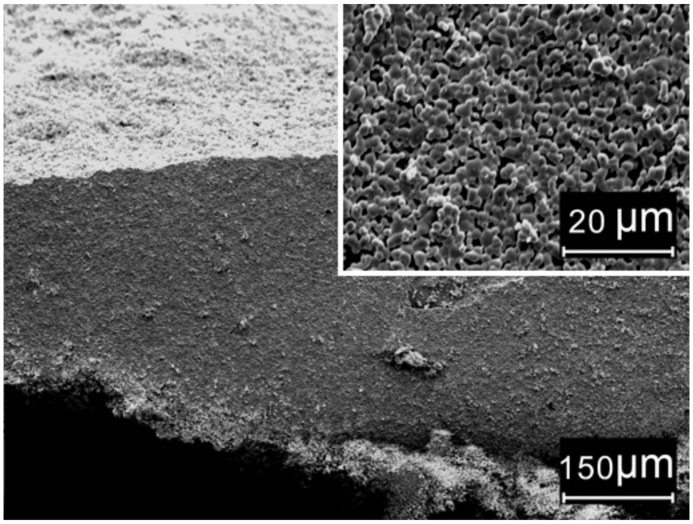

(c)

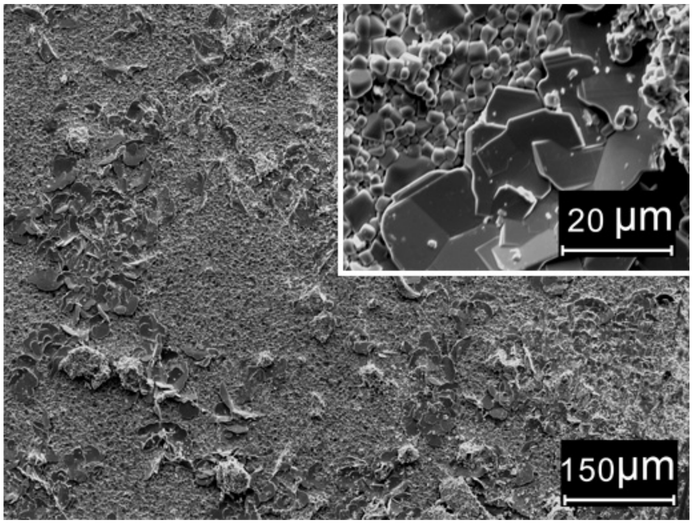

(d)

Figure 8.5 (continued)

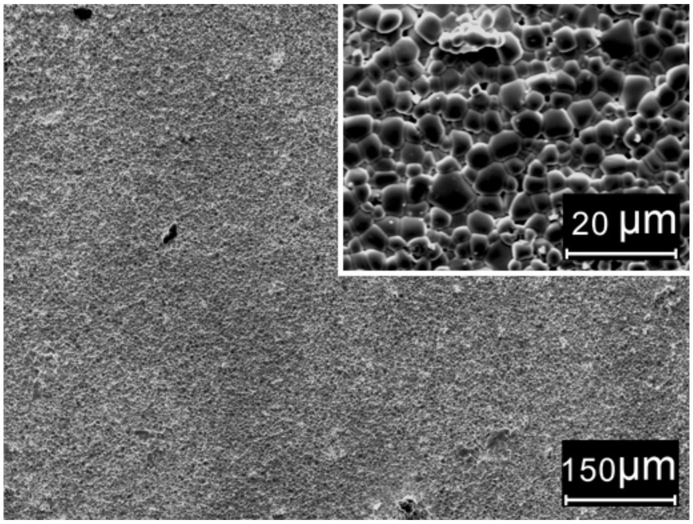

(e)

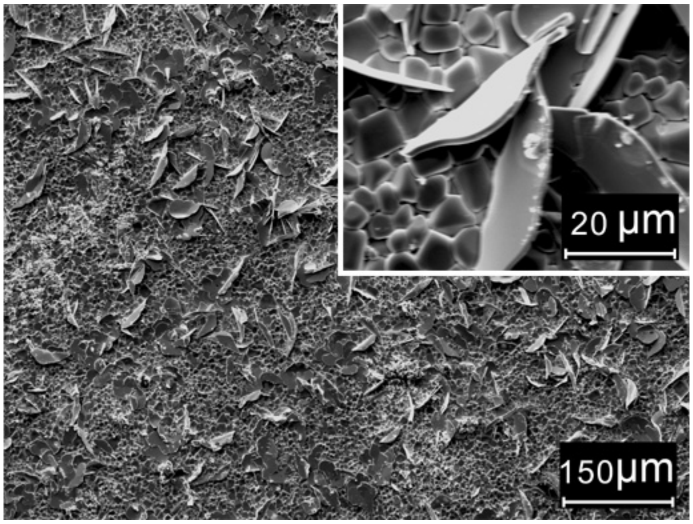

(f)

Figure 8.5 (continued)

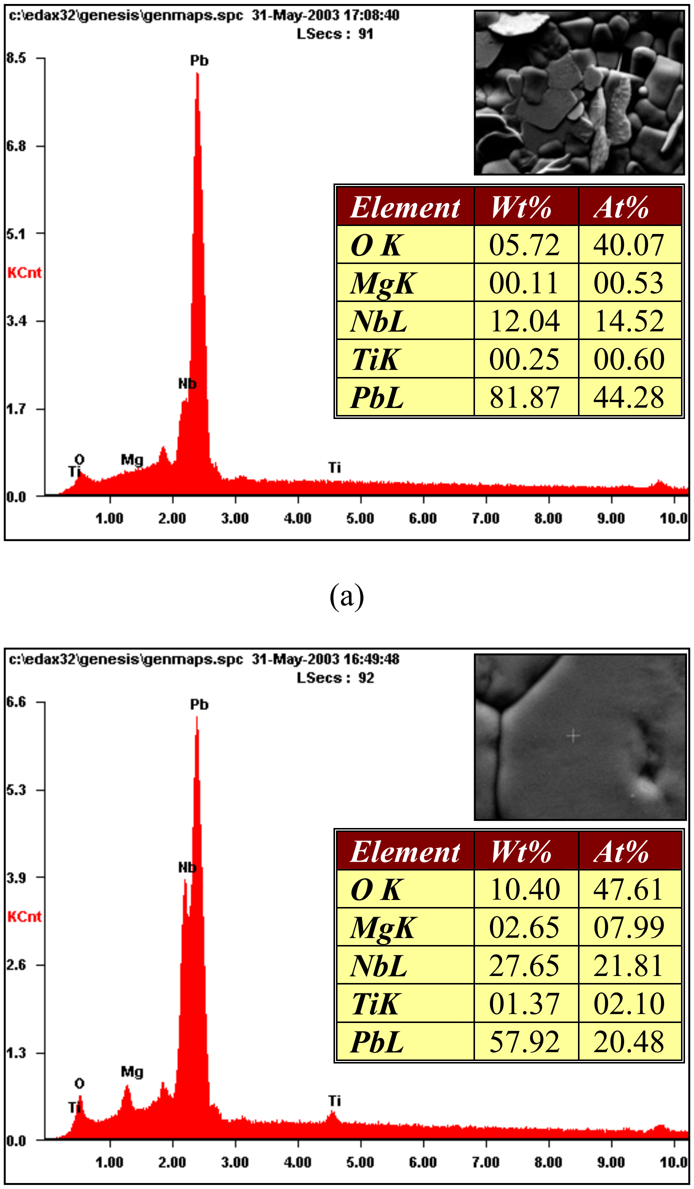

Element	*Wt%*	*At%*
O K	05.72	40.07
MgK	00.11	00.53
NbL	12.04	14.52
TiK	00.25	00.60
PbL	81.87	44.28

(a)

Element	*Wt%*	*At%*
O K	10.40	47.61
MgK	02.65	07.99
NbL	27.65	21.81
TiK	01.37	02.10
PbL	57.92	20.48

(b)

Figure 8.6: SEM-EDX analysis of (a) surface PbO plate (b) perovskite PMN-PT

In order to investigate the depth of these surface PbO plates, a very thin layer in the order of a few hundred microns was polished off the sample surface. Then the samples were analyzed again using the X-ray diffraction. The results showed that the

PbO oxide peak disappeared with only perovskite peaks left. Table 8.1 lists the percentage of perovskite phase inside the samples by using X-ray diffraction data and equation (8.1). These data showed that the coating method could produce almost pure perovskite phase inside the sintered samples independent of the presence of surface PbO or not. No clear relationship between the amounts of perovskite phase formed and the PbO excess amount was found. These perovskite phase percentage data also showed that the Massicot PbO only exists in a very thin surface layer.

Table 8.1: Percentage of perovskite phase in the bulk of the sintered samples for different sintering temperatures and PbO excesses

Samples	**Perovskite Phase Percentage**		
	1000°C Sintering	**900°C Sintering**	**800°C Sintering**
0.9PMN-0.1PT-99	98%	98%	99%
0.9PMN-0.1PT-100	99%	98%	99%
0.9PMN-0.1PT-100.5	98%	98%	97%
0.9PMN-0.1PT-101	99%	98%	99%
0.9PMN-0.1PT-102	98%	97%	98%
0.9PMN-0.1PT-105	98%	96%	96%
0.9PMN-0.1PT-110	97%	98%	98%

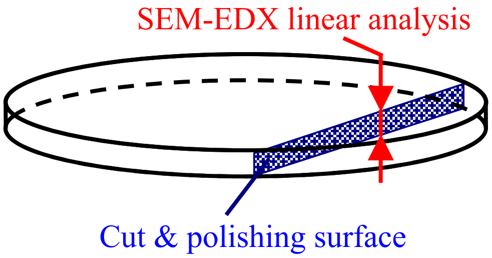

Figure 8.7: Cut and polishing surface and SEM-EDX linear analysis path.

To understand the behavior of the surface Massicot PbO further, freshly sintered samples were cut and polished perpendicular to the surface as drawn in Figure 8.7. The samples used here were not the samples that were polished off the surfaces for phase analysis. They still contained the surface information. After cutting and polishing as in Figure 8.7, linear EDX with the step of 5 μm was used to analyze the distribution of Pb element along the cross section. The result showed that Pb was distributed quite uniformly along the cross section. This means the Massicot PbO plates exist only on a very thin layer of less than 5 μm in thickness on the surface. This result is consistent with the X-ray diffraction analysis in previous paragraph. These polished samples were thermally etched at 900°C for 1 hour in an open crucible in air and then were observed in SEM again. The Thermal etching is a technique that relieves the higher energy associated at the grain boundaries of a material by heat treatment at a temperature below the sintering temperature. The result is that the grain boundary edge will become rounded so that it can be evaluated by optical or electron microscope techniques. Depending upon the ceramic material, the atmospheric condition of the furnace may need to be controlled. For example, etching silicon nitride will require either a vacuum or an inert atmosphere of nitrogen or argon to prevent oxidation of the surface to silicon dioxide. However no special atmosphere is required for PMN-PT thermal etch due to its good oxidation resistance and relative easy grain-boundary phase evaporate. SEM results of all the thermally etched samples showed that PbO plates appeared again on the polished surfaces of these samples that have surface PbO plates right after sintering. Figure 8.8 is the SEM pictures for the sintered 0.9PMN-0.1PT-105 thermally etched at 900°C and 1000°C. From Figure 8.8, it is clear that the PbO plates sit above the polished surface. Since the thermal etching is undergone at relative low temperature for grain-boundary energy relief and evaporation only, it is not unreasonable to say the polished surface is almost unchanged before and after thermal etching. In addition, the thermal etching occurred in an open environment, these PbO plates cannot come from evaporation and condensation mechanism. So the only possible source of these PbO plate is the bulk of the sample. Here we call the process of PbO moving from inside the sample to the surface extrusion. Another phenomenon noticed by comparing pictures in Figure 8.5 and Figure 8.8 was that the relative amount of surface PbO extruded by thermal etching is less than the amount of surface PbO extruded by sintering. Considering thermal etching occurred at 900°C for 1 hour, while sintering was 2 hours of heat-treatment at 900°C or 1000°C, it is very possible that the extruded PbO amount is time dependent. The longer the heat-treatment time, the more PbO is extruded.

To summarize, for the first time, Massicot PbO plates were observed on the surface of sintered PMN. The presence of this surface Massicot PbO layer indicates that, with the sintering temperature and sintering setup we used, the PbO evaporation was not very prominent. Otherwise surface PbO will be evaporated and no surface PbO could be observed just like what were observed from samples made from traditional columbite method. Therefore, it can be concluded that PbO is well preserved in our samples. With this in mind, the effects of PbO excess on sintering and properties will be discussed in the following.

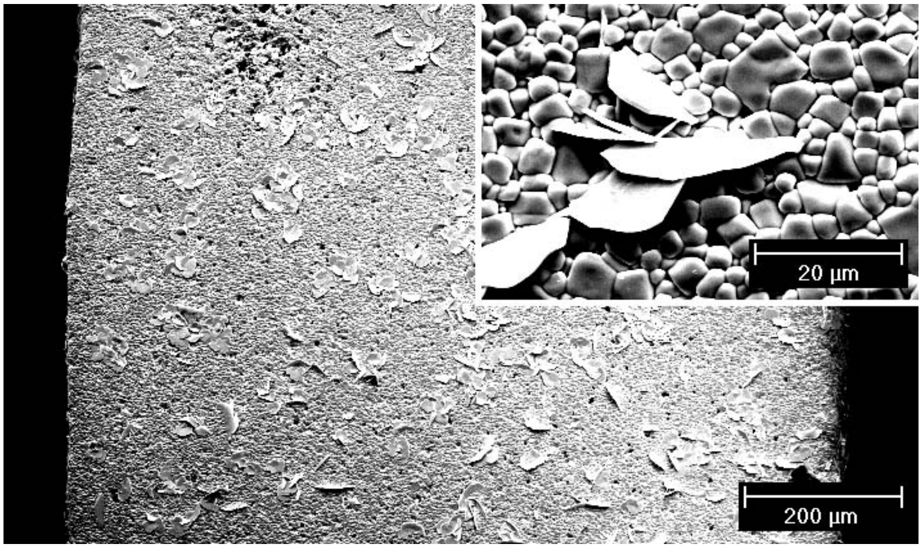

(a)

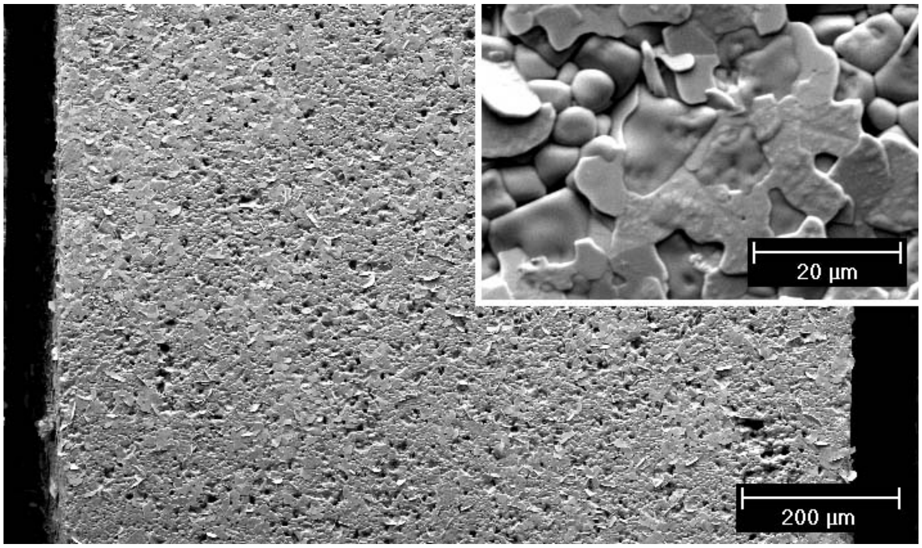

(b)

Figure 8.8: SEM micrograph of sintered 0.9PMN-0.1PT-105 thermally etched for 1 hr at (a) 900°C and (b) 1000°C

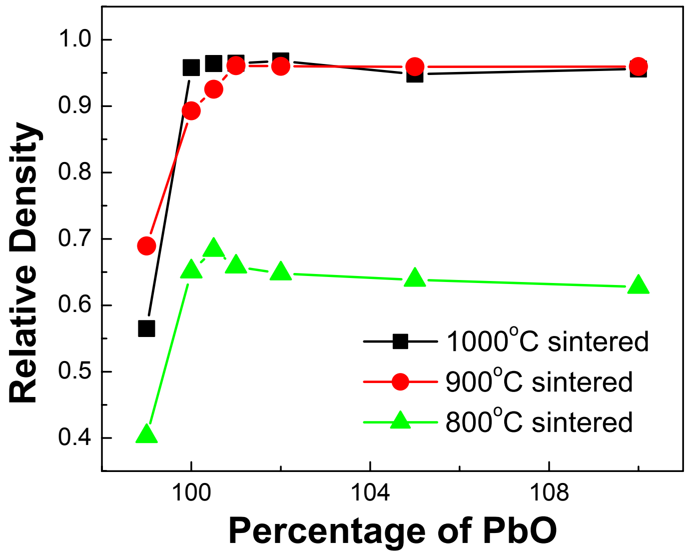

Figure 8.9: Relative densities versus PbO percentage based on the 0.9PMN-0.1PT theoretical density of 8.11g/cm^3.

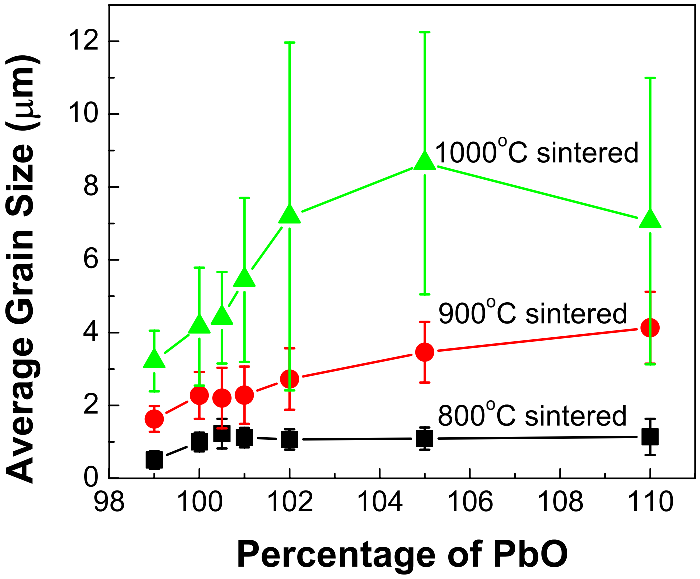

Figure 8.10: Average grain sizes versus PbO percentage.

8.3.2 Sintering and Properties

Figure 8.9 shows the density variations with starting PbO excess after polishing off the surface Massicot PbO layer. The densities before and after polishing off the surface layer are almost the same, so only one group of data is presented here. In this figure, it can be seen that the densities of 0.9PMN-0.1PT-99 are much lower than other samples with more PbO for all the sintering temperatures. This indicates that sufficient amount of PbO is very important for PMN-PT low temperature sintering. Figure 8.9 also showed that once the PbO amount reached the stoichiometric level, additional PbO is not very helpful in increasing the sintering density further. Also revealed in Figure 8.9 is that there is a large density increase between 800°C and 900°C for samples of all the PbO compositions. This suggests the possible formation of PbO liquid phase at a temperature between 800°C and 900°C. The detail will be discussed in the later part of this chapter.

Figure 8.10 shows the change of average grain sizes with starting PbO excess. The grain sizes and error bars here are calculated from the SEM pictures. Figure 8.10 shows that the grain size increases with PbO content for all sintering temperatures. Figure 8.9 and Figure 8.10 represent two aspects of PMN sintering, densification and grain growth respectively. These two figures together show that PbO played an important role in improving both densification and grain growth during PMN sintering.

Figure 8.11 shows the peak dielectric properties as a function of the amount of PbO excess after polishing of the surface Massicot PbO. Similar to the density data, only one group of data is presented here since the properties before and after polishing of the surfaces PbO are similar. Many factors could influence the dielectric constant such as intrinsic dielectric constant of the materials, grain size, density, the amount of PbO in the grain boundary, etc.[43] All these factors are different for the samples that were studied and it is difficult to compare which composition have the highest intrinsic dielectric properties. But from Figure 8.11, the largest overall dielectric constant appears to be between the composition of 0 at% and 1 at% starting PbO excess for all the sintering temperatures. Too much PbO was slightly detrimental to the overall dielectric properties. This maybe because too much PbO will increase the thickness of PbO between grain boundaries, thus lowering the dielectric properties.

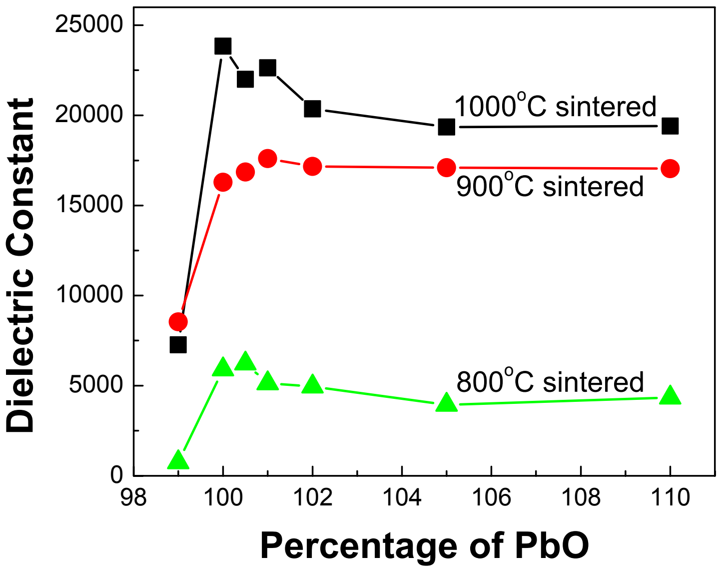

Figure 8.11: Peak dielectric constants vs. PbO percentage.

In summary, the following behavior was observed. For the first time, Massicot PbO oxide is observed on the surface of sintered PMN-PT samples that is not PbO deficient. The lower surface of the sample always has more PbO than the upper surface.

The amount of surface PbO increases with starting PbO amount. Thermal etching analysis showed that the surface PbO seems to be extruded out of the grain or grain boundary. Sufficient PbO is necessary to sinter PMN-PT. A large density increase was observed between 800°C and 900°C sintered samples. Also, Figure 8.9, 8.10, and 8.11 all reveal a saturation behavior in both sintering behavior and dielectric property after the PbO excess amount reaches the level between 0 at% and 2 at%. These phenomena are likely to be related to the formation of PbO liquid phase during sintering. As summarized by Guha,[97] the lowest melting point in the system of PbO and Nb_2O_5 has been established to be 835ºC, which is attributed to a eutectic between PbO and $Pb_3Nb_2O_8$ at a composition of 94 mol% PbO. The existence of this low melting point PbO rich phase was further proven by Nb_2O_5-MgO-PbO ternary phase diagram at 1000ºC.[98] As shown by Figure 8.6, the surface plate in our case is mainly PbO with ~10 mole% of Nb_2O_5. Therefore, for samples with PbO excess in our systems, PbO rich liquid phase will begin forming at 835°C. This PbO rich liquid phase has also been observed between grain boundaries with thickness in the order of 1 nm by several papers in both PMN and other PbO containing perovskite ceramics.[90, 91, 99] In sintering theory, the formation of liquid phase can improve the sintering densification process. This could explain the density jump between the 800°C and 900°C sintered samples and why stoichiometric PbO is necessary for PMN-PT to have high sintered density. Generally, the inter-granular glass/liquid phase thickness will have an equilibrium value in the order of nm for most ceramics due to the balance between the inter-granular van der Waals attraction and the double-layer repulsion.[100, 101] The PbO liquid equilibrium thickness is ~1 nm for PMN.[92] If triple pocket space is not considered, the liquid phase between grain boundaries with 1 nm in thickness will only occupy ≈0.06 vol% of the total volume for samples with average grain size of 5 μm. This volume percentage is very small compared with the starting PbO excess. Therefore, the formed liquid phase will tend to be squeezed out to the surface as the densification and grain growth continues. Since the sintering temperature is not high enough to cause the squeezed liquid phase on the surface to evaporate, liquid PbO will accumulate on the surface to form a PbO rich layer. Because of gravity effects and the difficulty of evaporation, the bottom side of the samples accumulates more PbO than the upper surface. In addition, since the amount of PbO liquid phase formed depends on the starting PbO amount, larger starting PbO amount will always create more PbO accumulation on the surface. Since the amount of liquid phase that grain boundary could accommodate is fixed at a certain value, the extra liquid PbO will be extruded out. It is possible that when the amount of starting PbO excess reaches a certain level, the actual PbO content in the lattice and grain-boundaries will not change further. This could explain the saturation effect observed in Figure 8.9, 8.10, and 8.11. The sintering process described above is illustrated in Figure 8.12. Similar model has been used to explain the surface PbO in the system of $PbNi_{1/3}Nb_{2/3}O_3$-$PbTiO_3$-$PbZrO_3$ recently.[99] However the detailed mechanism of how the liquid was squeezed out is not clear yet.

8.4 Summary

By the low-temperature PMN sintering method using the coated powders, it was found that PbO accumulated on the surface of samples. The surface PbO was in the form of plates with thickness in the order of micrometers. The lower side of a piece always has more surface PbO than the upper side. On average, the surface PbO amount increases with the starting PbO amount.

PbO plays an important role in both the sintering and the properties of PMN-PT. Sufficient PbO is necessary for obtaining the desired density and grain size. The observed behavior is probably related to the formation of a PbO rich liquid phase which was squeezed to the sample surface during densification.

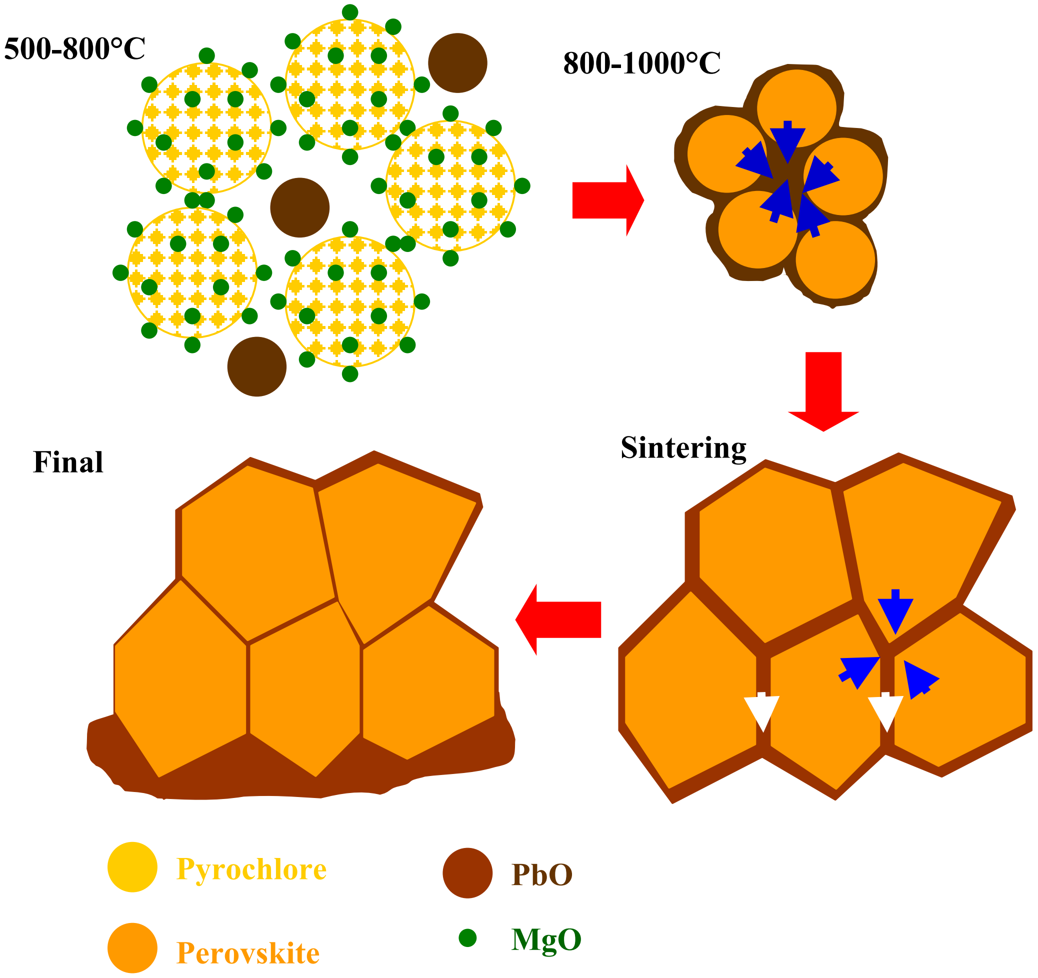

Figure 8.12: Reactively sintering process illustrations of PMN-PT with excess PbO.

CHAPTER 9: CONCLUSIONS AND FUTURE WORK

In this thesis, the phenomenon of colloidal coating was studied by both experiment and numerical simulation. The simulation results provide an understanding how $Mg(OH)_2$ was coated on the surface of Nb_2O_5. By mixing the $Mg(OH)_2$ coated Nb_2O_5 powder with PbO and PT, we showed that it is possible to produce pyrochlore-free PMN-PT powder with only one calcination step. By pressing the coated powder mixture, it is possible to reactively sinter PMN-PT with only a single step of heat-treatment at a sintering temperature as low as 1000°C. Furthermore, the reasons why the coating method could generate almost pure perovskite phase; why the coating method could decrease the sintering temperature; and the effect of excess PbO content were also studied. The following are the conclusions of this thesis.

9.1 General Conclusions

1. A Monte Carlo model based on SAK model was developed to numerically simulate colloidal coating. Compared with the model currently available, this is more realistic. Using this model, the colloidal coating process was demonstrated and the factors that influencing the coating quality were studied. Simulation results showed that: Colloidal coating is accomplished mostly by the dissolution of the precipitates of coating species followed by the re-precipitation on the particle surface. With high particle surface charge, individual particles of coating species formed when the coating species concentration is high. Aging could assist in the formation of more complete and thicker coating. Smaller core particle size,

higher core particle concentration and higher coating species solubility could help prevent the formation of individual particles of coating species particles. Increased coating species solubility and decreased particle size could help obtain thicker coatings. These simulation results are consistent with the experimental results.

2. $Mg(OH)_2$ was coated on the surface of Nb_2O_5 powder by precipitating $Mg(OH)_2$ in an aqueous Nb_2O_5 suspension at pH 10. Pyrochlore-free perovskite PMN and 0.9PMN-0.1PT could be produced after calcining the ball-milled coated powder to 900°C for 2 hours. In this method, only a single calcination step and a single ball-milling step are needed to produce pyrochlore-free PMN or PMN-PT powder.
3. By using the $Mg(OH)_2$-coated Nb_2O_5 powder , 0.9PMN-0.1PT with good relative density, grain size can be reactively sintered at 1000°C. The generated product has slightly better dielectric properties than commercial product. The sintering temperature is 200°C lower than that of the traditional columbite method. Due to the reactive sintering, the processing was simplified to only a single coating step, a single ball-milling step, and a single sintering step. Because this method needs only micron-sized reactant, regular processing equipment and simplified processing steps, it has great potential for cost effective PMN-PT production.
4. Mechanism studies showed that nanosize pyrochlore particle was formed during the calcination of the coated powder due to the reaction-induced volume expansion. The nanosize pyrochlore particle and the coating configuration decrease the diffusion distance in reaction and thus help complete the

transformation from pyrochlore to perovskite phase. Besides the factors above, the concurrence of reaction and sintering and the formation of liquid phase are the reasons for the low temperature PMN-PT reactive sintering.

5. By using the reactive sintering method, it was found for the first time that plate-like PbO in the order of micrometer size accumulated on the sample surface. The lower side of a piece always has more surface PbO than the upper side. On average, the surface PbO amount increases with increasing PbO amount. The PbO plays an important role in both sintering and properties. Sufficient PbO could enhance both densification and grain growth. The PbO behaviors are probably related to the formation of PbO-rich liquid phase which was squeezed to the sample surface during densification.

9.2 Recommendations for the Future Work

Reactive sintering is not a new technology. It has been utilized in many ceramic and powder metallurgy systems. It has also been tried in the PMN-PT processing from the intermediate product of $MgNb_2O_6$. The major contribution of this thesis is that we introduced this technology into the system of PMN-PT processing from the very beginning through a coating approach. Therefore, the processing is simplified further and the sintering temperature is decreased. This method is the only method so far that can overcome the major challenges for PMN-PT processing simultaneously. Some new phenomena and the working mechanisms accompanying this processing technology were also elucidated in this thesis. To fully exploit the potential of this technology, the following is my recommendations for the future work in this area:

1. Applied this technology to similar systems. Many lead containing perovskite ceramics systems, such as $Pb(Ni_{1/3}Nb_{2/3})O_3$ (PNN), $Pb(Fe_{1/2}Nb_{1/2})O_3$ (PFN), $Pb(Mg_{1/3}Ta_{2/3})O_3$ (PMT), $PbSc_{1/2}Ta_{1/2}O_3$ (PST), $Pb(In_{1/2}Nb_{1/2}O_3)$ (PIN), $Pb(Mg_{2/3}W_{1/3})O_3$ (PMW), are very similar to PMN-PT in properties, crystal structure, and processing. It is also required to avoid pyrochlore phase, lower sintering temperature, and simplify processing steps in these systems. Based on the mechanism found in previous chapters, it is very possible that this reactive sintering through coating approach could equally work for these systems. More broadly, due to the ability of improving mixing and composition uniformity, the coating method could possibly be further applied to other ceramics system for low temperature sintering.
2. Optimizations. In this thesis, not much work was devoted to the processing optimizations. Optimizations include finding the best MgO, PbO composition; the best coating condition; the best heat-treatment curve; the best ball-milling condition. Also the processing may be able to be simplified further. The results in this thesis opened the possibility of simplifying the processing and decreasing the sintering temperature for the system of PMN-PT processing by reactive sintering. But this method may not be the simplest methods due to its extra step of colloidal coating and evaporation. Based on the fact that more than 10 one-step calcination PMN powder processing methods have been found so far, it is still possible to find simpler PMN-PT reactive sintering methods. For example, we have revealed that the balling-milling in isopropanol would break Nb_2O_5 agglomerations. At the same time, the initial $Mg(OH)_2$ coating would also be broken with the ball-milling

and then recoating on the ball-milled Nb_2O_5. If we skip the first step of pre-coating and directly ball-mill the mixture of $Mg(OH)_2$, Nb_2O_5, and PbO, $Mg(OH)_2$ still could possibly be coated on the surface of Nb_2O_5 after ball-milling and have the same effect as the pre-coated method we described in this thesis.

3. Micro or nano size device. The PbO plates described in Chapter 8 show very interesting geometrical behaviors as illustrated in Figure 9.1. Many of them appear to be single crystal structure sticking out of the sample surface. They could be a new material choice for low dimension devices for electronics or MEMS applications. Therefore, it is worthy to investigate their properties and behaviors, further. The study in this direction could also help answer the question of how PbO is extruded to the sample surface. Methods like Nano-Indentation, TEM etc. could be utilized for this purpose.

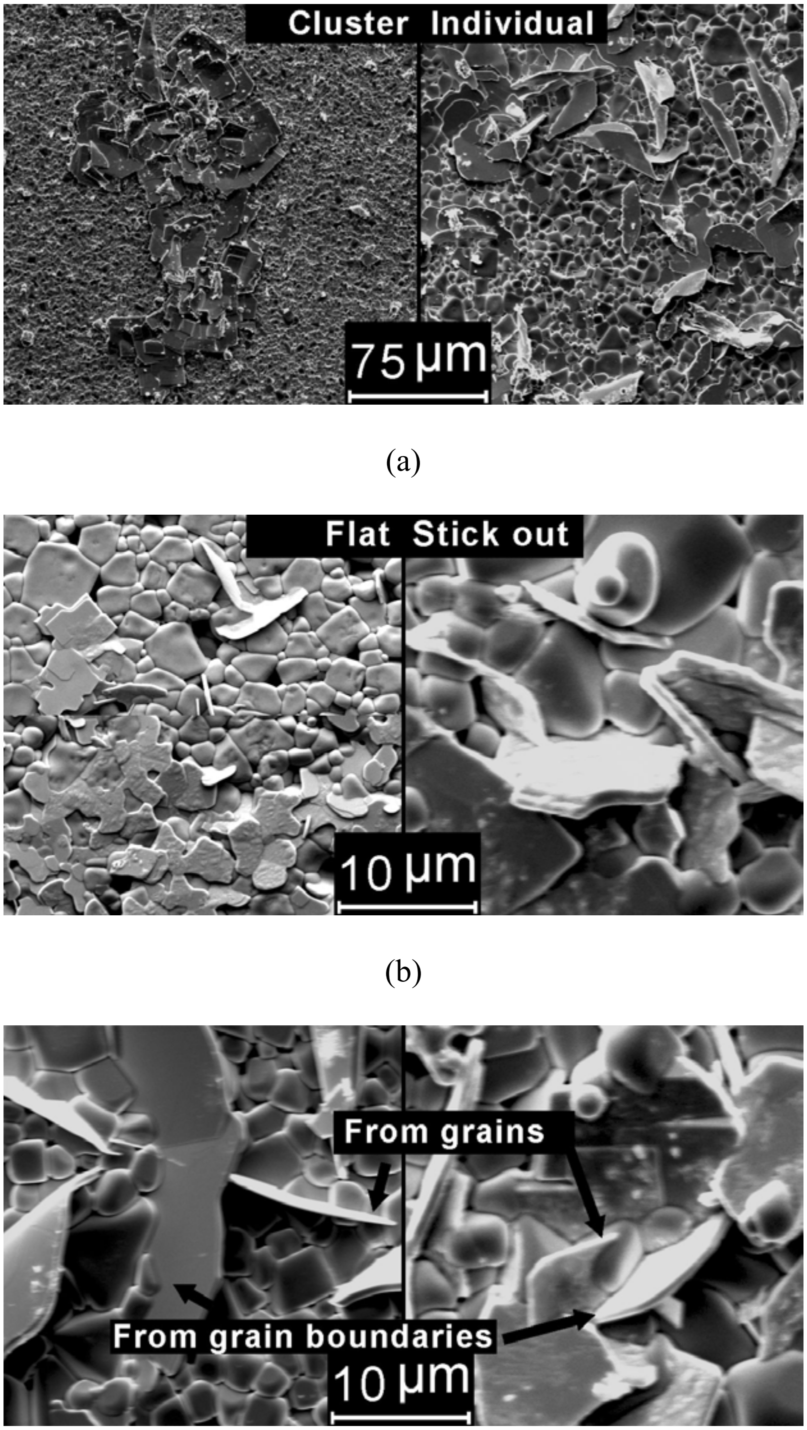

(a)

(b)

(c)

Figure 9.1: Geometrical behavior of surface PbO. (a) PbO plates cluster versus stand-along PbO plates. (b) Flatten PbO plates versus PbO plate stick out. (c) The places that PbO plates grow out. (d) Various PbO plate details

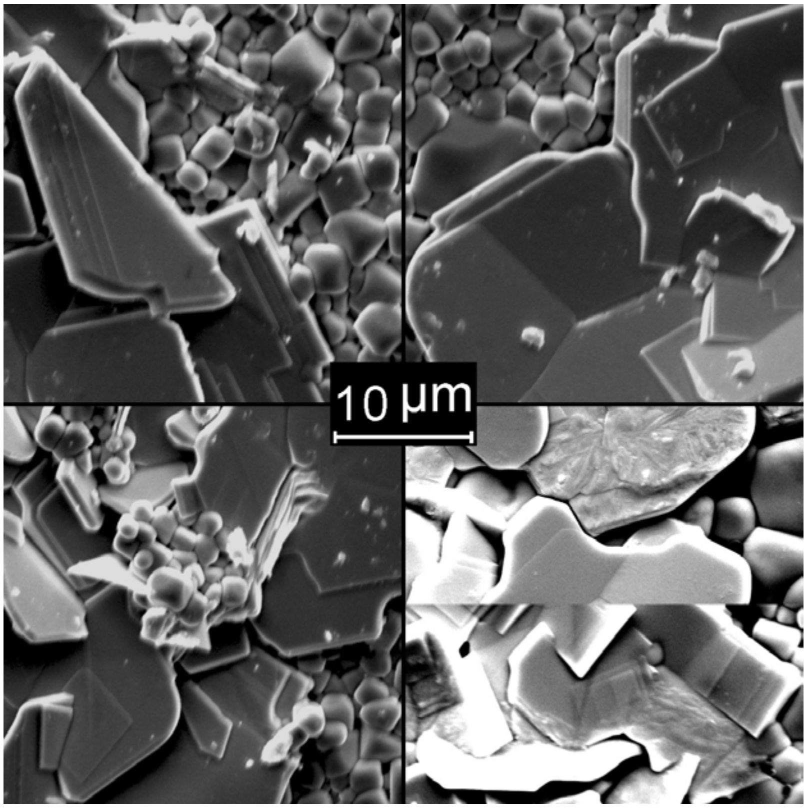

(d)

Figure 9.1 (continued)

LIST OF REFERENCES

1 C. L. Grahl, “Advanced Ceramics Experiences Severe Downturn; Recovery Expected in Late 2002 or 2003”, *Ceramics Industry*, August, p16-18 (2002)

2 J. Herbert, 1985a: Ceramic Dielectrics and Capacitors, *Electrocomponents Science Monographs*, Vol6, Gordon Breach, London (1985)

3 J. Herbert, 1985b: Ferroelectric Transducers and Sensors, *Electrocomponent Science Monographs*, Vol. 3. Gordon and Breach, London (1985)

4 E. R. Myers, and A. I. Kingon, Ferroelectric Thin Films, *Materials Research Symposium Proceedings*, San Fransisco, 200 (1990)

5 L. M. Levinson, *Electronic Ceramics*, Marcel Decker, NY (1988)

6 R. E. Aldrich, *Ferroelectrics*, 27, 19 (1980)

7 S. G. Porter, *Ferroelectrics*, 33, 193 (1981)

8 R. W. Whatmore, J. M. Herbert, and F. W. Ainger, *Phys. Status Solidi*, A61, 73 (1980)

9 L. Hanke, *Seimens Forsch Ber*. 8.4, 209 (1979)

10 R. Alfness, *Proc. ISAF 86*, Lehigh University, 1 (1986)

11 L. E. Cross, “Relaxor Ferroelectrics,” *Ferroelectrics*, 151, 305-20 (1994)

12 H. Jaffe and D. A. Berlincourt, "Piezoelectric Transducer Materials," *Proc. IEEE*, 53 [10] 1372-86 (1965)

13 M. A. Ealey and P. A. Davis, "Standard SELECT Electrostrictive Lead Magnesium Niobate Actuators for Active and Adaptive Optical Components," *Opt. Eng.*, 29 [11] 1373-82 (1990)

14 J. Zhao, Q. M. Zhang, N. Kim, and T. Shrout, "Electromechanical Properties of Relaxor Ferroelectric Lead Magnesium Niobate-Lead Titanate Ceramics," *Jpn. J. Appl. Phys.*, Part I, 34 [10] 5658-63 (1995)

15 G. H. Haertling, "Electro-optic Ceramics and Devices"; pp. 371-492 in *Electronic Ceramics*. Edited by L. M. Levinson. Marcel Dekker, New York, (1988)

16 Z. Y. Meng, U. Kumar, and L. E. Cross, "Electrostriction in Lead Lanthanum Zirconate Titanate (PLZT) Ceramics," in Piezoelectric and Electrostrictive Materials for Transducer Applications, ONR Annual Rep. No. N00014-82-K0339, Pennsylvania State University, University Park, PA, May (1985)

17 H. Banno, "Piezoelectric Transducer and Piezoelectric Ceramics"; pp. 2017-23 in *Encyclopedia of Advanced Materials*. Edited by R. W. Cahn. Pergamon Press, Oxford, U.K., (1995)

18 M. Inada, "Analysis of the Formation Process of the Piezoelectric PCM Ceramics," *Jpn. Natl. Tech. Rept.*, 27[1] 95-102 (1977)

19 O. Bouquin, and M. Lejeune, "Formation of the Perovskite Phase in the $PbMg_{1/3}Nb_{2/3}O_3$-$PbTiO_3$ System," *J. Am. Ceram. Soc.*, 74[5] 1152-56 (1991)

20 T. R. Shrout and S. L. Swartz, "Dielectric Properties of Pyrochlore Lead Magnesium Niobate," *Mater. Res. Bull.*, 18, 663-67 (1983)

21 I. I. Adrianova, *Opt. Spectrosc.*, 36, 547, (1974)

22 N. Wakiya, A. Saiki, N. Ishizawa, K. Shinozaki, and N. Mizutant, "Crystal-Growth, Crystal-Structure and Chemical-Composition of A Pyrochlore Type Compound in Lead-Magnesium-Niobium-Oxygen System," *Mater. Res. Bull.*, 28 (2): 137-143 (1993)

23 E. Goo, *J. Am. Ceram. Soc.*, 69, 188, (1986)

24 J. Chen, *J. Am. Ceram. Soc.*, 69, C303, (1986)

25 F. Chaput, J. P. Boilot, M. Lejeune, R. Papiernik, and L. G. Hubert Pfalzgraf, "Low-Temperature Route to Lead Magnesium Niobate," *J. Am. Ceram. Soc.*, 72 [8] 1355–57 (1989).

26 J. Chen, M. P. Harmer, "Microstructure and Dielectric-Properties of Lead Magnesium Niobate Pyrochlore Diphasic Mixtures," *J. Am. Ceram. Soc.*, 73(1) 68-73 (1990)

27 N. Wakiya, B. H. Kim, K. Shinozaki, N. Mizutani, "Composition Range of Cubic Pyrochlore Type Compound in Lead Magnesium Niobium Oxygen System," *J. Ceram. Soc. of Jpn.*, 102 (6) 612-615 (1994)

28 A. Mergen, I. M. Reaney, W. E. Lee, "Microstructures of Pyrochlore-Perovskite Mixtures in PbO-MgO-Nb_2O_5 System," *Brit. Ceram. Trans.*, 96(2) 41-49 (1997)

29 J. P. Guha, "Reaction chemistry and subsolidus phase equilibria in lead-based relaxor systems: Part I - Formation and stability of the perovskite and pyrochlore compounds in the system PbO-MgO-Nb_2O_5", *J. Mater. Sci.*, 34 4985-4994 (1999)

30 R. C. West and M. J. Astle (eds.), *Handbook of Chemistry and Physics;. CRC* Press, Boca Raton, FL, 1979–1980.

31 G. Desgardin, A. Bali, and B. Raveau, "Ceramiques Composites A Base De Perovskite et Pyrochlores Au Plomb PZN $(PbZn_{1/3}Nb_{2/3})O_3$: PFN $(PbFe_{1/2}Nb_{1/2})O_3$ et PMN $(PbMg_{1/3}Nb_{2/3}O_3)$ pir Condensateurs Multicouches a Haute Constante Dielectrique," *Mater. Chem. Phys.*, 8, 469-91 (1983).

32 S. L. Swartz and T. R. Shrout, "Fabrication of Perovskite Lead Magnesium Niobate," *Mater. Res. Bull.*, 17, 1245–50 (1982).

33 P. Ravindranathan, S. Komareni, A. S. Bhalla, and R. Roy, "Synthesis and Dielectric Properties of Sol–Gel-Derived $0.9Pb(Mg_{1/3}Nb_{2/3})O_3$–$0.1PbTiO_3$ Ceramics," *J. Am. Ceram. Soc.*, 74 [12] 2996–99 (1991).

34 F. Chaput, J. P. Boilot, M. Lejeune, R. Papiernik, and L. G. Hubert Pfalzgraf, "Low-Temperature Route to Lead Magnesium Niobate," *J. Am. Ceram. Soc.*, 72 [8] 1355–57 (1989).

35 Y. Narendar and G. L. Messing, "Kinetic Analysis of Combustion Synthesis of Lead Magnesium Niobate from Metal Carboxylate Gels," *J. Am. Ceram. Soc.*, 80 [4] 915–24 (1997).

36 J. P. Lee, J. Lee, S. Kang, and H. Kim, "Synthesis of $Pb(Mg_{1/3}Nb_{2/3})O_3$ Powder by Solvent Evaporation and Its Dielectric Properties," *J. Korean Ceram. Soc.*, 33 [1] 17–24 (1996).

37 M. Lejeune and J. P. Boilot, "Formation Mechanism and Ceramic Process of the Ferroelectric Perovskites: $Pb(Mg_{1/3}Nb_{2/3})O_3$ and $PbFe_{1/2}Nb_{1/2}O_3$," *Ceram. Int.*, 8 [3] 99–104 (1982).

38 Y. Ogata, and Y. Shinohara, " Method for production of dielectric powder," *US Patent* No: 4,636,248, (1987)

39 W. B. Ng, J. Wang, S. C. Ng, and L. M. Gan, "Processing and Characterization of Microemulsion-Derived Lead Magnesium Niobate," *J. Am. Ceram. Soc.*, 82 [3] 529–36 (1999)

40 J. G. Baek, T. Isobe, and M. Senna, “Synthesis of Pyrochlore-Free 0.9Pb-($Mg_{1/3}Nb_{2/3}$)O_3–0.1$PbTiO_3$ Ceramics via a Soft Mechanochemical Route,” *J. Am. Ceram. Soc.*, 80 [4] 973–81 (1997).

41 K. R. Han, S. Kim, and H. J. Koo, “New Preparation Method of Low-Temperature-Sinterable Perovskite-Free 0.9Pb($Mg_{1/3}Nb_{2/3}$)O_3–0.1$PbTiO_3$ Powder and Its Dielectric Properties,” *J. Am. Ceram. Soc.*, 81 [11] 2998–3000 (1998).

42 A. L.Costa, C. Galassi, and E. Roncari, "Direct synthesis of PMN samples by spray-drying," *J. Euro. Ceram. Soc.*, 22, 2093–2100 (2002)

43 T. R. Shrout and A. Halliyal, “Preparation of Lead-Based Ferroelectric Relaxors for Capacitors,” *Am. Ceram. Soc. Bull.*, 66 [4] 704–11 (1987).

44 C. H. Lu, and C. Y. Wen, "Thermal Decomposition and kinetic analysis of relaxor ferroelectric lead magnesium niobate", *J. Euro. Ceram. Soc.*, 18, 1599-1607 (1998)

45 D. Saha, A. Sen, H. S. Maiti, *Ceramics International*, 25 (2): 145-151 (1999)

46 Y. Yang, C. D. Feng, and Y. H. Yu, *Materials Lett.*, 49 (6): 345-351 (2001)

47 Y. C. Liou, L. Wu, and S. S. Liou, Jpn. *J. Appl. Phys.*, Vol. 33 Pt. 2, No. 9B (1994)

48 S. Kwon, E. M. Sabolsky, G. L. Messing, *J. Am. Ceram. Soc.*, 84[3]648-50 (2001)

49 C. L. Hu, and M. N. Rahaman, *J. Am. Ceram. Soc.*, 75[8], 2066 (1992)

50 V. Bokov and I. Mylnikova, *Soviet Physics Solid State*, 3, 3 (1960)

51 J. Zhao, Q. M. Zhang, N. Kim, and T. Shrout, “Electromechanical Properties of Relaxor Ferroelectric Lead Magnesium Niobate—Lead Titanate Ceramics,” *Jpn. J. Appl. Phys.*, Part I, 34 [10] 5658–63 (1995).

52 W.-H. Shih, and L.-L. Pwu, *J. Am. Ceram. Soc.*, 78[5], 1252 (1995)A

53 W.-H. Shih, and L.-L. Pwu, *J. Mat. Res.*, 10[11], 2808 (1995)(B)

54 C. L. Hu, and M. N. Rahaman, *J. Am. Ceram. Soc.*, 75[8], 2066 (1992)

55 C. Y. Yang, W. Y. Shih, and W.-H. Shih, *J. Am. Ceram. Soc.*, 82[2], 436 (1999)

56 M. Ohmori, and E. Matijević, *J. Colloid Interface Sci.*, 150[2], 594 (1992)

57 I. Haq, and E. Matijević, *Colloids Surfaces A – Physicochemical and Engineering Aspects*, 81, 153 (1993)

58 C. Y. Yang, Ph.D Thesis, Department of Materials Engineering, Drexel University, Philadelphia, PA. (2000)

59 W. Y. Shih, I. A. Aksay, and R. Kikuchi, *Phys. Rev.* A 36, 5015 (1987)

60 W. Y. Shih, J. Liu, W.-H. Shih, and I. A. Aksay, *J. Stat. Phys.*, 62, 961 (1991)

61 J. Liu, M. Sarikaya, W. Y. Shih, and I. A. Aksay, *Phys. Rev.* A 41, 3206 (1990)

62 W. Y. Shih, W.-H. Shih, and I. A. Aksay, in Physical Phenomena in Graduate Materials, edited by G. D. Cady, T. H. Geballe, and P. Sheng, *Mater. Res. Soc. Symp. Proc.* No. 195 (Materials Research Society, Pittsburgh, 1990), p. 477.

63 T. Terao, and T. Nakayama, *J. Phys., Condens. Matter.*, 11, 7071 (1999)

64 J. Liu, W. Y. Shih, R. Kikuchi, and I. A. Aksay, *J. Colloid Interface Sci.*, 142, 369 (1991)

65 M. Yasrebi, W. Y. Shih, and I. A. Aksay, *J. Colloid Interface Sci.*, 142, 357 (1991)

66 W. Y. Shih, W.-H. Shih, and I. A. Aksay, *J. Am. Chem. Soc.*, 79, 2587 (1996)

67 C. Y. Yang, W. Y. Shih, and W.-H. Shih, *Phys. Rev.* E 64, 0211403 (2001)

68 G. H. Bogush, and C. F. Zukoski, *J. Colloid Interfacer Sci.*, 142, 19 (1991)

69 H. Y. Luo, W. Y. Shih, and W.-H. Shih, "Effects of Particle Size and Aging on the Coating of $Mg(OH)_2$ on Nb_2O_5 Particles", *International Journal of Applied Ceramic Technology*, (to be published)

70 P. Ravindranathan, S. Komareni, A. S. Bhalla, and R. Roy, “Synthesis and Dielectric Properties of Sol–Gel-Derived $0.9Pb(Mg_{1/3}Nb_{2/3})O_3$–$0.1PbTiO_3$ Ceramics,” *J. Am. Ceram. Soc.*, 74 [12] 2996–99 (1991).

71 Y. Narendar and G. L. Messing, “Kinetic Analysis of Combustion Synthesis of Lead Magnesium Niobate from Metal Carboxylate Gels,” *J. Am. Ceram. Soc.*, 80 [4] 915–24 (1997).

72 R. C. West and M. J. Astle (eds.), *Handbook of Chemistry and Physics*; p. B-220. CRC Press, Boca Raton, FL, 1979–1980.

73 T. R. Shrout, P. Papet, S. Kim, and G. S. Lee, “Conventionally prepared submicrometer lead-based perovskite powders by reactive calcination,” *J. Am. Ceram. Soc.*, 73[7] 1864-67 (1990)

74 S. Venkataramani, “Calcining and its effects on sintering and properties of lead zirconate titanate ceramics”; Ph.D. Thesis. The Pennsylvania State University, University Park, PA, 1981

75 D. A Buckner and P. D. Wilcox, “Effects of calcining on sintering of lead zirconate titanate ceramics,” *Am. Ceram. Soc. Bull.*, 51, 218-22 (1972)

76 P. Papet, J. P. Dougherty, and T. R. Shrout, “Particle and grain size effects on the dielectric behavior of the relaxor ferroelectric $Pb(Mg_{1/3}Nb_{2/3})O_3$”, *J. Mater. Res.*, 5[12], 2902-09, (1990)

77 C. A. Randall, N. Kim, J. Kucera, W. Cao, and T. R. Shrout, "Intrinsic and Extrinsic Size Effects in Fine-Grained Morphotropic-Phase-Boundary Lead Zirconate Titanate Ceramics," *J. Am. Ceram. Soc.*, 81[3], 677–88, (1998)

78 H. Seyeda and J. Margalit, “Improving Electronic Ceramics with Niobium and Tantalum,” *Ceramic Industry*, June, (2002)

79 http://www.matweb.com/search/SpecificMaterial.asp?bassnum=CEDO13

80 C. Herring, *J Appl. Phys.*, 21, 301±303 (1950)

81 D. J. Lewis, D. Gupta, M. R. Notis, Y. Imanaka, "Diffusion of Ag-110m tracer in polycrystalline and single-crystal lead-containing piezoelectric ceramics,” *J. Am. Ceram. Soc.*, 84, (8), 1777-1784 (2001)

82 G. L. Messing, and M. Kumagai, “ Low-temperature sintering of α-alumina-seeded boehmite gels,” *Am. Ceram. Soc. Bull.*, 73, (10), 88-91, (1994)

83 W. Zeng, L. Gao, L. Gui, J. Guo, "Sintering kinetics of -Al_2O_3 powder," *Ceramics International*, 25 723 (1999)

84 J. Li, and X. Sun, “Synthesis and sintering behavior of a nanocrystalline α-alumina powder,” *Acta mater.*, 48, 3103-3112, (2000)

85 M. Kumagai, and G. L. Messing, “Controlled transformation and sintering of a boehmite Sol-Gel by α-alumina seeding,” *J. Am. Ceram. Soc.*, 68, [9], 500-505, (1985)

86 L. B. Kong, and J. Ma, "PZT ceramics formed directly from oxides via reactive sintering," *Materials Letters*, 51[10], 95-100 (2001)

87 R. M. German, “Sintering theory and practice,” A Wiley-Interscience Publication, New York, p7, (1995)

88 C. J. Brinker and G. W. Scherer, “Sol-Gel Science,” Academic Press, New York, Chap. 11, (1990)

89 H. M. Jang, K-M. Lee, and M-H. Lee, “Stabilization of Perovskite Phase and Dielectric Properties of $Pb(Zn,Mg)_{1/3}Nb_{2/3}O_3$-$PbTiO_3$ Ceramics Prepared by Excess Constituent Oxides,” *J. Mater. Res.*, 9 [10] 2634-44 (1994).

90 H. C. Wang, and W. A. Schulze, “The Role of Excess Magnesium Oxide or Lead Oxide in Determining the Microstructure and Properties of Lead Magnesium Niobate,” *J. Am. Ceram. Soc.*, 73 [4] 825-32 (1995).

91 A. L. Costa, C. Galassi, G. Fabbri, E. Roncari, and C. Capiani, “Pyrochlore Phase and Microstructure Development in Lead Magnesium Niobate Materials,” *J. Euro. Ceram. Soc.*, 21 1165-70 (2001).

92 H. M. Jang, K-M. Lee, “Dielectric and Piezoelectric Properties of the Thermally Annealed $Pb(Zn, Mg)_{1/3}Nb_{2/3}O_3$-$PbTiO_3$ System Across the Rhombohedral/tetragonal Morphotropic Phase Boundary,” *J. Mater. Res.*, 10 [12] 3185-93 (1995).

93 S. M. Gupta, and A. R. Kulkarni, “Role of Excess PbO on the Microstructure and Dielectric Properties of Lead Magnesium Niobate,” *J. Mater. Res.*, 10 [4] 953-61 (1995).

94 J. P. Guha, D. J. Hong, and H. U. Anderson, “Effect of Excess PbO on the Sintering Characteristics and Dielectric Properties of $Pb(Mg_{1/3}Nb_{2/3})O_3$-$PbTiO_3$ Based Ceramics,” *J. Am. Ceram. Soc.*, 71 [3] C-152-54 (1988).

95 M. Villegas, A. C. Caballero, C. Moure, P. Duran, and J. F. Fernandez, “Effects of PbO Excess in $Pb(Mg_{1/3}Nb_{2/3})O_3$-$PbTiO_3$ Ceramics: Part I. Sintering and Dielectric Properties,” *J. Mater. Res.*, 14 [3] 891-97 (1999).

96 C. H. Lu, and C.Y. Wen, "Thermal Decomposition and Kinetic Analysis of Relaxor Ferroelectric Lead Magnesium Niobate," *J. Euro. Ceram. Soc.*, 18 1599-1607 (1998).

97 J. P. Guha, "Reaction chemistry and subsolidus phase equilibria in lead-based relaxor systems Part II The ternary system PbO-MgO-Nb_2O_5," *J. of Mater. Sci.* 36 5219 - 5226 (2001)

98 P. Lucas and W. T. Petuskey, "Phase Equilibria in the Lead–Magnesium–Niobium–Oxygen System at 1000°C," *J. Am. Ceram. Soc.,* 84 [9] 2150–52 (2001)

99 M. Kondo and K. Kurihara, "Sintering Behavior and Surface Microstructure of PbO-Rich $PbNi_{1/3}Nb_{2/3}O_3$-$PbTiO_3$-$PbZrO_3$ Ceramics," *J. Am. Ceram. Soc.*, 84 [11] 2469-74 (2001).

100 D. R. Clarke, "On the equilibrium thickness of intergranular glass phases in ceramics materials," *J. Am. Ceram. Soc.*, 70 [1] , 15-22 (1987)

101 R. H. French, "Origins and Applications of London Dispersion Forces and Hamaker Constants in Ceramics," *J. Am. Ceram. Soc.*, 83 [9] 2117–46 (2000)

VITA

Name: Huiming Gu
Date of Birth: July 12, 1974
Citizenship: People Republic of China

Education:

Ph.D. in Materials Science & Engineering, Drexel University, Philadelphia, PA, 2003
M.S. in Microelectronics & Solid State Electronics, Shanghai Institute of Technical Physics, Chinese Academy of Science, Shanghai, China, 1999
B.S. in Materials Science & Engineering, Tsinghua University, Beijing, China, 1996

List of Publications:

- H. M. Gu, W. Y. Shih, W.-H. Shih, "Study of Mechanism of Pyrochlore Free PMN-PT Powder Using Coating Method", *American Ceramics Society 105th Proceeding*, Nashville, TN, April, (2003)
- H. M. Gu, W. Y. Shih, W.-H. Shih, "A Single-Calcination Synthesis of Pyrochlore-Free 0.9PMN-0.1PT and PMN Ceramics by a Coating Method", *Journal of American Ceramics Society*, 86 (2), 217-221, (2003)
- J. R. Yang, H. M. Gu, X. Q. Chen, W. Z. Fang, L. He, "Dislocation assessment of CdZnTe by chemical etching on both {111}B and {211}B faces", *Journal of Crystal Growth*, 234 (2-3): 337-342, (2002)
- W. Y Shih, X. P. Li, H. M. Gu, W.-H. Shih, I. A. Aksay, "Simultaneous liquid viscosity and density determination with piezoelectric unimorph cantilevers", *Journal of Applied Physics*, 89 (2) 1497-1505, (2001)
- H. M. Gu, J. R. Yang, X. Q. Chen, L. He, "Difference of EPDs on (111)B and (211)B Faces of CdZnTe Crystals by Using Everson Etch", *Journal of Synthetic Crystals*, Vol.28 No.2 (1999)
- H. M. Gu, J. R. Yang, X. Q. Chen, L. He, "Distribution Behavior of Dislocation in CdZnTe Materials", *Chinese Journal of Semiconductors*, 20 (12) 1059, (1999)

3 more papers and 1 patent are in preparation

Professional Affiliations:

The American Ceramic Society (ACerS)
American Physical Society (APS)